

THE FUNDAMENTAL RELATIONSHIP BETWEEN TOOL WEAR, SURFACE  
INTEGRITY, AND FATIGUE IN MILLING OF DIFFICULT-TO-CUT ALLOYS

by

WEI LI

YUEBIN GUO, COMMITTEE CHAIR

MARK E. BARKEY  
J. BRIAN JORDON  
MARK L. WEAVER  
KEITH A. WOODBURY

A DISSERTATION

Submitted in partial fulfillment of the requirements  
for the degree of Doctor of Philosophy  
in the Department of Mechanical Engineering  
in the Graduate School of  
The University of Alabama

TUSCALOOSA, ALABAMA

2013

Copyright Wei Li 2013  
ALL RIGHTS RESERVED

## ABSTRACT

Tool wear is the critical factor to determine machining economy since it is directly related to tool life and the overall cost of production. Surface integrity (surface finish, microstructure, residual stress, microhardness, and surface chemistry) and service performance (e.g. fatigue life) of machined components can be also adversely affected by tool wear because they deteriorate to an unacceptable level with the progression of tool wear. Therefore, it is necessary to understand and establish the basic relationship between tool wear, surface integrity, and fatigue performance in order to give a general guidance for producing as many quality parts as possible while minimizing machining costs.

This study starts with a critical assessment of literature on surface integrity in machining of difficult-to-cut alloys. To significantly improve the accuracy and repeatability of tool wear measurement, a novel online optical tool inspection system has then been developed to integrate with a CNC machining center to monitor tool wear in milling. The progression of tool flank wear of PVD coated inserts in end milling of AISI H13 tool steel and Inconel 718 superalloy were presented to demonstrate the function of the optical tool inspection system.

A Taguchi design-of-experiment based dry finish milling of AISI H13 tool steel ( $50 \pm 1$  HRC) with (Ti, Al)N/TiN coated cutting tools was conducted to investigate the process-induced surface integrity. The mechanism of surface integrity in hard milling was investigated to understand the effects of mechanical/thermal loads on surface microstructure and properties. The microstructure, microhardness and residual stresses were characterized. A phase transformed

white layer was not observed in the context of concerned process parameters. The milled surfaces are characterized by the increased microhardness and high compressive residual stresses, which are beneficial for improving fatigue performance and wear resistance of the machined components. Finally, the process design space for the desired surface integrity has been established via the microhardness and residual stress maps.

By using the online optical tool inspection system, tool wear effect on surface integrity and fatigue life of AISI H13 tool steel by dry hard milling using PVD coated tools are studied. The evolutions of surface integrity were characterized at different levels of tool flank wear. At each level of tool flank wear, the effects of cutting speed, feed, and radial depth-of-cut on surface integrity were investigated respectively. It shows that surface roughness in the step-over direction is much higher than that in the feed direction under all the milling conditions. The increased tool wear did not necessarily produce a rougher surface in both directions. Optical images of the subsurface microstructure of the machined samples do not show a noticeable white layer or heat affected zones which may be explained by the characteristic of periodic tool/work contact in milling compared to turning and grinding. Residual stresses are compressive in both directions and are more compressive in the step-over direction than the feed direction. Four-point bending fatigue tests were performed using the samples machined at different flank wear conditions. The results show that generally a worn tool reduces fatigue life, and the larger the tool wear, the shorter the fatigue life. The fractured surfaces of fatigued samples were characterized. Fatigue endurance limits of the machined surfaces at different reliability levels were estimated and correlated with the experimentally determined fatigue life.

Tool wear effect on surface integrity and fatigue life of Inconel 718 superalloy by milling using PVD coated tools are also studied. The evolutions of surface integrity including surface

roughness, microstructure, and microhardness were characterized at three levels of tool flank wear ( $VB = 0, 0.1 \text{ mm}, 0.2 \text{ mm}$ ). At each level of tool flank wear, the effects of cutting speed, feed, and radial depth-of-cut on surface integrity were investigated respectively. End milling can produce surface finish between  $0.1 \text{ }\mu\text{m}$  and  $0.3 \text{ }\mu\text{m}$  under most of the conditions. Roughness is generally higher in step-over direction than feed direction. No obvious white layer is observed in subsurface microstructure. The machined surface is significantly work-hardened due to the dominant mechanical loading. Four-point bending fatigue test shows that none of the milled samples failed within four million cycles. Fatigue endurance limits of the machined samples at different reliability levels were calculated and correlated with the experimentally determined fatigue life.

## DEDICATION

This work is dedicated to people who guided me and helped me through the process of conducting this research and writing the manuscript of my PhD dissertation - in particular, my parents, my wife and her parents who stood by me throughout the time taken to complete this work.

## ACKNOWLEDGMENTS

I am pleased to take this opportunity to thank my research advisor, fellow graduate students, Ph.D. committee members, friends, and faculty members who have helped me with this research project. I am most indebted to Dr. Yuebin Guo, the chairman of this dissertation, for giving me the opportunity to conduct this research, providing technical guidance and financial aid, and sharing his research expertise and wisdom with me. I would like to thank all committee members, Drs. Mark Barkey, Brian Jordon, Mark Weaver, and Keith Woodbury for their invaluable input, inspiring questions, and support to the dissertation and my academic progress as well. I also would like to thank Mr. Kenneth Dunn, machine shop chief, and James Yarbrough, Jim Edmonds, and Sam Tingle in the machine shop for their assistance in making fatigue testing fixture and sharing experience. Thanks also go to Dr. Guo's undergraduate research assistants Nathan Ivey, David Mitchell, and Samuel Gray who assisted me in performing machining tests, surface integrity characterization, and fatigue testing. This research would be difficult without the support of my fellow graduate students Subhash Anurag, Rahul Waikar, Michael Sealy, Roberto Caslaru, Hardik Singh, Meisam Salahshoor, Chenhao Fu, and Alejandro Sequera. Finally, I would like to thank my wife who always encourages me to persist in the graduate study.

## CONTENTS

ABSTRACT .....	ii
DEDICATION .....	v
ACKNOWLEDGMENTS .....	vi
LIST OF TABLES .....	xiii
LIST OF FIGURES .....	xv
1. INTRODUCTION .....	1
2. SURFACE INTEGRITY CHARACTERIZATION AND PREDICTION IN MACHINING OF HARDENED AND DIFFICULT-TO-MACHINE ALLOYS: A STATE-OF-ART RESEARCH REVIEW AND ANALYSIS .....	4
2.1. Definition, sources, and effects of residual stresses .....	5
2.2. Experimental characterization of residual stresses in machining of hardened and difficult-to-machine alloys.....	7
2.2.1. RS measurement methods and issues .....	7
2.2.2. The effect of work material on residual stress .....	9
2.2.3. Hardened steel alloys.....	10
2.2.3.1. Hard turning.....	10
2.2.3.2. Hard milling.....	17
2.2.4. Titanium alloys.....	21

2.2.4.1. Turning .....	21
2.2.4.2. Milling .....	24
2.2.5. Nickel-based alloys .....	24
2.2.5.1. Turning .....	24
2.2.5.2. Milling .....	29
2.3. An assessment of current residual stress prediction by finite element simulation .....	30
2.3.1. Material property determination.....	30
2.3.2. Material property modeling .....	32
2.3.3. Tool-chip and tool-work interface modeling .....	35
2.3.4. Simulation methods .....	37
2.3.5. Size effect.....	39
2.4. Future work on multiscale simulation for predicting residual stresses in machining.....	41
2.4.1. Rationale of multiscale simulation .....	41
2.4.2. Challenges and barriers of multiscale simulation for predicting residual stress.....	43
2.5. References .....	44
3. A NOVEL ONLINE OPTICAL SYSTEM FOR INSPECTING TOOL WEAR CONDITION IN MILLING HARDENED STEELS AND NICKEL-BASED SUPERALLOYS .....	53
3.1. Introduction .....	54
3.1.1. Tool wear and its impact on surface integrity, performance. ....	54
3.1.1.1. Tool steel .....	55
3.1.1.2. Nickel-based superalloy .....	57

3.1.2.	Tool condition monitoring methods .....	58
3.1.3.	Research objectives .....	60
3.2.	Experimental procedure .....	61
3.2.1.	On-line optical tool monitoring system .....	61
3.2.2.	Work material and cutting tool .....	62
3.2.2.1.	AISI H13 and PVD insert.....	62
3.2.2.2.	Inconel 718 and PVD insert .....	63
3.2.3.	Milling conditions .....	64
3.3.	Results and discussions .....	64
3.3.1.	Tool wears in end milling .....	64
3.3.1.1.	AISI H13 .....	67
3.3.1.2.	Inconel 718 .....	71
3.3.2.	Tool wear mechanism.....	74
3.4.	Conclusions .....	76
3.5.	References .....	77
4.	<b>AN INVESTIGATION ON PROCESS DESIGN SPACE FOR OPTIMAL SURFACE INTEGRITY IN FINISH HARD MILLING OF TOOL STEEL .....</b>	<b>80</b>
4.1.	Introduction .....	81
4.2.	Experimental procedure .....	84
4.2.1.	Work material, machine tool and cutting tool.....	84
4.2.2.	Experimental design .....	86
4.2.3.	Sample preparation and measurement.....	88
4.2.3.1.	Surface characterization .....	88

4.2.3.2. Subsurface characterization.....	89
4.3. Results and discussions .....	90
4.3.1. Surface formation mechanism.....	90
4.3.2. Surface integrity characterization.....	93
4.3.2.1. Microstructure.....	93
4.3.2.2. Microhardness.....	96
4.3.2.3. Residual stresses .....	103
4.3.3. Process parameter space for desired surface integrity.....	106
4.4. Conclusions .....	106
4.5. Nomenclature.....	108
4.6. References .....	108
5. A FUNDAMENTAL STUDY OF TOOL WEAR EFFECT ON SURFACE INTEGRITY AND FATIGUE LIFE OF TOOL STEEL BY DRY HARD MILLING.....	111
5.1. Introduction .....	112
5.2. Literature review .....	114
5.3. Tool wear vs. surface integrity experiment .....	116
5.3.1. Work material and cutting tool .....	116
5.3.2. Experimental design .....	117
5.3.3. Sample preparation.....	119
5.3.4. Surface integrity characterization.....	119
5.3.4.1. Surface roughness .....	119
5.3.4.2. Subsurface microstructure.....	121
5.3.4.3. Residual stresses .....	124

5.3.4.4. Surface and subsurface microhardness .....	128
5.4. Four-point bending fatigue test.....	133
5.4.1. Fatigue sample preparation .....	133
5.4.2. Fatigue testing setup .....	134
5.4.3. Fatigue performance .....	136
5.4.3.1. Four-point bending fatigue testing.....	136
5.4.3.2. Endurance limit estimation.....	137
5.4.3.3. Fatigued sample characterization.....	139
5.5. Conclusions .....	141
5.6. References .....	142
6. A FUNDAMENTAL STUDY OF TOOL WEAR EFFECT ON SURFACE INTEGRITY AND FATIGUE LIFE OF NICKEL-BASED SUPERALLOY BY END MILLING.....	145
6.1. Introduction .....	146
6.2. Literature review .....	147
6.3. Tool wear vs. surface integrity experiment .....	152
6.3.1. Work material and cutting tool .....	153
6.3.2. Experimental design .....	154
6.3.3. Sample preparation.....	157
6.3.4. Surface integrity characterization.....	157
6.3.4.1. Surface roughness .....	157
6.3.4.2. Subsurface microstructure.....	159
6.3.4.3. Surface and subsurface microhardness .....	160
6.4. Four-point bending fatigue test.....	163

6.4.1. Test specimen preparation .....	163
6.4.2. Fatigue test system setup .....	167
6.4.3. Fatigue performance .....	170
6.4.3.1. Four-point bending fatigue testing.....	170
6.4.3.2. Endurance limit estimation.....	170
6.5. Conclusions .....	173
6.6. References .....	174
7. ANALYSIS OF VARIANCE BASED PREDICTIVE MODEL FOR SURFACE ROUGHNESS IN END MILLING OF IN 718 .....	177
7.1. Introduction .....	178
7.2. Tool wear in machining Inconel alloys .....	179
7.3. Experimental procedure .....	181
7.3.1. Work material and cutting tool .....	181
7.3.2. Tool wear vs. surface integrity experiment.....	182
7.4. Results and discussions .....	183
7.4.1. Characterization of surface roughness.....	184
7.4.2. Predictive model of surface roughness .....	187
7.5. Conclusions .....	195
7.6. References .....	195

## LIST OF TABLES

2.1	General comparison of residual stress measuring methods .....	9
2.2	Experimental matrix .....	19
3.1	Chemical composition of Inconel 718 (wt %).....	63
3.2	Milling parameters for AISI H13 .....	64
3.3	Milling parameters for Inconel 718 .....	64
4.1	Normal chemical composition of AISI H13 steel (wt %).....	84
4.2	Material properties of AISI H13 steel.....	84
4.3	Geometry of milling cutter.....	85
4.4	Factor levels of process parameters in milling experiments .....	87
4.5	Design-of-experiment milling experiments based on the Taguchi method - $L_{16}(4^4)$ .....	88
4.6	X-ray measurement of residual stress .....	89
5.1	End milling plan for tool wear vs. surface integrity experiment .....	118
5.2	End milling parameters to prepare fatigue samples.....	133
5.3	Four-point bending fatigue testing condition .....	135
5.4	Modifying factors of endurance limit .....	138
6.1	Chemical composition of Inconel 718 (wt.%).....	154
6.2	End milling experiment plan to characterize surface integrity.....	155
6.3	End milling parameters to prepare fatigue samples.....	164

6.4 Four-point bending fatigue testing condition .....	169
6.5 Endurance limit modifying factors .....	171
7.1 Chemical compositions of IN 718 (wt. %).....	181
7.2 End milling conditions .....	182
7.3 Experimental matrix in end milling of IN 718 .....	190
7.4 Regression analysis from original data input .....	191
7.5 Reduced experimental matrix in milling of IN 718.....	192
7.6 Regression analysis from the reduced data input .....	192
7.7 Analysis of variance.....	193

## LIST OF FIGURES

2.1	The effect of surface integrity produced in hard turning on rolling contact fatigue life.....	6
2.2	Effects of residual stress.....	7
2.3a	Effect of hardness on residual stress distribution in the subsurface in turning hardened AISI 4340 steel (300 fpm, 0.006 in. depth of cut, 0.035/rev feed) - cutting direction.....	11
2.3b	Effect of hardness on residual stress distribution in the subsurface in turning hardened AISI 4340 steel (300 fpm, 0.006 in. depth of cut, 0.035/rev feed) - feed direction.....	11
2.4	Tool edge honing effect on residual stress in hard turning AISI 52100 .....	12
2.5a	The effect of cutting edge chamfer on residual stress - double chamfer geometry .....	12
2.5b	The effect of cutting edge chamfer on residual stress - effect of double chamfer on residual stress .....	12
2.6a	RS distribution in hard turning AISI 52100 with different rake angle - rake -6 deg.....	13
2.6b	RS distribution in hard turning AISI 52100 with different rake angle - rake -21 deg.....	13

2.6c	RS distribution in hard turning AISI 52100 with different rake angle - rake -41 deg.....	13
2.6d	RS distribution in hard turning AISI 52100 with different rake angle - rake -61 deg.....	13
2.7a	The effect of feed on residual stress profiles in hard turning - Matsumoto et al. ....	14
2.7b	The effect of feed on residual stress profiles in hard turning - Dahlman et al. ....	14
2.8a	The effect of depth of cut on residual stress profiles in hard turning - Matsumoto et al. ....	14
2.8b	The effect of depth of cut on residual stress profiles in hard turning - Dahlman et al.....	14
2.9a	The effect of tool-wear on residual stress profile - RS evolution during tool life .....	15
2.9b	The effect of tool-wear on residual stress profile - RS as a function of tool-wear .....	15
2.10	Tool-wear effect on residual stress .....	15
2.11a	Microstructures of the cross-sectional surfaces - hard turned fresh (HTF).....	16
2.11b	Microstructures of the cross-sectional surfaces - ground fresh (GF) .....	16
2.11c	Microstructures of the cross-sectional surfaces – hard turned with white layer (HTWL).....	16
2.11d	Microstructures of the cross-sectional surfaces – ground with white layer (GWL).....	16
2.12a	Comparison of residual stress profiles for different surface microstructures - feed direction .....	16
2.12b	Comparison of residual stress profiles for different surface microstructures - cutting direction .....	16
2.13a	RS vs. depth below surface when workpiece angle: $\alpha = 0^\circ$ .....	19

2.13b	RS vs. depth below surface when workpiece angle: $\alpha = 60^\circ$ .....	19
2.14a	Effect of tool-wear on residual stress profile in milling of H13 steel with coated carbide. $V = 80$ m/min, $f = 0.15$ mm/rev and $a_p = 0.8$ mm - New tool, $T = 0.6$ min.....	20
2.14b	Effect of tool-wear on residual stress profile in milling of H13 steel with coated carbide. $V = 80$ m/min, $f = 0.15$ mm/rev and $a_p = 0.8$ mm - Worn tool, $T = 40.06$ min .....	20
2.15a	Residual stress map under the combined influence of feed and radial depth of cut - residual normal stress along feed direction....	21
2.15b	Residual stress map under the combined influence of feed and radial depth of cut - residual normal stress along step-over direction.....	21
2.16a	Residual stress profile in turning Ti-6Al-4V at different conditions - sharp insert, 120 m/min, 0.25 mm/rev .....	23
2.16b	Residual stress profile in turning Ti-6Al-4V at different conditions - sharp insert, 120 m/min, 0.4 mm/rev .....	23
2.17a	Uncertainty of residual stress in turned Ti-6Al-4V samples - faced sample #1: in-depth residual stress profile .....	23
2.17b	Uncertainty of residual stress in turned Ti-6Al-4V samples - faced sample #2: in-depth residual stress profile .....	23
2.18a	The influence of milling parameters on surface residual stress - cutting speed influence.....	24
2.18b	The influence of milling parameters on surface residual stress - feed influence .....	24
2.19a	Residual stress in turning IN 718 at different conditions - speed: 40 m/min, new coated WC .....	26
2.19b	Residual stress in turning IN 718 at different conditions - speed: 40 m/min, new uncoated WC .....	26
2.19c	Residual stress in turning IN 718 at different conditions - speed: 40 m/min, worn coated WC.....	26
2.19d	Residual stress in turning IN 718 at different conditions - speed: 40 m/min, worn uncoated WC.....	26

2.20a	Subsurface microstructure by: new tool.....	26
2.20b	Subsurface microstructure by: worn tool.....	26
2.21a	Residual stress in turning Inconel 718 with coated and uncoated tools - $\sigma_{//}$ .....	27
2.21b	Residual stress in turning Inconel 718 with coated and uncoated tools - $\sigma_{\perp}$ .....	27
2.22	Effect of cutting edge preparation on RS [Honed-R (positive rake); Chamfered-A1 (negative rake); Sharp-A2 (negative rake)].....	28
2.23	Effect of nose radius [0.8 mm-A1(negative rake); 1.2 mm-B (negative rake); 1.6 mm-C (negative rake)] on the RS.....	29
2.24	Effect of different cutter orientations/workpiece tilt angle on residual stress.....	30
2.25	Machining ductile iron with random microstructures of 30-80 $\mu\text{m}$ .....	35
2.26	Machining AISI 52100 steel with random microstructures of 2-4 $\mu\text{m}$ .....	35
2.27	Residual stress evolution by sequential cuts (R1: during cutting; R2: after cooling; R3: after releasing forces; R4: residual stress).....	38
2.28	Comparison of predicted and measured residual stress.....	39
2.29	Predicted tangential residual stress profiles in subsurface in AISI 52100.....	39
3.1	On-line optical tool wear inspection system in milling.....	62
3.2	Schematic of tool wear zones (1: flank wear, 2: nose wear, 3: crater wear).....	65
3.3	Typical tool wear image.....	66
3.4	Flank wear evolution in dry hard milling AISI H13 (PVD coated inserts).....	68
3.5	Tool flank wear evolution in dry hard milling AISI H13 (PVD coated inserts).....	69

3.6	Tool chipping (PVD coated insert) .....	70
3.7	Flank wear evolution in milling Inconel 718 .....	72
3.8	Wear progression in milling Inconel 718 .....	73
3.9	Nose wear evolution in milling Inconel 718 .....	74
4.1a	Edge geometry of the milling cutter: Tool-holder .....	86
4.1b	Edge geometry of the milling cutter: Dimensions of cutting insert.....	86
4.1c	Edge geometry of the milling cutter: Tool edge before milling .....	86
4.1d	Edge geometry of the milling cutter: Tool edge after milling (Exp. #16).....	86
4.2a	Cutting loci in end milling: Cycloidal cutting locus in one pass .....	91
4.2b	Cutting loci in end milling: Overlapping cutting loci in consecutive pass.....	91
4.3a	Optical images of subsurface microstructure: sample 1 ~ sample 8.....	94
4.3b	Optical images of subsurface microstructure: sample 9 ~ sample 16.....	95
4.4	Micro-indentation array on the top surface .....	97
4.5	Surface microhardness variation in parallel and perpendicular to feed directions.....	97
4.6	Micro-indentation array in the subsurface .....	98
4.7a	Microhardness distributions in the subsurface: Axial depth-of-cut $a_p = 1.0$ mm.....	99
4.7b	Microhardness distributions in the subsurface: Axial depth-of-cut $a_p = 1.5$ mm.....	99
4.7c	Microhardness distributions in the subsurface: Axial depth-of-cut $a_p = 2.0$ mm.....	100
4.7d	Microhardness distributions in the subsurface: Axial depth-of-cut	

	$a_p = 2.5$ mm.....	100
4.8	Surface microhardness ( $HK_{0.05}$ ) contour under the combined influence of feed rate and radial depth-of-cut .....	102
4.9a	Residual stress contours under the combined influence of feed rate and radial depth-of-cut: Normal residual stress in feed direction .....	104
4.9b	Residual stress contours under the combined influence of feed rate and radial depth-of-cut: Normal residual stress in step-over direction .....	105
4.9c	Residual stress contours under the combined influence of feed rate and radial depth-of-cut: Shear residual stress.....	105
5.1a	Initial tool flank wear: Fresh tool (flank wear = 0).....	117
5.1b	Initial tool flank wear: Tool with flank wear = 0.1 mm.....	117
5.1c	Initial tool flank wear: Tool with flank wear = 0.2 mm.....	118
5.2	Texture of machined surface .....	120
5.3	Average, maximum, and minimum surface roughness ( $R_a$ ) in the feed and step-over directions.....	120
5.4a	Optical images of subsurface microstructure: sample #1 - sample # 6.....	123
5.4b	Optical images of subsurface microstructure: sample #7 - sample # 12.....	123
5.4c	Optical images of subsurface microstructure: sample #13 - sample # 21.....	124
5.5	Residual stresses at the machined surface.....	125
5.6a	Residual stresses distribution profiles: sample #4 .....	127
5.6b	Residual stresses distribution profiles: sample #5 .....	127
5.6c	Residual stresses distribution profiles: sample #6 .....	127
5.6d	Residual stresses distribution profiles: sample #10 .....	127

5.6e	Residual stresses distribution profiles: sample #11 .....	127
5.6f	Residual stresses distribution profiles: sample #12.....	127
5.6g	Residual stresses distribution profiles: sample #13 .....	128
5.6h	Residual stresses distribution profiles: sample #14 .....	128
5.6i	Residual stresses distribution profiles: sample #15 .....	128
5.7a	Microhardness profiles in the subsurface: Microhardness profile for samples 1 ~ 3.....	129
5.7b	Microhardness profiles in the subsurface: Microhardness profile for samples 4 ~ 6.....	130
5.7c	Microhardness profiles in the subsurface: Microhardness profile for samples 7 ~ 9.....	130
5.7d	Microhardness profiles in the subsurface: Microhardness profile for samples 10 ~ 12.....	131
5.7e	Microhardness profiles in the subsurface: Microhardness profile for samples 13 ~ 15.....	131
5.7f	Microhardness profiles in the subsurface: Microhardness profile for samples 16 ~ 18.....	132
5.7g	Microhardness profiles in the subsurface: Microhardness profile for samples 19 ~ 21 .....	132
5.8	MTS four-point bending fatigue testing system .....	134
5.9	Four-point bending fatigue testing configuration .....	135
5.10	Fatigue life vs. tool wear .....	136
5.11a	Cross-section of fatigued samples: Fatigued sample .....	140
5.11b	Cross-section of fatigued samples: Fatigue crack on fractured surface of sample #F1 (VB = 0) .....	140
5.11c	Cross-section of fatigued samples: Fatigue crack on fractured surface of sample #F2 (VB = 0.05 mm).....	140
5.11d	Cross-section of fatigued samples: Fatigue crack on fractured	

surface of sample #F3 (VB = 0.10 mm).....	140
5.11e Cross-section of fatigued samples: Fatigue crack on fractured surface of sample #F4 (VB = 0.15 mm).....	140
5.11f Cross-section of fatigued samples: Fatigue crack on fractured surface of sample #F5 (VB = 0.20 mm).....	140
6.1 On-line optical tool monitoring system for end milling .....	153
6.2a Fresh tool (flank wear = 0) .....	156
6.2b Tool with flank wear = 0.1 mm .....	156
6.2c Tool with flank wear = 0.2 mm .....	156
6.3 Texture of machined surface .....	158
6.4 Average, maximum, and minimum surface roughness ( $R_a$ ) in the feed and step-over directions .....	158
6.5 Optical images of subsurface microstructure .....	160
6.6a Microhardness profiles for samples 1 ~ 3 .....	161
6.6b Microhardness profiles for samples 7 ~ 9 .....	161
6.6c Microhardness profiles for samples 16 ~ 18.....	162
6.6d Microhardness profiles for samples 19 ~ 21 .....	162
6.7 Divided zones on top and bottom surfaces of the workpiece .....	164
6.8a Fresh tool (t = 0) .....	165
6.8b Tool after cutting 13 minutes .....	165
6.8c Tool after cutting 26 minutes.....	166
6.8d Tool after cutting 39 minutes .....	166
6.8e Tool after cutting 52 minutes.....	167
6.9 MTS four-point bending fatigue testing system.....	168
6.10 Schematic of four-point bending fatigue testing system.....	169

6.11	Fatigue life of the four end milled Inconel 718 samples.....	170
7.1a	Fresh tool (flank wear = 0) .....	184
7.1b	Tool with flank wear = 0.1 mm .....	184
7.1c	Tool with flank wear = 0.2 mm .....	184
7.2	Roughness ( $R_a$ ) in feed and step-over directions .....	185
7.3	Effect of feed on surface roughness at different tool wear levels .....	186
7.4	Effect of cutting speed on surface roughness at different tool wear levels .....	187
7.5	Comparison between the measured and predicted surface roughness.....	194

## CHAPTER 1

### INTRODUCTION

Tool wear is a complex phenomenon occurring in a cutting process. When a tool is used for cutting mechanical parts, a decision must be made whether a worn tool should be replaced by a new one before the next cutting, or if the worn tool can still be used but the cutting parameters need to be changed to adapt to the tool condition. Compared with a sharp tool, a worn tool will produce poor surface integrity and fatigue performance of the machined surfaces. Surface integrity and fatigue performance of the machined surfaces would deteriorate to an unacceptable level due to the progression of tool wear. The most conservative way to get components machined with desired quality is to replace the worn tool with a new one. However, this will increase manufacturing cost and reduce the production efficiency since more tools will be used and extra time for replacement will be spent. It is the primary objective for manufacturers to produce as many quality parts as possible while minimizing machining costs. In order to achieve multiple objectives of production efficiency, fatigue life, and manufacturing cost, the relationship between tool wear, surface integrity, and fatigue performance of machined components needs to be thoroughly studied to provide a general guidance for production.

Two basic types of tool wear will occur: flank wear (the portion of the tool in contact with the newly machined surface) and crater wear (the portion of the tool on the tool/chip interface). Generally, crater wear only has a minor effect on surface integrity of a machined

component unless it causes a cutting edge failure. Therefore, flank wear is always the most important wear mode when surface integrity is concerned. To capture the evolution of flank wear in machining process, a novel online optical tool inspection system has been developed in this research to integrate with a CNC machining center to monitor tool wear conditions in milling.

This dissertation proposal is a compilation of seven separate chapters. In addition to chapter 1 (Introduction), chapter 2 begins with a comprehensive review on surface integrity characterization and prediction in machining of hardened and difficult-to-machine alloys. Chapter 3 develops a novel online optical tool inspection system to monitor tool wear conditions in milling. The tool wear evolutions versus cutting time in end milling of AISI H13 tool steel and Inconel 718 superalloy were obtained and examined to demonstrate the function of the system. Chapter 4 focuses on finding the process design space for optimal surface integrity including microhardness and residual stresses in hard milling AISI H13 tool steel. Surface integrity of samples milled by tools with different flank wear conditions, including surface roughness, microstructure, residual stresses, and microhardness was characterized in chapter 5 to reveal the variation of surface integrity with respect to tool flank wear. Four-point-bending fatigue test was also conducted on end milled samples produced by tools with varied flank wear values to investigate the effect of flank wear on fatigue performance. Chapter 6 is dedicated to the effect of tool wear on surface integrity and fatigue performance of end milled Inconel 718 samples. Surface roughness, microstructure, and microhardness were characterized to reveal the evolutions of surface integrity with respect to tool flank wear. Fatigue performance of end milled samples produced by tools with different flank wear values was determined by four-point-bending fatigue test. Finally, chapter 7 proposes a predictive model for end milled surface

roughness from the experimental results in chapter 6. Both process parameters (cutting speed, feed per tooth, radial depth of cut) and tool wear have been incorporated in the model.

## CHAPTER 2

### SURFACE INTEGRITY CHARACTERIZATION AND PREDICTION IN MACHINING OF HARDENED AND DIFFICULT-TO-MACHINE ALLOYS: A STATE-OF-ART RESEARCH REVIEW AND ANALYSIS

#### Abstract

This chapter presents a review of the state-of-art research on surface integrity characterization, especially the characteristics of residual stresses produced in machining of hardened steels, titanium and nickel-based superalloys using the geometrically defined tools. The interrelationships among residual stresses, microstructures, and tool-wear have been discussed. Current research on residual stress modeling and simulation using finite element method has been critically assessed. Also, the rationale for developing multi-scale simulation models for predicting residual stresses in machining has been presented. At the end, possible future work has been proposed.

## 2.1. Definition, sources, and effects of residual stresses

Residual stresses are stresses that remain in a solid body after the external loading (mechanical and thermal) has been removed. The basic mechanism of machining-induced residual stresses was studied and reported in several pioneering research publications [40,15,25-27,51-54,10-11,45-46]. Residual stress (RS) stems from inhomogeneous material deformation which can be caused by mechanical loading, thermal gradient, and phase transformation in a machining process. Residual stresses are self-equalizing, i.e., the resultant force and the moment that they produce must be zero. Generally, RS can be classified into two types according to the distance or range over which they can be observed. The first kind of RS can be termed macro residual stress, which is prevalent in the order of hundred microns in the subsurface. The second kind is often called micro residual stress covering a distance of a few grains or a part of a grain.

Residual stress also has close relationships with other surface integrity factors characterizing mechanical, metallurgical, chemical, and topological states of a machined surface. Residual stress has been generally recognized as the key factor among all surface integrity parameters significantly influencing the product performance such as fatigue life as shown in Figure 2.1 [73], creep, corrosion, and dimensional accuracy of a machined component.

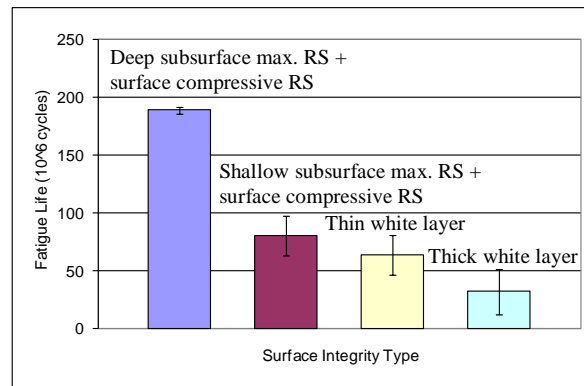


Fig. 2.1 The effect of surface integrity produced in hard turning on rolling contact fatigue life [73].

The influence of RS may be either beneficial or detrimental, depending upon its magnitude, pattern, and distribution. Unfortunately, the presence of RS generally goes unrecognized until a malfunction or failure occurs. It has been shown that compressive stresses are usually beneficial to fatigue life, creep life and resistance to stress corrosion cracking, whereas tensile RS are usually detrimental to these same properties [23]. Brinksmeier et al. [10] gave a good summary of the most important effects of RS on mechanical and electrical components, see Figure 2.2.

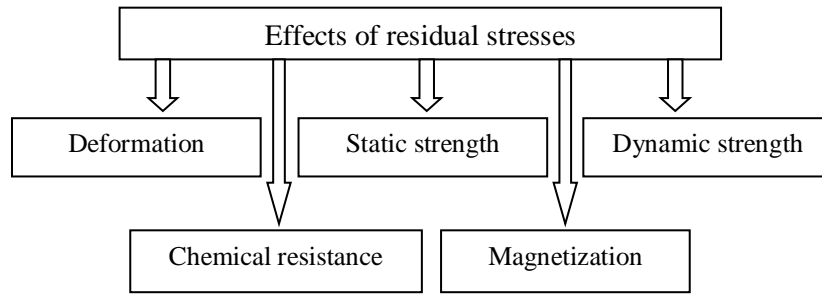


Fig. 2.2 Effects of residual stress [10].

Residual stresses not only significantly affect product performance, but also serves as a key criterion for process selection [96], for example hard turning vs. grinding, for making precision components. In addition, the measurement of residual stresses is expensive, time consuming, and tedious. Hence, the characterization and prediction of residual stresses for improving product performance has great economic as well as scientific importance.

## 2.2. Experimental characterization of residual stresses in machining of hardened and difficult-to-machine alloys

### 2.2.1. RS measurement methods and issues

Various quantitative and qualitative techniques for measuring RS have been developed over the last few decades. Generally, the measuring methods for RS have been categorized as destructive or nondestructive. Obviously, nondestructive RS measurement is always preferred. For a RS depth analysis, all methods, however, require a partial or complete destruction of the specimen; therefore, a distinction as to direct and indirect measuring methods is more effective would be needed [88,89]. Lu [56] summarized the general methods for measuring residual stresses and their respective characteristics, see Table 2.1.

In the present study, three measurement techniques are used to evaluate the residual stresses: X-ray diffraction method, the neutron diffraction method, and the incremental hole drilling method. The experimental results obtained from the first two techniques are quite similar. Only the residual stresses in the different phases (matrix and reinforcement) can be separately analyzed. The main advantage of the neutron diffraction method is its high penetration capacity for inspecting material up to several millimeters in depth. The disadvantages of such a technique are the high cost and the low spacing resolution. A combination of several techniques is more efficient for a better understanding of the formation mechanism of the residual stress. The incremental hole drilling method is a useful technique for studying large grain size matrix material, but it cannot deal with the residual stresses in the different phases of the material. The use of X-rays is one of the most popular techniques for residual stress measurement. It is a non-destructive technique of evaluating residual stress. With layer removal, the in-depth residual stress distribution can also be analyzed. It is also an efficient tool for studying the evolution of residual stress in a mechanical structure under static or dynamic loading.

Table 2.1 General comparison of residual stress measuring methods [56].

Method	X-ray	Neutron diffraction	Ultrasonic	Magnetic	Hole drilling	Deflection	Sectioning
<b>Nature</b>	Nondestructive	Nondestructive	Nondestructive	Nondestructive	Destructive	Destructive	Destructive
<b>Hypothesis</b>	Isotropic, homogeneous, fine grain polycrystalline material	Isotropic, homogeneous, polycrystalline material	Isotropic, homogeneous material, homogeneous stresses on the acoustic path between the transmitter and receiver	Ferromagnetic material	Biaxial uniform stresses on the surface of the hole	Biaxial uniform stresses on rectangle whose length and width are sufficiently large	3D stress field
<b>Type of residual stresses analyzed</b>	First and second or third kind	First and second kind	First, second, and third kind	First, second, and third kind	First kind	First kind	First kind
<b>Parameters measured</b>	Change in the interplanar spacing of the polycrystalline	Change in the interplanar spacing of the polycrystalline	Variation of ultrasonic wave speed	Noise amplitude or magnetic permeability	Surface strain or displacements	Strain or deflection	Surface strain or displacements
<b>Minimum analysis zone</b>	0.5 mm <sup>2</sup>	4 mm <sup>2</sup>	0.1 – 30 mm <sup>2</sup>	1 – 100 mm <sup>2</sup>	0.5 mm <sup>2</sup>	100 – 1000 mm <sup>2</sup>	100 mm <sup>2</sup>
<b>Inspection depth</b>	1 – 50 um	2 – 50 mm	0.015 – 3 mm	0.1 – 1 mm	0.02 – 15 mm	0.1 – 3 mm	> 1mm
<b>Precision</b>	± 20 MPa	± 30 MPa	10 – 20 MPa	10 – 20 MPa	± 20 MPa	± 30 MPa	± 10MPa

### 2.2.2. The effect of work material on residual stress

This review focuses on hardened steels and difficult-to-machine alloys since they are of great interests in automotive, aerospace, and biomedical industries. The characterization of residual stress in machining aluminum and soft steel alloys has been reported in previous publications. Hardened steels refer to a group of alloys over 35 HRC after quenching and tempering, while the difficult-to-machine alloys can be classified into three major categories: titanium-based alloys, nickel-based alloys (e.g., Inconel), and iron-based alloys (e.g., austenitic stainless steels) that require higher cutting energy when compared with low-strength alloys (e.g., plain carbon steel). Residual stress characteristics in machining the iron-based austenitic stainless steels have been well documented in a recent review by M'Saoubi et al. [63]; therefore, it will not be covered in this work. Although several review papers [10,49,57,90] covered various

aspects of surface integrity, only few publications focus on residual stresses produced from machining with tools with geometrically defined cutting edges.

### 2.2.3. Hardened steel alloys

Hard machining, i.e., machining hardened steels ( $> 35$  HRc), has been used since the early 1980's. Competing with grinding as a finishing process for machining industry making bearings, gears, cams, shafts, pinions, dies, molds, tools, etc., hard machining is cheaper, faster, more flexible, and more environmentally friendly in many cases. Machining-induced surface integrity, including subsurface residual stresses, microstructure alteration and changes in mechanical behavior, is critical for component performance such as fatigue life and stress corrosion. Hard machining is a cluster of processes including hard turning, hard milling, hard drilling, to name a few.

#### 2.2.3.1. Hard turning

Matsumoto et al. [60] initiated the study on the effect of material hardness on the residual stress in the turned surface of AISI 4340. They concluded that the increase in hardness produces compressive residual stress at the surface and deep compressive residual stress in the subsurface as shown in Figure 2.3. They supposed that the mechanical deformation caused by the cutting tool would be responsible for the variation of the residual stress pattern in the machined surface.

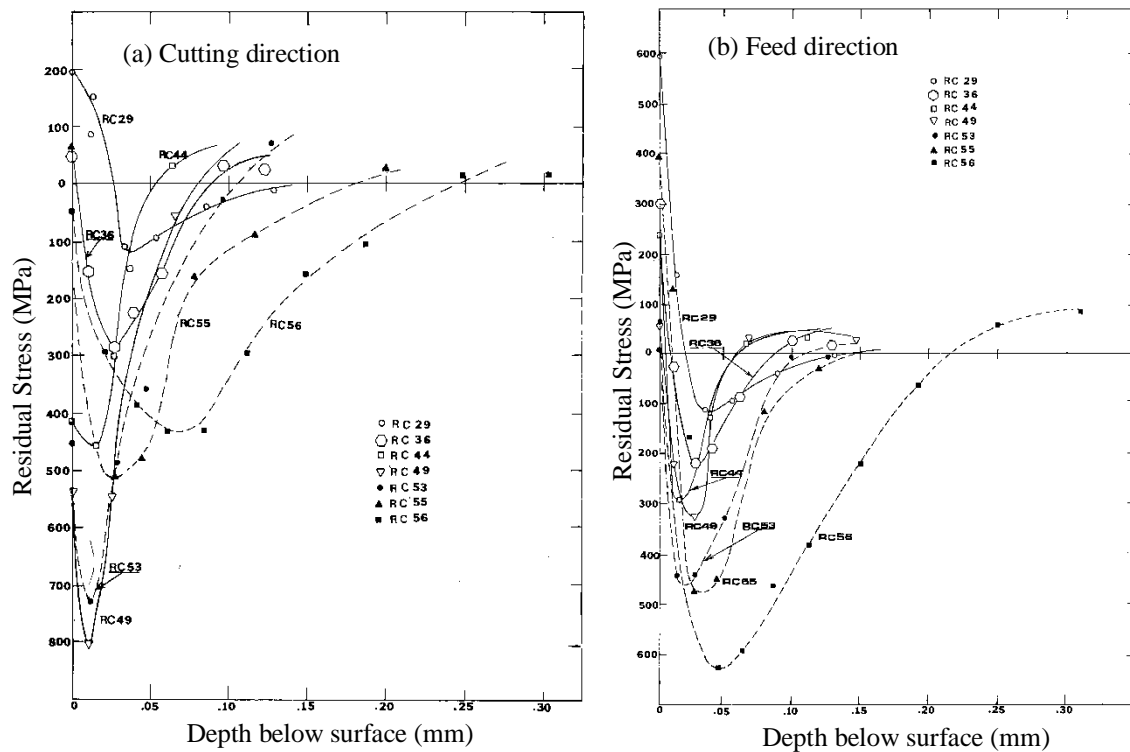


Fig. 2.3 Effect of hardness on residual stress distribution in the subsurface in turning hardened AISI 4340 steel (300 fpm, 0.006 in. depth of cut, 0.035/rev feed) [60].

In a subsequent work, Matsumoto et al. [61] found that the tool edge geometry is the dominant factor determining the residual stress profile in hard turning of AISI 52100 with a sharp tool, a 0.02mm honed tool, a tool with major chamfer of 15 degree, and a tool with double chamfer geometry. They compared the residual stress profile created by these tools and found that the honing clearly creates a deeper compressive residual stress, while the double chamfer tool can produce similar results as shown in Figures 2.4 and 2.5.

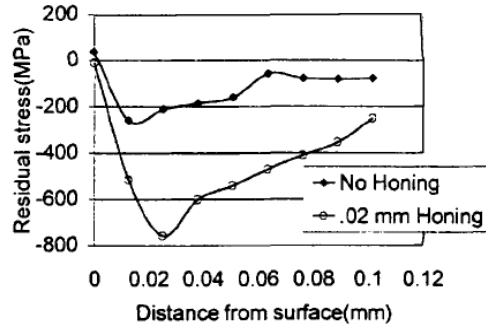
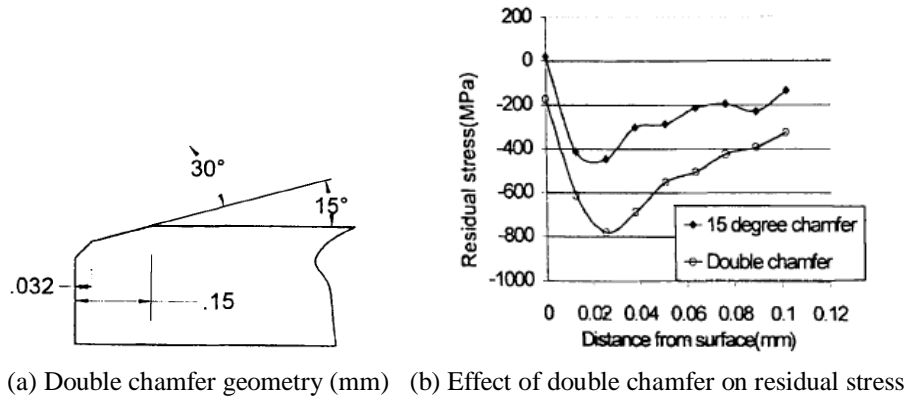


Fig. 2.4 Tool edge honing effect on residual stress in hard turning AISI 52100 [61].



(a) Double chamfer geometry (mm) (b) Effect of double chamfer on residual stress

Fig. 2.5 The effect of cutting edge chamfer on residual stress [61].

Dahlman et al. [17] described how rake angle and cutting parameters affect the RS in turning AISI 52100. The RS were measured using the XRD method in both cutting ( $V_c$ ) and feed direction ( $f$ ). Four values of rake angle ( $-6^\circ$ ,  $-21^\circ$ ,  $-41^\circ$ ,  $-61^\circ$ ) had been applied in the experiment and the RS profiles obtained for these conditions are from Figure 2.6. They drew the conclusion that a larger negative rake angle gives higher compressive stresses, as well as a deeper affected zone below the surface, and showed that the maximum stress position can go deeper into the material with increased rake angles.

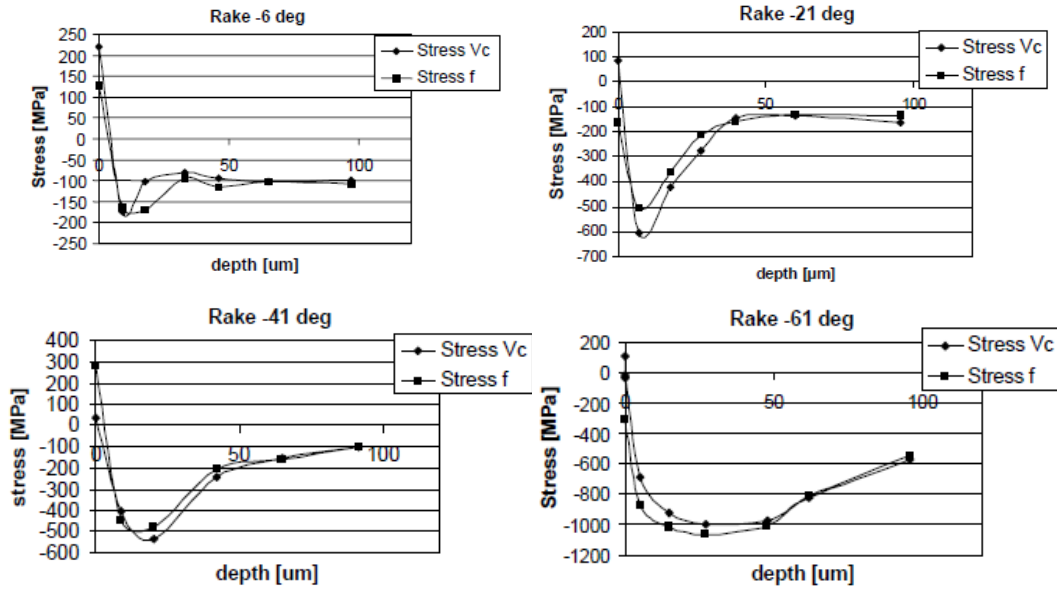
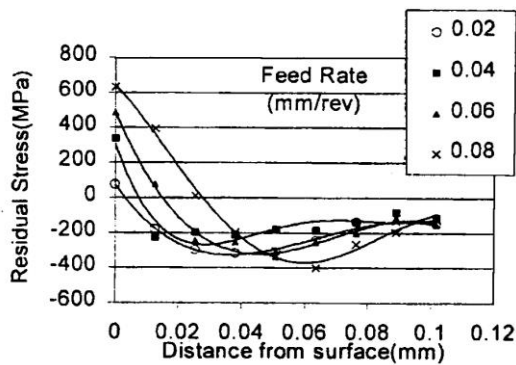
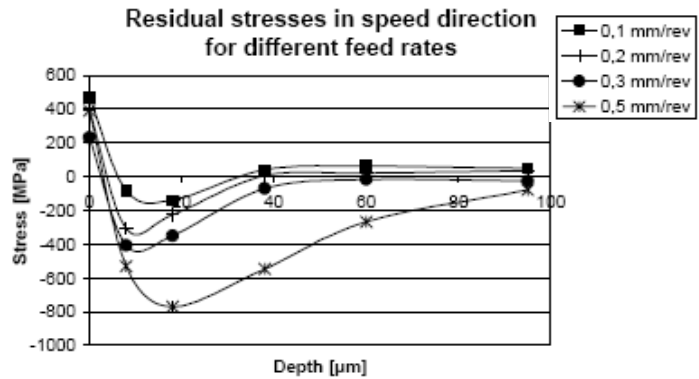


Fig. 2.6 RS distribution in hard turning AISI 52100 with different rake angle [17].

It has been found that the feed rate does not change the pattern of a residual stress profile in Figure 2.7 [61,17]. However, it can be observed that a small feed generated a larger tensile RS at the surface, but a shallower maximum compressive RS in the subsurface. Also, Figure 2.8 shows that the depth of cut does not affect the magnitude of residual stress or the profile.

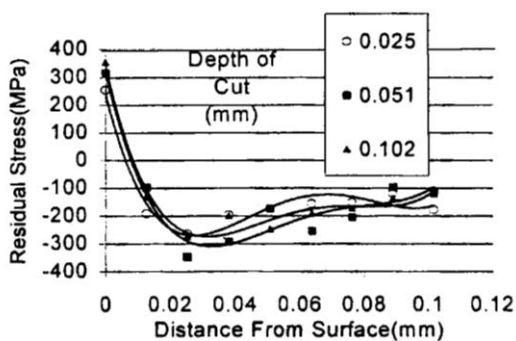


(a) Matsumoto et al. [61]

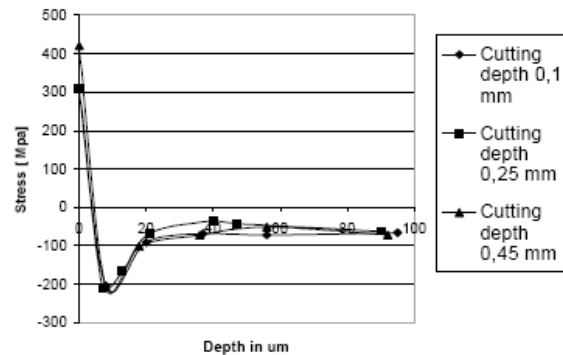


(b) Dahlman et al. [17]

Fig. 2.7 The effect of feed on residual stress profiles in hard turning.



(a) Matsumoto et al. [61]



(b) Dahlman et al. [17]

Fig. 2.8 The effect of depth of cut on residual stress profiles in hard turning.

As tool-wear is inevitable in machining, several studies have found that tool-wear may induce white layer, a thermally-induced, phase transformed layer. Residual stress is attributable to tool-wear land developed on the flank surface of the tool. Tensile residual stress does not occur at the surface unless considerable tool-wear or cutting time has elapsed as shown in Figure 2.9. When a tool-wear induced white layer occurs, high tensile residual stress appears at the top

surface shown in Figure 2.10. Therefore, tensile residual stress primarily depends on the extent of tool flank wear land  $VB$ . The increase of wear land shifts compressive residual stress to tensile at the surface and the maximum compressive residual stress to the deeper subsurface.

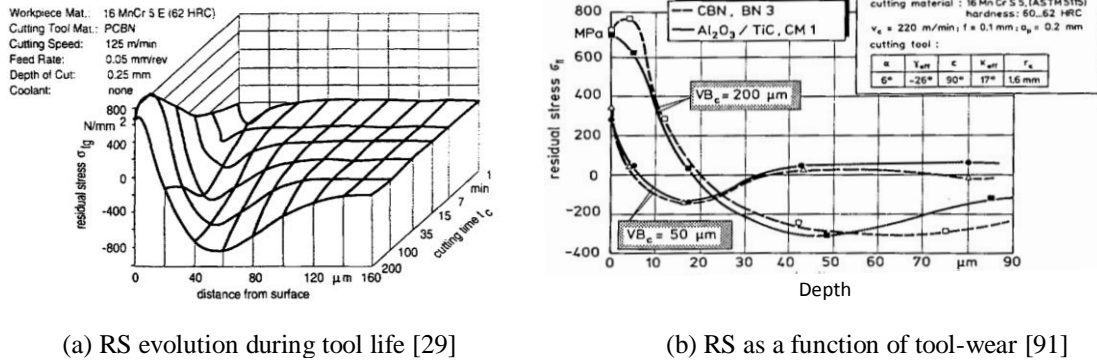


Fig. 2.9 The effect of tool-wear on residual stress profile.

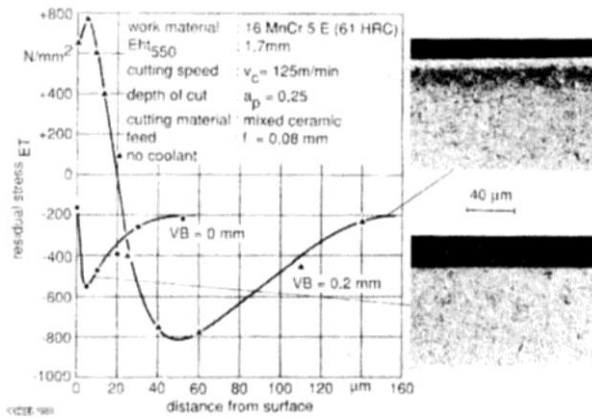


Fig. 2.10 Tool-wear effect on residual stress [50].

Since the basic objective to use hard turning is to replace grinding, a comparison of residual stress produced from turning vs. grinding would be necessary to justify the replacement. Warren and Guo [97] have shown the comparison of residual stress for the different subsurface

microstructures in hard turning and grinding, and for heat treated workpiece (quenched and tempered) – see Figures 2.11 and 2.12.

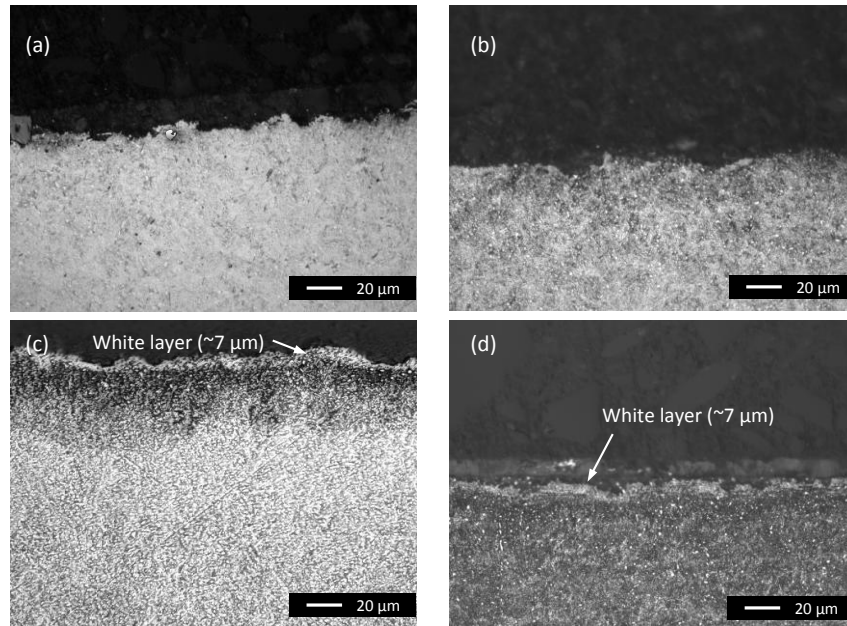


Fig. 2.11 Microstructures of the cross-sectional surfaces: (a) hard turned fresh (HTF), (b) ground fresh (GF), (c) hard turned with white layer (HTWL), (d) ground with white layer (GWL) [97].

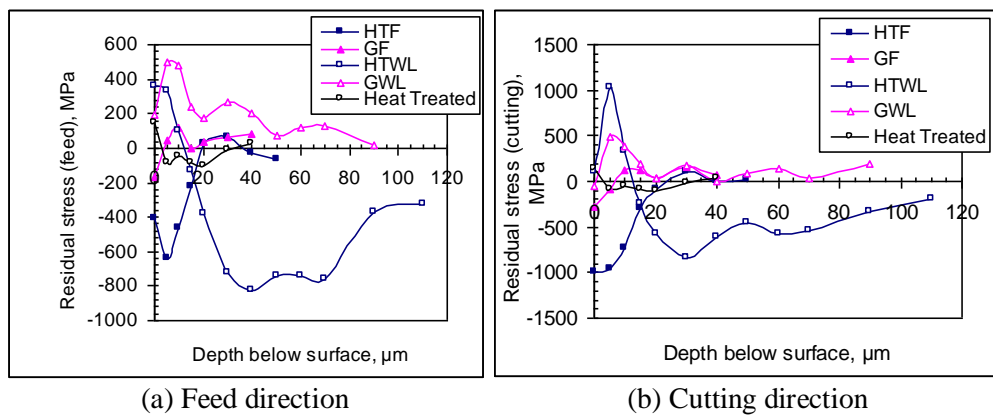


Fig. 2.12 Comparison of residual stress profiles for different surface microstructures [97].

The most significant differences in the characteristics of residual stress profiles obtained from hard turning and grinding are manifested in several aspects: (a) Hard turning with a fresh tool generates a “hook” shaped residual stress profile characterized by surface compressive residual stress and maximum compressive residual stress in the subsurface. Gentle grinding only generates maximum compressive residual stress at the surface. The magnitude of residual stress and the affected depth generated in hard turning is much larger than those for grinding; (b) Hard turning with a worn tool generates a high tensile stress in the area of the thermal white layer. The high Hertz pressure and the rapid temperature change in the subsurface, in the case of a worn tool, makes the residual stress more compressive and deeper into the subsurface than the turned one with a fresh tool. Abusive grinding also produces tensile residual stress, but has similar profile shape to that of the GF surfaces; (c) Tensile residual stress in the area of white layer in hard turning was higher than that for the ground white layer. However, the residual stress for the ground white layer does not become compressive (as for the hard turned white layer), and remains tensile throughout the entire depth measured; and (d) Machining is the deterministic factor for the resulting residual stress magnitudes and profiles compared with the minor influence of initial residual stress by heat treatment.

#### 2.2.3.2. Hard milling

Hard milling is another major process in the cluster of hard machining processes. Traditionally, the manufacturing of dies and molds involves end milling annealed (soft) steels, heat treatment (hardening), electro discharge machining (EDM), and finish grinding/hand polishing. However, the process chain is very time-consuming, expensive and environmentally hazardous. Furthermore, the machined surface by EDM or grinding process is prone to thermal damage. Hard milling, i.e., milling alloys steels at hardened state (40–60 HRc), provides

substantial potential advantages of hard milling over traditional EDM or grinding in terms of reduction of machining costs, lead time and number of necessary machine tools, increase of material removal rate, elimination of part distortion by heat treatment, as well as improved surface integrity. Hard milling has emerged as a competitive finish or semi-finish technology in the manufacture of dies and molds [105].

In hard milling, a number of die and mold steel alloys such as hot-working H13 and cold-working D2 and P20 has been investigated. Axinte and Dewes [4] studied the residual stress developed along the tool feed direction in high speed down milling AISI H13. The workpiece angle were chosen as  $\alpha = 0^\circ$  and  $\alpha = 60^\circ$ . Major experimental parameters used in this work are shown in Table 2.2. The experimental results for residual stress are presented in Figure 2.13(a) (Test 1-4) and Figure 2.13(b) (Test 5-8). It can be seen that highly compressive surface residual stress appears at the surface and higher workpiece angle cause lower compressive stress. During milling AISI H13 at different cutting parameters, it was found that cutting speed and feed per tooth were the significant factors affecting the surface residual stresses. Increasing cutting speed and feed per tooth caused the compressive stresses to decrease due to a likely increase in thermal effect on the machined surface [4]. The tool geometry changes the contact length between the tool and the workpiece as well as the cutting temperature and cutting forces; thus the different tool geometries results in different residual stresses profile [59].

Table 2.2 Experimental matrix [4].

$\alpha$ (°)	$f_z$ (mm/tooth)	$v$ (m/min)	
		200	300
0	0.05	Test 1	Test 2
	0.10	Test 3	Test 4
60	0.05	Test 5	Test 6
	0.10	Test 7	Test 8

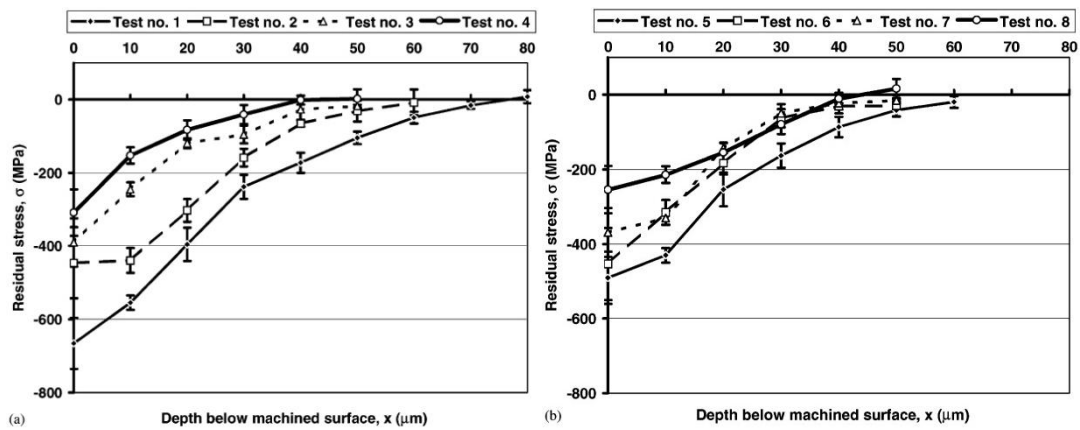


Fig. 2.13 RS vs. depth below surface when workpiece angle: (a)  $\alpha = 0^\circ$ ; (b)  $\alpha = 60^\circ$  [4].

When compared with hard turning, the “hook” shaped residual stress profile does not occur in Figure 2.13. In contrast, Chandrasekaran et al. [13] have shown that “hook” shaped residual stress profiles do happen in hard milling of H13 as shown in Figure 2.14 and D2 steels. Also, it has been seen that even a strong change in composition (reduction in  $Cr$  to 8%) did not affect the residual stress profile to any great extent after milling.

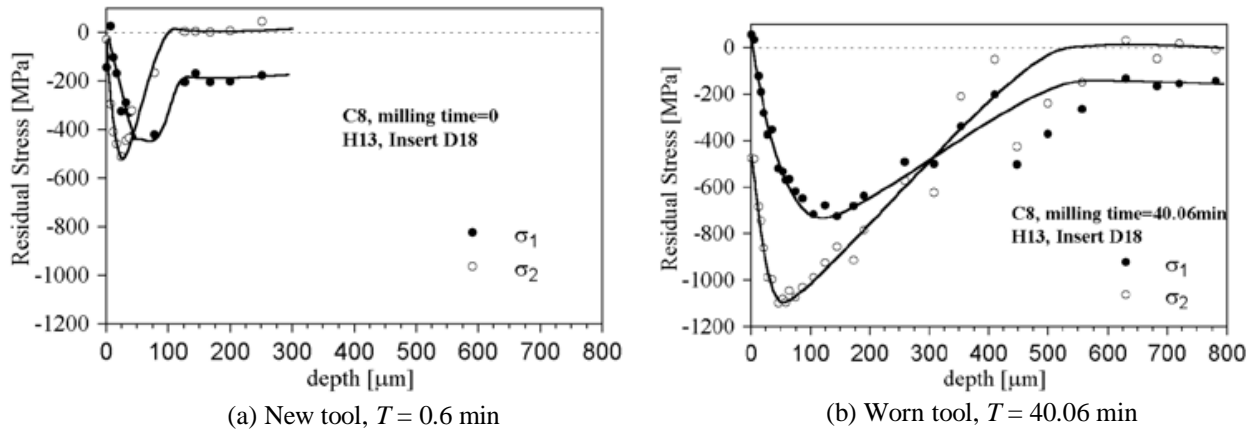


Fig. 2.14 Effect of tool-wear on residual stress profile in milling of H13 steel with coated carbide.  $V = 80$  m/min,  $f = 0.15$  mm/rev and  $a_p = 0.8$  mm [13].

Zhang and Guo [106] developed a process parameter space for target residual stress at the milled surface of H13 steel ( $50 \pm 1$  HRC) – see Figure 2.15, with respect to feed rate and radial depth of cut. They found that the residual normal stresses along feed and step-over directions increased with the increase of radial depth of cut or feed rate and they were all compressive which is beneficial for desired surface properties. They showed that the residual shear stresses can be neglected since their values were very small with respect to residual normal stresses.

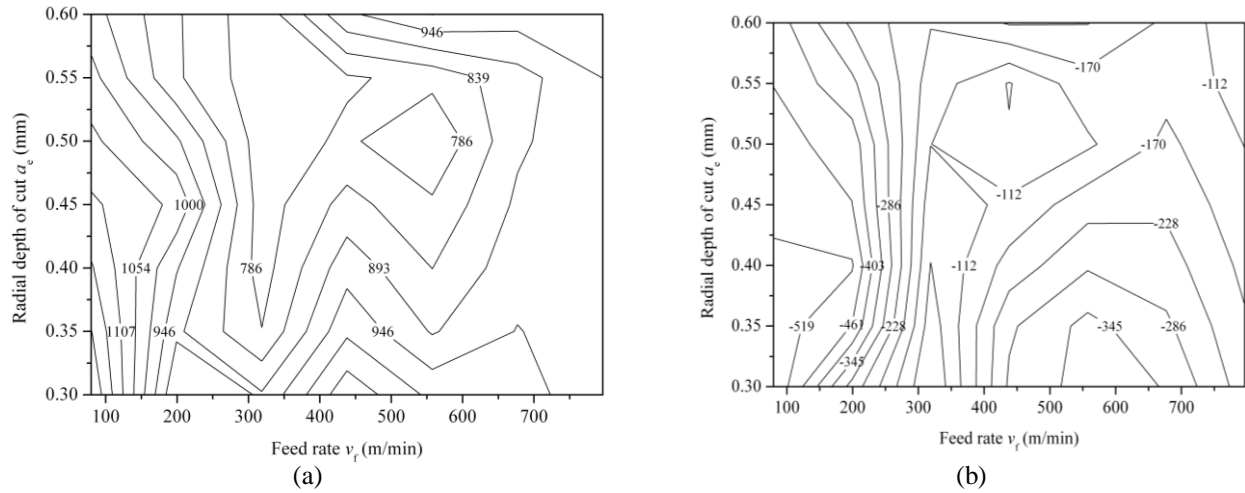


Fig. 2.15 Residual stress map under the combined influence of feed and radial depth of cut [106]; (a) residual normal stress along feed direction; (b) residual normal stress along step-over direction.

Elbestawi et al. [22] investigated the white layers formed in high-speed milling of hardened AISI H13 using PCBN ball-nose end mills, and found that the white layer was dependant on edge preparation and tool-wear. However, no white layers or other microstructural alterations were observed on the machined surfaces even with worn tools under the higher levels of cutting speed and feed rate when hardened H13 steel (HRc 47-49) was machined using *TiAlN* coated carbide tools [4].

## 2.2.4. Titanium alloys

### 2.2.4.1. Turning

Titanium alloys are widely used in aerospace, biomedical, and chemical industries primarily due to their exceptional strength to weight ratio [24], high temperature performance [109] and corrosion resistance [16]. For example, almost all titanium monolithic components in

aerospace industry are manufactured by milling [86]. However, titanium alloys are typically difficult-to-cut materials due to their high strength at elevated temperatures [48], low modulus, low thermal conductivity [41] and high chemical reactivity [85]. The machined titanium components such as compressors of aircraft engines require the greatest reliability which is determined by the process-induced surface integrity. However, surface integrity of milled titanium components easily deteriorates due to the poor machinability of titanium alloys and cyclic chip loading during milling. Milling-induced surface integrity, including anisotropic surface roughness, residual stress, surface microstructure alterations and microhardness, has received little attention. A brief review of the state-of-the-art knowledge on surface integrity of machined titanium components is summarized as follows.

An early study by Zlatin and Field [108] shows that an abusive milling produced tensile residual stress in the machined layer, while a gentle milling was shown to produce compressive residual stress. Narutaki et al. [64] reported that surface residual stress increased with the increase of cutting speed. The magnitudes of residual stresses in dry machining of *Ti-6Al-4V* were also larger than those produced by wet cutting. Hughes et al. [44] studied the effect of cutting tool material and edge geometry on workpiece surface integrity in turning of *Ti-6Al-4V*. The residual stress distributions for machining with sharp and worn tools at different turning parameters have been studied – see Figure 2.16.

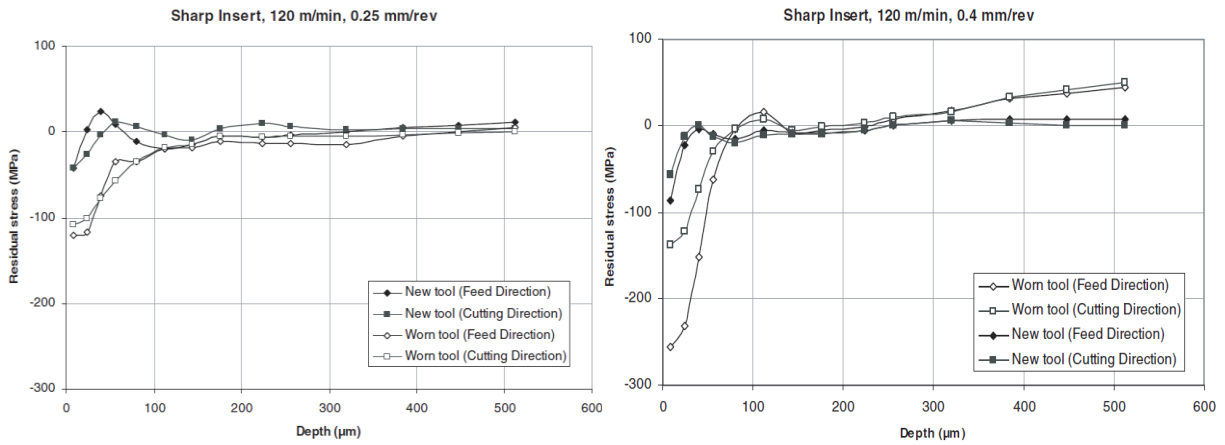


Fig. 2.16 Residual stress profile in turning Ti-6Al-4V at different conditions [44].

Yang et al. [100] found that residual stress on the ground *Ti-6Al-4V* surfaces has a larger scatter than that of the face turned ones in a statistical sense – see Figure 2.17. X-ray diffraction technique was employed to determine the residual stress profiles and the scatter of residual stress has been considered in the measurement process.

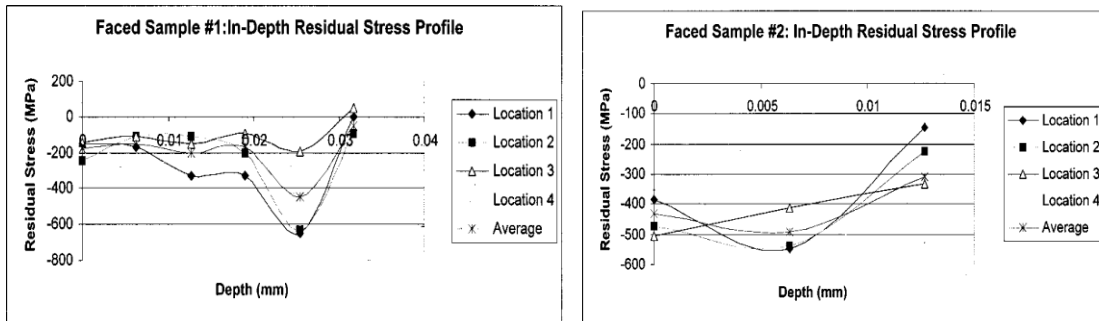


Fig. 2.17 Uncertainty of residual stress in turned Ti-6Al-4V samples [100].

### 2.2.4.2. Milling

Narutaki et al. [64] reported that surface compressive residual stress increased with the increase of cutting speed and the magnitudes of residual stresses produced in dry machining of *Ti-4Al-6V* were also larger than those from wet machining. A comprehensive experimental study on surface integrity of *Ti-6Al-4V* has been performed by Sun and Guo [87]. They report the influence of end milling parameters (including cutting speed and feed) on surface residual stress in the two directions – see Figure 2.18, for milled surfaces free of the white layer.

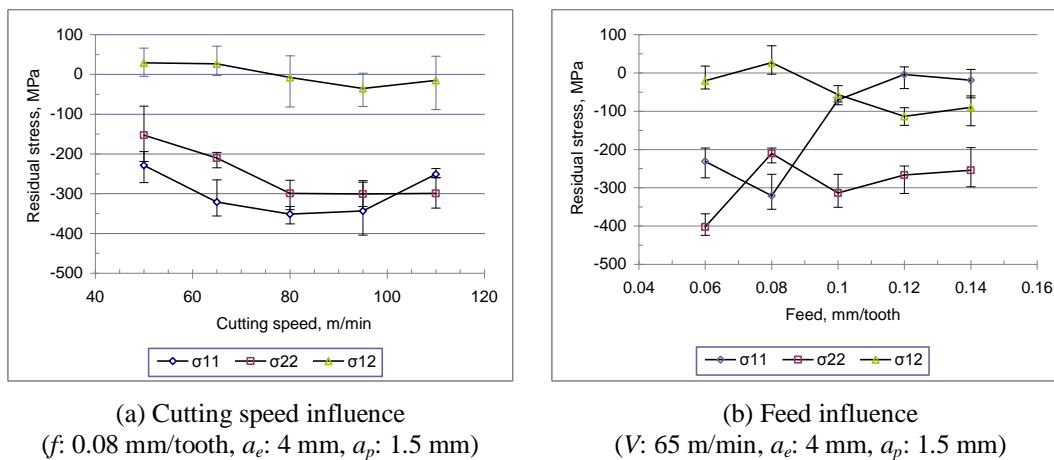


Fig. 2.18 The influence of milling parameters on surface residual stress [87].

### 2.2.5. Nickel-based alloys

#### 2.2.5.1. Turning

Similar to titanium alloys, the nickel-based superalloys are capable of retaining high mechanical and chemical properties at elevated temperatures which make them ideal materials in making aero-engine components, marine equipment, nuclear reactors, petrochemical equipment, food processing equipment, and pollution control apparatus. Inconel 718 is one popular nickel

superalloy widely used in aerospace industry. Due to the significant hardening effects induced by large strains and high strain-rates, Inconel 718 is a typical difficult-to-cut material. The critical issues in machining nickel-based superalloys are short tool-life and poor surface integrity.

Sharman et al. [74] reported hook-shaped residual stress profiles (Figure 2.19), with tensile stress at the surface for both  $TiCN/Al_2O_3/TiN$  coated and uncoated fresh  $WC$  tools. Both sharp and worn uncoated  $WC$  tools produce less tensile residual stresses than those by the coated tools. In addition, it is expected that the worn coated  $WC$  tools produce more tensile residual stress at the surface than the fresh  $WC$  ones. However, it is very interesting to note while the worn uncoated  $WC$  tools produces more compressive residual stress at the surface than those by the new uncoated  $WC$  tools. The subsurface microstructural damage caused by turning Inconel 718 was shown in Figure 2.20.

Tool coating may act as a thermal barrier to block heat dissipation into the cutting tool; therefore, the high surface temperature tends to produces higher tensile residual stress. Similarly, ceramic cutting tools suffer similar issues of thermally-induced high tensile residual stress. Arunachalam et al. [1] investigated the influence of  $CBN$  and mixed alumina ceramic tools on the RS when facing age hardened Inconel 718. They found that ceramic tools cause much higher tensile RS as compared to  $CBN$  tools due to the poor thermal conductivity of ceramic tools, leading to higher values of residual stresses caused by the dominance of thermal effects. In contrast, Outeiro et al. [68] reported that  $TiAlN$  coated  $WC$  tools produce lower surface tensile stress than the uncoated tools (Figure 2.21). They reported that the contradictory trends of residual stress could be attributed to the different coatings.

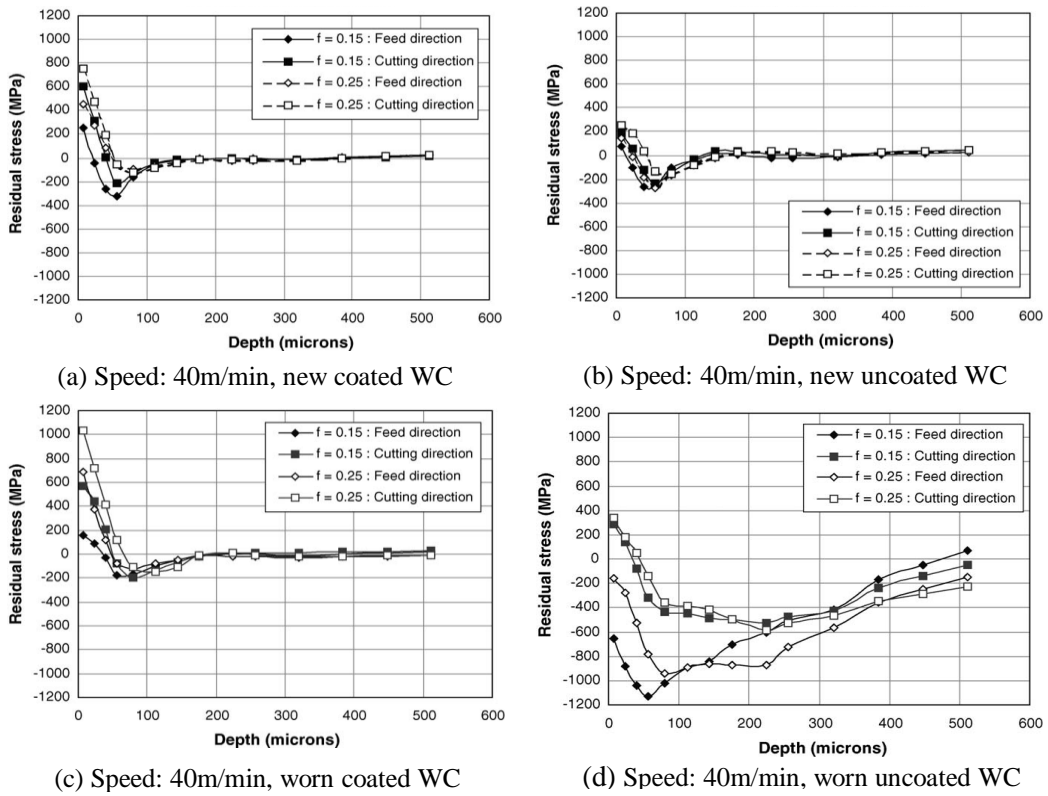


Fig. 2.19 Residual stress in turning IN 718 at different conditions [74].

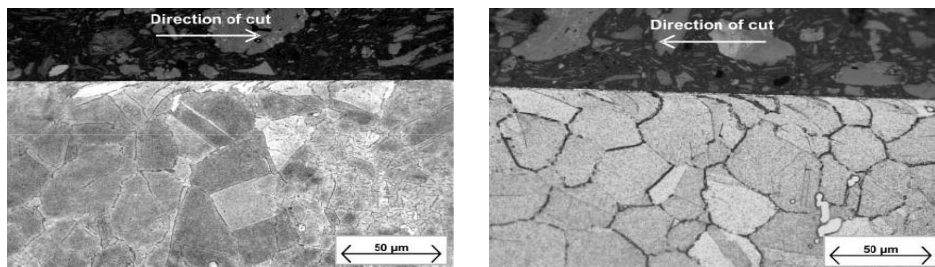


Fig. 2.20 Subsurface microstructure by: (a) new tool; (b) worn tool [75].

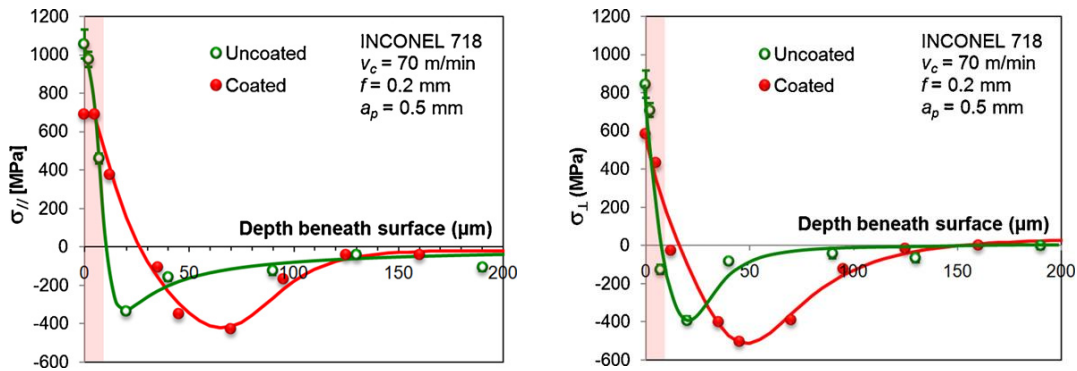


Fig. 2.21 Residual stress in turning Inconel 718 with coated and uncoated tools [68].

The effect of cutting edge preparation which includes honed, chamfered and sharp cutting edges, and the effect of nose radius on the RS were examined by Arunachalam et al. [2] when machining with coated carbide cutting tools. In the case of both wet and dry machining of Inconel 718, a sharp cutting edge results in higher values of tensile RS than the honed cutting edge, while chamfered cutting edge generates compressive RS, as shown in Figure 2.22. These differences in the RS can be explained by the model developed by Syren as cited by Brinksmeier et al. [10] that surfaces generated by a cutting operation without a following squeezing have tensile stresses, while surfaces, which are squeezed, and thus plastically deformed, have compressive stresses. They explained that using honed and chamfered edge will induce a plastically deformed layer, and thus would result in lower tensile RS or even compressive RS.

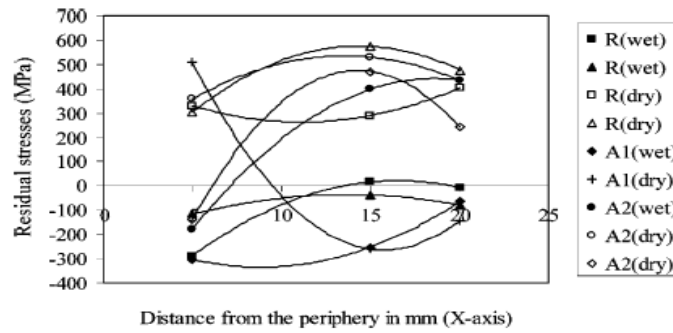


Fig. 2.22 Effect of cutting edge preparation on RS [Honed-R (positive rake); Chamfered-A1 (negative rake); Sharp-A2 (negative rake)] [2].

The experimental result of the effect of nose radius on the RS is depicted in Figure 2.23. From the RS profiles, in both wet and dry cutting conditions, the smallest nose radius (0.8mm) resulted in compressive RS while the larger radius i.e., 1.2 and 1.6mm resulted in tensile RS. For radii 1.2 and 1.6mm, 1.2mm showed higher values of tensile RS. Generally, compressive RS can be obtained by using a rounded edge tool due to the ploughing effect. They gave one possible explanation for this phenomenon as that the contact area in a large radius insert is larger than a smaller radius and so more frictional heat would be generated in the cutting operation [1]. Another likely reason shown was that there must be a turning point or critical value for transition from compressive RS to tensile RS, or for transition from decrease to increase within the tensile range, with respect to edge radius which would be beneficial to designing the tool edge.

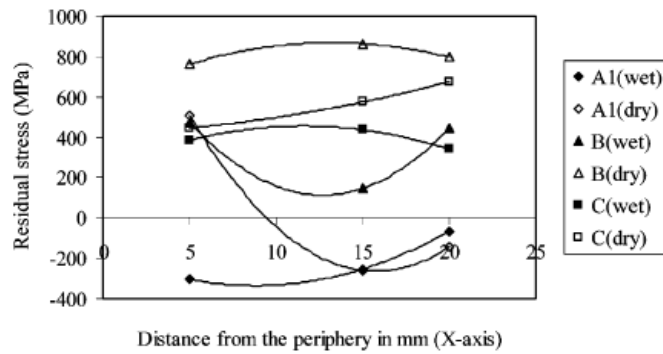


Fig. 2.23 Effect of nose radius [0.8mm-A1 (negative rake); 1.2mm-B (negative rake); 1.6mm-C (negative rake)] on the RS [2].

### 2.2.5.2. Milling

Aspinwall et al. [3] conducted a comprehensive series of experiments on the effects of cutter orientation, workpiece angle on machinability in high speed milling of Inconel 718. It was found that compressive surface residual stress was generated when a horizontal upwards cutter orientation was employed, while a tensile stress would be observed by employing a horizontal downwards operation. The residual stress profiles in feed direction are shown in Figure 2.24.

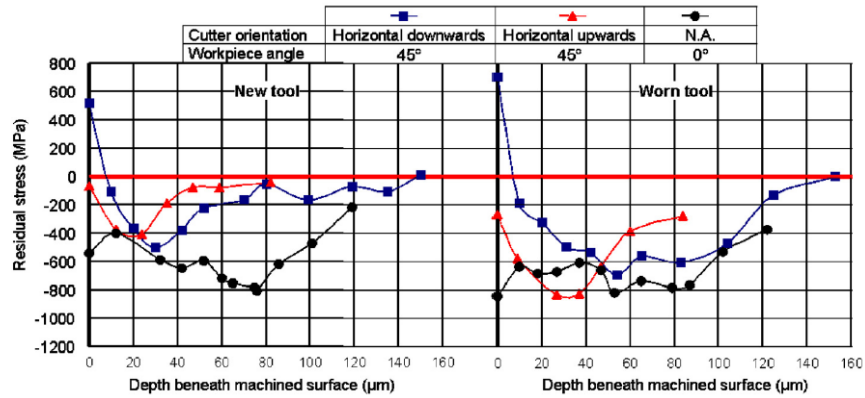


Fig. 2.24 Effect of different cutter orientations/workpiece tilt angle on residual stress [3].

### 2.3. An assessment of current residual stress prediction by finite element simulation

#### 2.3.1. Material property determination

The material properties are essential inputs to accurately predict residual stresses in any finite element analysis (FEA) and other analytical modeling of machining processes. In addition, modeling development is one thing, and the methods to determine dynamic material properties encountered in machining is quite another. Obtaining the necessary material property data has been identified as one of two key problems for the future of computational mechanics of the machining process [93].

Average flow stress properties of the work material in a small range of large strain, high strain-rate and temperature in machining have been investigated using machining tests coupled with predictive machining models [69,82,76]. Alternatively if one has an accurate constitutive model which fits the parameters of the model using a few cutting tests, it would be a perfect method. However, this constitutive model is not yet available, despite significant advances and efforts.

For the time being, either method discussed above is thought impractical to get the complete data needed for a comprehensive and accurate FEA analysis. It would be far better, from the viewpoint of attempting to predict machining responses, if this could be done using material properties obtained from an independent test. Conducting independent material testing at elevated temperature and extrapolating experimental data to machining range is a feasible approach to approximate the material behavior in machining. The material properties are also homogeneous from the tensile or compression testing. Spaans [80] was one of the early researchers to use the Split Hopkinson method to estimate mechanical properties of the work material in metal cutting. Torsional Hopkinson bar tests were conducted to measure stress-strain properties relevant to machining and high speed forming [81]. Split Hopkinson bar impact testing has been used to obtain the flow stress data of the materials under elevated temperature and relatively low strain-rate (below  $2000 \text{ s}^{-1}$ ) [79,102]. However, the testing system is very complex.

An integrated approach based on compression and cutting experiments has also been developed to characterize the mechanical behavior of work materials in machining [83,82,31]. It is also confirmed that the compression data can be correlated with the cutting data. The developed approach is valid for machining with continuous chips at a variety of cutting speeds. Guo and Liu [34] proposed the method of tensile tests at elevated temperatures coupled with the concept of velocity-modified temperature to approximate material properties of hardened AISI 52100 steel in hard machining by using of this method.

The pros and cons of compression, tension, or torsion tests may be evaluated in terms of the achieved temperatures, strains, strain-rates, and specimen dimensions. Material properties

from each test need to be extrapolated to a certain degree in order to apply the data in a machining simulation.

### 2.3.2. Material property modeling

Several phenomenological plasticity models including the early power law model, Johnson-Cook (JC) model [47], Usui model [79,58], mechanical threshold stress (MTS) model [28], Zerilli model [104], etc. have been developed to relate flow stress to plastic strain, strain-rate, and/or temperature. It should be mentioned that the methods to determine flow stress data using machining tests [42,71] and fitting these existing models to the flow stress data are beyond the scope of this research. The adiabatic shear instability model [42] does not contain a strain-rate term. However, machining tests have shown that chip morphology transition occurs beyond a certain strain-rate ( $\sim 10^4$  /s) [12]. Although the phenomenological models are easy to use and may describe the general response of simple material deformations, these models are empirical and semi-empirical and lack mechanisms incorporating isotropic/kinematic hardening, recovery, or complex loading and history effects. Despite sometimes remarkably good fit to measured stress-strain curves within a certain range of strains, strain-rates and temperatures, these models have no predictive power beyond that same range of deformation conditions and material microstructure. Their usage is limited only to the range of deformation conditions for which they were curve-fitted, and the accuracy is often not satisfactory. What is missing in these models is the ability to capture the complex effects which are common in machining.

At present, the traditional JC model is very often used in FEA of metal cutting to incorporate strain, strain-rate, and temperature dependence of the flow stress. The JC model has two parts: the stress function in Equation (2.1) and the strain function in Equation (2.2). It should

be pointed out that the correlation of the equations to experimental data is not satisfactory for many materials. The JC model assumes that the flow stress is a unique function of the total strain, strain-rate, and temperature, and their effects on the flow stress are independent.

$$\sigma = [A + B\varepsilon^n] \left[ 1 + C \ln \frac{\dot{\varepsilon}}{\dot{\varepsilon}_0} \right] (1 - T_h^m) \quad (2.1)$$

$$\varepsilon_f = [d_1 + d_2 \exp(d_3 \frac{\sigma_p}{\sigma_e})] [1 + d_4 \ln(\frac{\dot{\varepsilon}}{\dot{\varepsilon}_0})] (1 + d_5 T_h) \quad (2.2)$$

where the homologous temperature is  $T_h = \frac{T - T_{room}}{T_{melt} - T_{room}}$ ,  $A, B, C, m, n$  are material constants, and

$d_1 \sim d_5$  are material failure parameters. The material failure strain  $\varepsilon_f$  is assumed to be dependent on a nondimensional plastic strain-rate  $\dot{\varepsilon} / \dot{\varepsilon}_0$ , a dimensionless pressure-deviatoric stress ratio  $\sigma_p / \sigma_e$  (where  $\sigma_p$  is the pressure stress and  $\sigma_e$  is the von Mises stress), and  $T_h$ .

The JC model lacks a mechanism to capture history effects of strain path, strain-rate, and temperature in manufacturing processes. In addition, the Bauschinger effect cannot be incorporated. A critical issue for the JC model is that it may not predict the adiabatic phenomenon, i.e., the flow stress dramatically decreases when the plastic strain increases in a transient event such as metal cutting. This point can be clearly seen in Equation (2.1), in which the flow stress goes up when the plastic strain increases at a certain temperature. It basically models an isothermal stress response and works well for static/quasi-static and thermal softening process characterized by the drop of flow stress with the increased temperature regardless of plastic strain. In order to model an adiabatic process, a governing equation of converting

deformation work to thermal energy has to be used. Adiabatic shearing results in the decrease of flow stress when the plastic strain increases.

The JC model has been widely used in FEA simulations of metal cutting to predict residual stresses. One of the earliest saw-tooth chip simulations in orthogonal cutting by Benson [9] was based on the Eulerian algorithm. Saw-tooth chips were also simulated using the Lagrangian algorithm by Movahhedy [62], Guo [31], Guo et al. [37], Behrens [8], and others. Some of these studies used a small negative tool rake angle to make a simulation more practical although a positive rake angle would make the simulation much easier.

The above semi-empirical constitutive models only address homogeneous material properties. The existence of size effect and microstructures make work material inhomogeneous, especially in micromachining. A recent study [38] has shown that an internal state variable based plasticity model developed by Bammann et al. [5-6] is capable of modeling the complex loading history, recovery, adiabatic effects, and microstructures of polycrystalline materials with random microstructures [14,32] as shown in Figures 2.25 and 2.26.

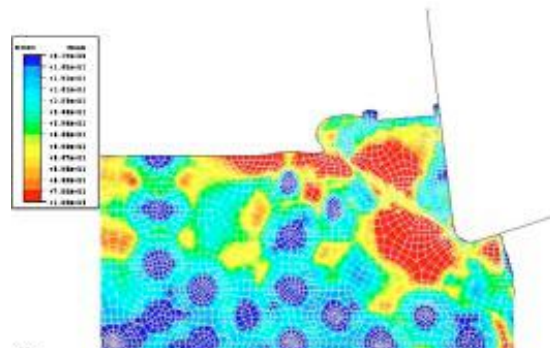


Fig. 2.25 Machining ductile iron with random microstructures of 30-80  $\mu\text{m}$  [14].

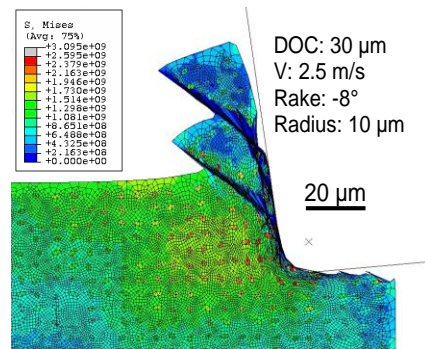


Fig. 2.26 Machining AISI 52100 steel with random microstructures of 2-4  $\mu\text{m}$  [32].

### 2.3.3. Tool-chip and tool-work interface modeling

Friction on the tool-chip and tool-work interfaces is a major input for determining residual stresses, other surface integrity characteristics, and in-process variables. Therefore, an accurate determination of the friction condition is of considerable importance for finite element analysis of metal cutting. The key issue is the variation of apparent friction coefficient at the tool-chip and tool-work interfaces with the surface deformation energy. Some friction models used in finite element simulation of metal cutting are summarized in the literature [30]. The tool-

chip and tool-work interactions have been modeled using different methods: (1) an average friction coefficient only, (2) normal and shear stresses as boundary conditions, (3) an assumed sticking region only with constant shear flow stress, (4) a fixed sliding region with assumed friction coefficient and a sticking region with constant shear flow stress. Some modified friction models has been used in recent simulations of machining hardened and difficult-to-cut steel alloys [35,99,70,103]. Shortcomings associated with these models are summarized as follows.

(1) An average friction coefficient was used arbitrarily or estimated based on the resultant forces without decoupling the sticking and sliding regions. The estimated average coefficient of friction varies greatly under different cutting conditions.

(2) For normal and shear stresses used as boundary conditions, the determination of both distribution and stress magnitude were difficult by experiment methods such as the pin-on-disk, photoelastic, and the split tool techniques, which altered the tool-chip or tool-work friction conditions.

(3) For assumed sticking region only at the tool-chip interface, the omission of sliding region may have appreciable effect on the accuracy of model predictions.

(4) For the friction model with fixed sticking and sliding regions, the sizes of the sticking and sliding regions were assumed. A constant shear flow stress was applied to the fixed sticking region and an assumed friction coefficient to the sliding region. For simulating orthogonal cutting, this model may be easily used as the tool-chip contact is simple. For practical machining processes, it would be difficult to apply this friction model as the tool-chip and tool-work contacts are very complex.

(5) From microtribology point of view, the basic mechanisms and individual contributions of adhesion and ploughing to the apparent friction coefficient have not been well understood.

#### 2.3.4. Simulation methods

Despite significant analytical and semi-analytical modeling efforts over the years, most notably by [40,52-54,7,18,98], the quantitative relationship between cutting conditions and residual stresses is still lacking due to the inherent complexity nature of residual stress formation in machining. Much interest has been directed towards the development of finite element models to predict residual stress distribution since 1980s. Strenkowski and Carroll [84] developed a FEM model of orthogonal cutting demonstrating that the use of chip separation criterion based on the effective plastic strain is essential in predicting residual stresses in the machined layer. Hsu [43] developed a two-dimensional Eulerian FEM model to predict residual stress beneath the machined surface. However, effects of thermal loading and boundary conditions on residual stresses were ignored. Shih [78] proposed a 2D FEM model to predict residual stress based on the geometrical criterion of chip formation. Effects of thermal loading and clamping force were identified as important to predict the residual stress distribution in the machined layer. The effect of tool-wear on the residual stress was ignored. Obikawa et al. [66] investigated effect of discontinuous chip formation on the residual stress distribution without consideration of thermal and boundary effects. No experimental data was provided to verify the model prediction.

The effect of sequential cutting simulation on residual stress was investigated by Sasahara et al. [72] by ignoring the influence of thermal loading and boundary conditions. Guo and Liu [35] simulated the “hook” shaped residual stress profile shown in Figure 2.27 in

orthogonal cutting of annealed 304 stainless steel. Valiorgue et al. [92] used a traditional heat partition-based semi-simulation method to predict the stresses shown in Figure 2.28 in the subsurface in turning of 316L steel. A hybrid predictive model and validation of unique hook-shaped residual stress profiles in hard turning has been recently reported [33] – see Figure 2.29. It has been found that the ploughed depth is the deterministic factor in producing the machining-induced RS profile. The unique hook-shaped RS profile is produced when the ploughing depth reaches a threshold (critical) value. Friction coefficient only affects the magnitude of surface residual stress but not the basic shape of residual stress profiles.

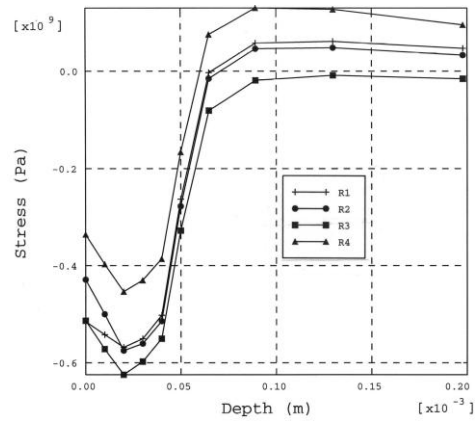


Fig. 2.27 Residual stress evolution by sequential cuts [35] (R1: during cutting; R2: after cooling; R3: after releasing forces; R4: residual stress).

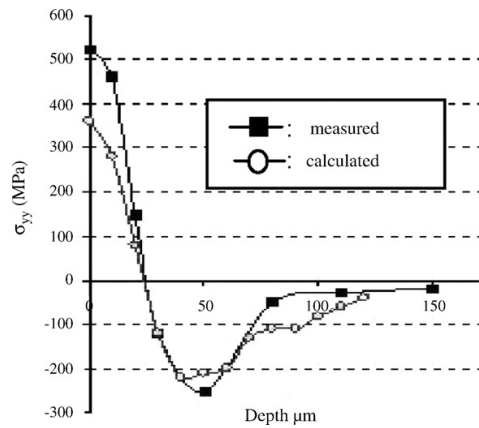


Fig. 2.28 Comparison of predicted and measured residual stress [92].

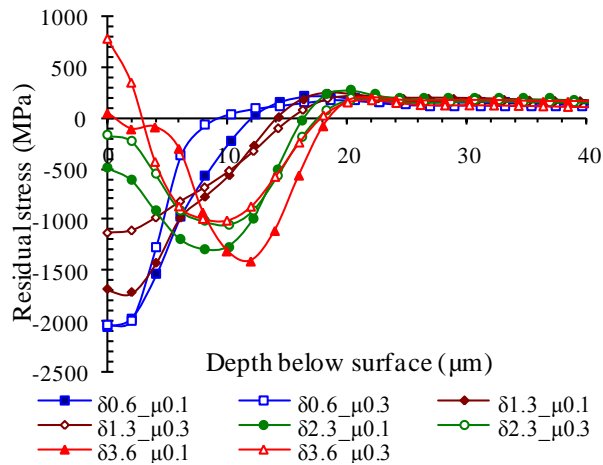


Fig. 2.29 Predicted tangential residual stress profiles in subsurface in AISI 52100 [33].

### 2.3.5. Size effect

It has been known for a very long time that size effect exists in metal cutting process, where the specific energy increases with decrease in deformation size. It is generally believed that this is due to the fact that all metals contain defects, such as grain boundaries, missing and impurity atoms, void, etc., and when the size of the material removed decreases, the probability

of encountering a stress-reducing defect decreases [77]. There are two different aspects of size effects of concern: when the depth of cut is on the same order as the tool edge radius, and where the microstructure of workpiece material contributes a lot to the cutting mechanism. Metal cutting process is greatly influenced by the ratio of the depth of cut to the effective cutting edge radius of the tool. This ratio predominantly defines the material removal mechanism and thus introduces the concept of minimum depth of cut below which no material will be removed, or minimum chip thickness, below which no chip can form. In addition, when the cutting edge dimension is of the same order as the grain size, or where material cannot be treated as isotropic and homogeneous, the cutting mechanism will be substantially different from conventional [20]. A recent comprehensive review paper on size effects documents the historical development of theories and applications involving size effects in machining [94].

The prediction of residual stress by machining hardened steels and difficult-to-cut superalloys is of recent interests. The importance of size effect such as cutting edge radius on the prediction of residual stress has been well recognized [21,37,65,67,101]. However, very few models are capable of explaining or predicting the unique hook-shaped residual stress profiles using sharp tools and the evolution of residual stress profiles with tool-wear in hard turning. An accurate prediction of residual stresses with the incorporation of size effect and other small scale effects is still in scientific infancy.

## 2.4. Future work on multiscale simulation for predicting residual stresses in machining

### 2.4.1. Rationale of multiscale simulation

The machining-induced residual stress and the root causes are typical multiscale physical phenomena manifested in different spatial and temporal scales. On the geometrical side, the unique knowledge can be obtained at different scales are summarized as follows:

*Macro/mesoscale simulation:* Cutting tool geometry such as nose radius ( $\sim 1$  mm), depth of cut (hundred  $\mu\text{m}$  to several mm), feed ( $\sim 100$   $\mu\text{m}/\text{rev}$ ), and workpiece dimensions (mm to m) are macro/mesoscale parameters to generate residual stress. In addition, in-process cutting parameters including chip morphology and cutting forces are generally regarded in macro/mesoscale. If the residual stress distribution depth is on the order of millimeter, it is also in the macro/mesoscale.

*Microscale simulation:* A microscale simulation can help to model the following critical parameters which cannot be incorporated otherwise in other scales.

(1) *Microscale in-process parameters:* The in-process parameters which determine the magnitude, shape, and the affected depth of residual stresses are in microscale, for example temperature penetration of 10-30  $\mu\text{m}$  and strain/strain gradient of 20  $\mu\text{m}$ .

(2) *Microscale residual stress:* The affected depth of a machining induced residual stress on the order of 100  $\mu\text{m}$  at most machining conditions can be simulated as shown in Figure 2.12.

(3) *Size effect:* The magnitudes of process parameters such as cutting edge radius ( $\sim 10$   $\mu\text{m}$ ) and depth-of-cut ( $\sim 10$   $\mu\text{m}$ ), especially in mechanical micromachining [20]. Micromachining with a large aspect ratio of cutting edge radius to depth-of-cut inherits many characteristics of conventional machining. At the same time, micromachining has distinct process physics mainly

due to the comparable sizes of cutting edge radius and depth-of-cut. The downsizing scale of machining results in size effect via plasticity gradient which may fundamentally changes the whole aspect of machining. The size effect results in a ploughing-dominated process rather than the traditional shearing-dominated one. The cutting mechanism transition in micromachining has significant impacts on material properties, cutting mechanics, and the resulting surface integrity of the machined components.

(4) *Microstructure effect*: Due to the comparable sizes of cutting edge radius, depth-of-cut, and microstructures (several  $\mu\text{m}$ ), the microstructures also has a profound influence on a cutting process and surface integrity.

(5) *Microtribology*: The microtribology phenomena between tool/chip and tool/work also need to be addressed at the mciroscale.

*Nanoscale simulation*: Some physical phenomena can only be analyzed in nanoscale. For example chemical transport/diffusion usually occurs in less than 100 nm. The depth of cut is on the order of  $\sim 10\text{nm}$  in a nanocutting process, the cutting process and surface integrity need to be modeled using molecular dynamics (MD) simulations.

On the temporal scale, the related physical phenomena are also multiscale: (1) The dynamic mechanical behavior of a work material in machining characterized by large strain (1 and up), high temperature (up to melting point), and high strain-rate ( $10^6/\text{s}$ ) is very challenge to obtain. However, the mechanical behavior is of great significance for the final residual stress and other surface integrity factors. (2) The associated thermal and microstructural phenomena are multiscale. For instance, the transient cutting temperature ( $\sim 1\text{ ms}$ ) will induce phase transformation on the same time order, but heat conduction/radiation to the workpiece and environment may take minutes or longer.

Since the root-of-causes of residual stress are multiscale, the prediction of residual stress by incorporating the dynamic mechanical and thermal behaviors of work material and practical cutting tool geometry in different scales is a very challenging problem. Although many numerical and analytical studies have been performed on metal cutting, few, if any, have developed and validated multiscale simulation models to predict residual stresses.

#### 2.4.2. Challenges and barriers of multiscale simulation for predicting residual stress

To incorporate different physical processes at different length scales in machining, it is necessary to develop a multiscale simulation model which can predict process parameters at microscale, as well as parameters at macroscale, at certain accuracy. While such a capable model has not been developed for machining at present, recent research efforts in other engineering areas have shown considerable evidence for bridging the different scales. The discussions in the preceding sections lead to the following challenges, barriers, and requirements for research breakthrough. The major issues are elaborate as follows.

- The tyranny of scales: Formidable obstacles remain in linking highly disparate length and time scales and in bringing together the disciplines involved in simulating residual stress. The tyranny of scales cannot be defeated by simply building faster computers, developing efficient algorithms, and using 3D mesh with small geometrical features. Instead, fundamental breakthroughs to model natural events at multiple scales are required.
- Verification and validation: While verification and validation have been subjects of concern for many years, their further development will have a significant impact on the level of confidence one can assign predicted residual stress in light of the knowledge on experimental data. For example, the predicted residual stress by a 2D FEA model is very

challenging to verify due to the fact that a true orthogonal cutting with same simulation conditions is difficult to setup.

- Predictability of residual stresses at operation levels, including 3D model development to take account of varying tool geometry, complex tool-chip and work-tool tribological interactions poses a significant scientific challenge.

## 2.5. References

- [1] Henricksen EK. Residual stresses in machined surfaces. *Trans. ASME* 1951; 73: 69-76.
- [2] Colwell LV, Sinnot MJ, Tobin JC. The determination of residual stresses in hardened, ground steel. *Trans. ASME* 1955; 77: 1099-1105.
- [3] Field M, Kahles JF. The surface integrity of machined and ground high strength steels. *DMIC Report* 1964; 210: 54-77.
- [4] Field M, Kahles JF. Review of surface integrity of machined components. *Annals of the CIRP* 1971; 20 (2): 153-162.
- [5] Field M, Koster WP, Kohls JB, Snider RE, Maranchik J. Machining of high strength steels with emphasis on surface integrity. Tech. Report AFMDC 70-1, Metcut Research Associates, Inc. 1970.
- [6] Koster WP, Field M, Fritz LJ, Gatto LR, Kahles JF. Surface integrity of machined structural components. Tech. Report AFML-TR-70-11, Metcut Research Associates, Inc. 1970.
- [7] Liu CR, Barash MM. The mechanical state of the sublayer of a surface generated by chip-removal process, part1: cutting with a sharp tool. *Trans. ASME, J. Eng. Ind.* 1976; 98 (4): 1192–1201.
- [8] Liu CR, Barash MM. The mechanical state of the sublayer of a surface generated by chip-removal process, part2: cutting with a tool with flank wear. *Trans. ASME, J. Eng. Ind.* 1976; 98 (4): 1202–1208.
- [9] Liu CR, Barash MM. Variables governing patterns of mechanical residual stress in a machined surface. *Trans. ASME, J. Eng. Ind.* 1982; 104 (3): 257-264.

- [10] Brinksmeier E, Cammett JT, König W, Leskovar P, Peters J, Tönshoff HK. Residual stresses-measurement and causes in machining processes. *Annals of the CIRP* 1982; 31 (2): 491-510.
- [11] Brinksmeier E, Schneider E, Theiner WA, Tönshoff HK. Nondestructive testing for evaluating surface integrity. *Annals of the CIRP* 1984; 33 (2): 489-509.
- [12] Jeelani S, Bailey JA. Residual stress distribution in machining annealed 18 percent nickel maraging steel. *ASME Journal of Engineering Materials and Technology* 1986; 108: 93-98.
- [13] Jeelani S, Biswas S, Natarajan R. Effect of cutting speed and tool rake angle on residual stress distribution in machining 2024-T351 aluminium alloy: a study of cumulative fatigue damage in AISI 4130 steel. *J. of Material Science* 1986; 21: 2705-2710.
- [14] Schwach DW, Guo YB. A fundamental study on the impact of surface integrity by hard turning on rolling contact fatigue. *Int. J. Fatigue* 2006; 28: 1838-1844.
- [15] El-Khabeery MM, Fattouh M. Residual stress distribution caused by milling. *International Journal of Machine Tools & Manufacture* 1989; 29: 391-401.
- [16] Warren AW, Guo YB. The impact of surface integrity by hard turning vs. grinding on rolling contact fatigue: comparison of fatigue life and acoustic emission signals. *Fatigue & Fracture of Eng. Mater. Structures* 2007; 30: 698-711.
- [17] Tönshoff HK. Eigenspannungen und plastische verformungen im werkstück durch spanende bearbeitung. Dr.-Ing. Diss. TH Hannover 1965.
- [18] Tönshoff HK. Randzonenbeeinflussung durch spanen und abtragen – ein beitrag zur anpassung der analysenmethoden. *Annals of the CIRP* 1974; 23 (1): 187-188.
- [19] Lu J. Handbook of measurement of residual stresses. The Fairmont Press, Inc., Lilburn, GA 1996.
- [20] M'Saoubi R, Outeiro JC, Chandrasekaran H, Dillon OW, Jawahir IS. A review of surface integrity in machining and its impact on functional performance and life of machined products. *Int. J. Sustainable Manufacturing* 2008; Vol. 1, Nos. 1 (2): 203-236.
- [21] Klocke F, Brinksmeier E, Weinert K. Capability profiles of hard cutting and grinding processes. *Annals of the CIRP* 2005; 54 (2): 557-580.
- [22] Lucca DA, Brinksmeier E, Goch G. Progress in assessing surface and subsurface integrity. *Annals of the CIRP* 1998; 47 (2): 669-693.
- [23] Tönshoff HK, Arendt C, Amor RB. Cutting of hardened steel. *Annals of the CIRP* 2000; 49 (2): 547-566.

- [24] Matsumoto Y, Barash MM, Liu CR. Effect of hardness on the surface integrity of AISI 4340 steel. *Journal of Engineering for Industry* 1986; 108: 169-175.
- [25] Matsumoto Y, Hashimoto F, Lahoti G. Surface integrity generated by precision hard turning. *Annals of the CIRP* 1999; 48 (1): 59-62.
- [26] Dahlman P, Gunnberg F, Jacobson M. The influence of rake angle, cutting feed and cutting depth on residual stresses in hard turning. *Journal of Materials Processing Technology* 2004; 147: 181-184.
- [27] Goldstein M. Optimierung der fertigungsfolge 'kaltfließpressen-spanen' durch hartdrehen als feinarbeitungsverfahren für einsetzgehärtete preßbauteile. Doctoral thesis, RWTH Aachen 1991.
- [28] Tönshoff HK, Wobker HG, Brandt D. Hard turning-influences on the workpiece properties. *Transactions of NAMRI/SME* 1995; 23: 215-220.
- [29] König W, Klinger M, Link R. Machining hard materials with geometrically defined cutting edges-field of applications and limitations. *Annals of the CIRP* 1990; 39 (1): 61-64.
- [30] Warren AW, Guo YB. Characteristics of residual stress profiles in hard turned versus ground surfaces with and without a white layer. *ASME J. Manufacturing Sci. Eng.* 2009; 131 (041004): 1-10.
- [31] Zhang S, Guo YB. An experimental and analytical analysis on chip morphology, phase transformation, oxidation, and their relationships in finish hard milling. *International Journal of Machine Tools & Manufacture* 2009; 49: 805-813.
- [32] Axinte DA, Dewes RC. Surface integrity of hot work tool steel after high speed milling-experimental data and empirical models. *Journal of Materials Processing Technology* 2002; 127: 325-335.
- [33] Marques MJ, Outeiro JC, Dias AM, M Saoubi R, Chandrasekaran H. Surface integrity of H13 ESR mould steel milled by carbide and CBN tools. *Materials Science Forum* 2006; p. 514-516, 564-568.
- [34] Chandrasekaran H, M'Saoubi R, Högman B, Nordh LG, Coulon B, Lebrun JL, Viale D, Gitton S, Montero MC, Marques MJ, Outeiro JC, Dias AM. Development of machinability enhanced tool steels for improved product economy in hard milling. *Technical Steel Research-Report EUR 21726, EC, Brussels* 2005.
- [35] Zhang S, Guo YB. Taguchi method based process space for optimal surface topography by finish hard milling. *ASME J. Manufacturing Sci. Eng.* 2009; 131 (051003): 1-9.
- [36] Elbestawi MA, Chen L, Becze CE, El-Wardany TI. High-speed milling of dies and molds

- in their hardened state. *Annals of the CIRP* 1997; 46 (1): 57-62.
- [37] Ezugwu EO. Key improvements in the machining of difficult-to-cut aerospace superalloys. *Int. J. Machine Tools & Manufacture* 2005; 45: 1353-1367.
- [38] Zoya ZA, Krishnamurthy R. The performance of CBN tools in the machining of titanium alloys. *J. Mater. Proc. Tech.* 2000; 100: 80-86.
- [39] Copper D. Machining capacity, expertise must grow. *SME/Aerospace & Defense Manufacturing, Manufact. Eng.* 2006. p. 63-65.
- [40] Sun J, Guo YB. A new multi-view approach to characterize 3D chip morphology and properties in end milling titanium alloy Ti-6Al-4V. *Int. J. Machine Tools and Manufacture* 2008; 48: 1486-1494.
- [41] Kahles JF, Field M, Eylon D, Froes FH. Machining of titanium alloys. *Journal of Metals* 1985; 37: 27-35.
- [42] Hong H, Riga AT, Cahoon JM. Machinability of steels and titanium alloys under lubrication. *Wear* 1993; 162: 34-39.
- [43] Su Y, He N, Li L, Li XL. An experimental investigation of effects of cooling/lubrication conditions on tool wear in high-speed end milling of Ti-6Al-4V. *Wear* 2006; 261: 760-766.
- [44] Zlatin N, Field M. Procedures and precautions in machining titanium alloys. *Titanium Sci. Tech.* 1973; 1: 489-504.
- [45] Narutaki N, Murakoshi A, Motonishi S. Study on machining of titanium alloys. *Annals of the CIRP* 1983; 32 (1): 65-69.
- [46] Hughes JI, Sharman ARC, Ridgway K. The effect of cutting tool material and edge geometry on tool life and workpiece surface integrity. *Proc. IMechE, Part B: Journal of Engineering Manufacture* 2005; 220: 93-107.
- [47] Yang XP, Liu CR, Grandt AF. An experimental study on fatigue life variance, residual stress variance, and their correlation of face-turned and ground Ti-6Al-4V samples. *Journal of Manufacturing Science and Engineering* 2002; 124: 809-819.
- [48] Sun J, Guo YB. A comprehensive experimental study on surface integrity by end milling Ti-6Al-4V. *Journal of Materials Processing Technology* 2009; 209: 4036-4042.
- [49] Sharman ARC, Hughes JI, Ridgway K. An analysis of the residual stresses generated in Inconel 718TM when turning. *Journal of Materials Processing Technology* 2006; 173: 359-367.
- [50] Arunachalam RM, Mannan MA, Spowage AC. Residual stress and surface roughness

- when facing age hardened Inconel 718 with CBN and ceramic cutting tools. *International Journal of Machine Tools & Manufacturing* 2004; 44: 879-887.
- [51] Outeiro JC, Pina JC, M'Saoubi R, Pusavec F, Jawahir IS. Analysis of residual stresses induced by dry turning of difficult-to-machine materials. *Annals of the CIRP* 2008; 57: 77-80.
- [52] Sharman ARC, Hughes JI, Ridgway K. Surface integrity and tool life when turning Inconel 718 using ultra-high pressure and flood coolant systems. *Proc. IMechE, part B: J. Engineering Manufacture* 2008; 222: 653-664.
- [53] Arunachalam RM, Mannan MA, Spowage AC. Surface integrity when machining age hardened Inconel 718 with coated carbide cutting tools. *International Journal of Machine Tools & Manufacture* 2004; 44: 1481-1491.
- [54] Aspinwall DK, Dewes RC, Ng E.-G, Sage C, Soo S.L. The influence of cutter orientation and workpiece angle on machinability when high-speed milling Inconel 718 under finishing conditions. *International Journal of Machine Tools & Manufacture* 2007; 47: 1839-1846.
- [55] van Luttervelt CA, Childs THC, Jawahir IS, Klocke F, Venuvinod PK. Present situation and future trends in modeling of machining operations--progress report of the CIRP working group 'modeling of machining operations. *Annals of the CIRP* 1998; 47 (2): 587-626.
- [56] Oxley PLB. *The mechanics of machining*. Ellis Horwood Limited, Chichester, England, UK 1989.
- [57] Stevenson R. Study on the correlation of workpiece mechanical properties from compression and cutting Tests. *J. Mach. Sci. Tech.* 1997; 1(1): 67-79.
- [58] Shatla M, Altan T. Determination of flow stress for machining and practical applications of FEM and analytical modeling. *Proc. 2000 NSF Design & Manufacturing Res. Conf., Vancouver, British Columbia, Canada* 2000.
- [59] Spaans C. *The fundamentals of three-dimensional chip curl, chip breaking and chip control*. Ph.D. Dissertation, Delft University of Technology, Delft, South Holland, Netherlands 1971.
- [60] Stevenson MG, Oxley PLB. Torsional hopkinson bar tests to measure stress-strain properties relevant to machining and high speed forming. *North America Metalwork Res. Conf., 3rd Proc.* 1975; p. 291-304.
- [61] Shirakashi T, Maekawa K, Usui E. Flow stress of low carbon steel at high temperature and strain rate, part 1: property of incremental strain method in impact compression test with rapid heating and cooling systems. *Bull. Japan Soc. Prec. Eng.* 1983; 17: 161-166.

- [62] Yoshino M, Shirakashi T. Flow-stress equation including effects of strain rate and temperature history. *Int. J. Mech. Sci.* 1997; 39 (12): 1345-1362.
- [63] Stevenson R, Stephenson DA. The mechanical behavior of zinc during metal cutting. *J. Eng. Mat. Tech.* 1995; 117: 172-178.
- [64] Guo YB. An integral method to determine the mechanical behavior of materials in metal cutting. *J. Mater. Proc. Tech.* 2003; 142 (1): 72-81.
- [65] Guo YB, Liu CR. Mechanical properties of hardened AISI 52100 steel in hard machining. *ASME J. Manuf. Sci. Eng.* 2002; 124: 1-9.
- [66] Johnson GR, Cook WH. Fracture characteristics of three metals subjected to various strains, strain rates, temperatures and pressures. *Eng. Frac. Mech.* 1985; 21: 31-48.
- [67] Maekawa K, Shirakashi T, Usui E. Flow stress of low carbon steel at high temperature and strain rate, part 2: flow stress under variable temperature and variable strain rate. *Bull. Japan Soc. Prec. Eng.* 1983; 17: 167-172.
- [68] Follansbee PS, Kocks UF. A constitutive description of the deformation of copper based on the use of the mechanical threshold stress as an internal state variable. *Acta Metall.* 1988; 36: 81-93.
- [69] Zerilli FJ, Armstrong RW. Dislocation-mechanics-based constitutive relations for material dynamics calculations. *J. App. Phy.* 1987; 61: 1816-1825.
- [70] Hou ZB, Komanduri R. Modeling of thermomechanical shear instability in machining. *Int. J. Mech. Sci.* 1997; 39: 1273-1314.
- [71] Sartkulvanich P, Koppka F, Altan T. Determination of flow stress for metal cutting simulation – a progress report. *J. Mater. Proc. Tech.* 2004; 146: 61-71.
- [72] Campbell JD. Dynamic plasticity: macroscopic and microscopic aspects. *Mater. Sci. Eng.* 1973; 12: 3-21.
- [73] Benson DJ. A mixture theory for contact in multi-material Eulerian formulations. *Comput. Methods Appl. Mech. Engr.* 1997; 140: 59-86.
- [74] Movahhedy MR, Altintas Y, Gadala MS. Numerical analysis of metal cutting with chamfered and blunt tools. *J. Manuf. Sci. Eng.* 2002; 124: 178-188.
- [75] Guo YB, Wen Q. A hybrid approach to investigate chip morphology transition from saw-tooth to discontinuous chips with the effects of cutting edge geometry. *Trans. of NAMRI/SME* 2005; XXXIII: 469-476.
- [76] Behrens A, Kalisch K, Wulfsberg JP. Possibilities and problems of finite element

- simulation of high speed cutting mechanics. ASME/IMECE, MED, Anaheim, CA 2004.
- [77] Guo YB, Wen Q, Horstemeyer MF. An internal state variable plasticity based approach to determine dynamic loading history effects on material property in manufacturing processes. *Int. J. Mech. Sci.* 2005; 47: 1423–1441.
- [78] Bammann D.J. Modeling temperature and strain rate dependent large deformation of metals. *Appl. Mech. Rev.* 1990; 43: 312-319.
- [79] Bammann DJ, Chiesa ML, Johnson GC. Modeling large deformation and failure in manufacturing processes. In: Tatsumi, T., Wanatabe, E., Kambe, T. (eds.) *Theor. App. Mech.* 1996. p. 359-376.
- [80] Chuzhoy L, DeVor RE, Kapoor SG, Beaudoin AJ, Bammann DJ. Machining simulation of ductile iron and its constituents, part 2: numerical simulation and experimental validation of machining. *ASME J. Manuf. Sci. Eng.* 2003; 125: 192-201.
- [81] Guo YB, Anurag S. Finite element modeling and simulation of micromachining random multiphase materials. *Trans. NAMRI/SME* 2008; 36: 373-380.
- [82] Guo YB. Finite element analysis of superfinish hard turning. Ph.D. Dissertation, Purdue University, West Lafayette 2000.
- [83] Guo YB, Liu CR. FEM analysis of mechanical state on sequentially machined surfaces. *Machining Science and Technology* 2002; 6: 21-41.
- [84] Yang XP, Liu CR. A new stress-based model of friction behavior in machining and its significant impact on residual stresses computed by finite element method. *International Journal of Mechanical Sciences* 2002; 44: 703-723.
- [85] Özel T. The influence of friction models on finite element simulations of machining. *Int. J. Mach. Tools & Manuf.* 2006; 46: 518–530.
- [86] Zemzemi F, Rech J, Ben Salem W, Dogui A, Kapsa P. Identification of a friction model at tool/chip/workpiece interfaces in dry machining of AISI4142 treated steels. *Jour. Mat. Proc. Tech.* 2008; 209: 3978-3990.
- [87] Barash MM, Schoech WJ. A semi-analytical model of the residual stress zone in orthogonal machining. *Proc. 11th Int. MTDR Conf.*, Pergamon Press, London 1970. p. 603.
- [88] Devarajan N, Asundi MK, Somasundaram S. Experimental method for predicting residual stresses due to turning in stainless steel. *Experimental Techniques* 1984. p. 22-26.
- [89] Wu DW, Matsumoto Y. The effect of hardness on residual stresses in orthogonal

- machining of AISI 4340 steel. *Trans. ASME, J. Eng. Ind.* 1990; 112 (3): 245-252.
- [90] Strenkowski JS, Carroll JT. A finite element model of orthogonal metal cutting. *Trans. ASME, J. Eng. Ind.* 1985; 107: 349-354.
- [91] Hsu HC. An elasto-viscoplastic finite element model of orthogonal metal cutting for residual stress prediction. Ph.D. Dissertation, North Carolina State University, Raleigh, USA 1992.
- [92] Shih AJ. Finite element simulation of orthogonal metal cutting. *Transactions of the ASME* 1995; 117: 84-93.
- [93] Obikawa T, Sasahara H, Shirakashi T. Application of computational machining method to discontinuous chip formation. *Journal of Manufacturing Science and Engineering* 1997; 119: 667-674.
- [94] Sasahara H, Obikawa T, Shirakashi T. Finite element modeling of residual stress control on machined surface. *Trans. NAMRI/SME* 1997; XXV: 231-218.
- [95] Valiorgue F, Rech J, Hamdi H, Gilles P, Bergheau JM. A new approach for the modeling of residual stresses induced by turning of 316L. *Journal of Materials Processing Technology* 2007; 191: 270-273.
- [96] Guo YB, Anurag S, Jawahir IS. A novel hybrid predictive model and validation of unique hook-shaped residual stress profiles in hard turning. *Annals of the CIRP* 2009; 58 (1): 81-84.
- [97] Shaw MC. The size effect in metal cutting. *Sadhana-Academy Proceedings in Engineering Sciences* 2003; vol.28, part 5: 875-896.
- [98] Dornfeld D, Min S, Takeuchi Y. Recent advances in mechanical micromachining. *Annals of the CIRP* 2006; 55 (2): 1-24.
- [99] Vollertsen F, Biermann D, Hansen HN, Jawahir IS, Kuzman K. Size effects in manufacturing of metallic components. *Annals of the CIRP* 2009; 58 (2): 566-587.
- [100] Ee KC, Dillon OW, Jawahir IS. Finite element modeling of residual stresses in machining induced by cutting tool with a finite edge radius. *Int. J. Mech. Sci.* 2005; 47: 1611-1628.
- [101] Nasr Mohamed NA, Ng EG, Elbestawi MA. Modeling the effects of tool-edge radius on residual stresses when orthogonal cutting AISI 316L. *International Journal of Machine Tools & Manufacture* 2007; 47: 401-411.
- [102] Outeiro JC, Dias AM, Jawahir IS. On the effects of residual stresses induced by coated and uncoated cutting tools with finite edge radii in turning operations. *Annals of the CIRP* 2006; 55 (1): 111-116.

- [103] Yen YC, Jain A, Altan T. A finite element analysis of orthogonal machining using different tool edge geometries. *J. Mater. Proc. Tech.* 2004; 146: 72-81.

## CHAPTER 3

### A NOVEL ONLINE OPTICAL SYSTEM FOR INSPECTING TOOL WEAR CONDITION IN MILLING HARDENED STEELS AND NICKEL-BASED SUPERALLOYS

#### Abstract

Tool wear adversely affects surface integrity due to higher cutting forces and temperatures. In this paper, a novel online optical tool inspection system has been developed to integrate with a CNC machining center to monitor tool wear conditions in milling. The evolutions of tool flank wear of PVD coated inserts in end milling of AISI H13 tool steel and Inconel 718 superalloy were inspected to demonstrate the function of the optical measurement system. The tool wear evolution versus cutting time were obtained and examined. The characteristic images of fast tool wear in milling Inconel 718 were captured using scanning electron microscope (SEM) and compared with the optical images to estimate flank wear. Three basic modes of tool wear: flank wear, nose wear, and crater wear were compared and analyzed. A two-parameter method has been developed to evaluate both flank wear and nose wear with respect to cutting time in milling Inconel 718. The advantages of the on-line optical tool inspection system were discussed.

### 3.1. Introduction

#### 3.1.1. Tool wear and its impact on surface integrity, performance

Tool wear can be described as gradual failure of cutting tools during manufacturing process. It is a complex but general phenomenon occurring in metal cutting industry. Tool wear is considered to be a critical factor that determines the economy of the machining process since it is closely related to the cutting tools' life and thus the overall cost of production. Kannatey-Asibu and Dornfeld [1] referred the term tool wear to degradation of the cutting tool with three basic modes of failure: (a) gradual wear of cutting surfaces of the tool; (b) fracture of the cutting edge due to excessive cutting forces; (c) high temperatures at the cutting tip which can reduce mechanical properties of the tool.

A sharp tool (without or with small flank wear) will generally produce compressive residual stress and no microstructure changes on the machined surface are induced. While, Guo and Ammala [2] found that a worn tool will increase cutting temperature which results in a thin white layer and undesirable tensile residual stress on the machined surface. Worn tools harmfully affect surface integrity and performance of the workpiece to be machined. Increased cutting forces and temperature, more tensile residual stress (RS), increased surface roughness on the machined parts will be generated when machining with worn tools. Consequently, dimensional accuracy and repeatability of workpiece is reduced and more energy is expected to be consumed during machining process. The surface integrity and performance of the parts machined by worn tools would be deteriorated to unexpected state compared with parts machined by fresh tools. However, few researchers have constructed a necessary bridge between tool wear and surface integrity of machined components. It is the primary concern for manufacturers to produce as

many qualified parts as they could with minimum machining costs. The relationship between tool life and product quality can provide important guide for industry production.

Machined components may be put under various applications. However, no matter what conditions the machined components will be experiencing, their performance is always the first concern from customers' perspective. The performance of the components largely depends on the machining process which generally affects the very thin layer beneath the machined surface and the surface integrity of that thin layer can directly determine the performance. Therefore, the connection among cutting tool wear, surface integrity and performance of machined parts should be well recognized in order to maintain the desired quality of products in mass production process. In this context, experiments are necessary to be done trying to find the linkage of the three factors.

#### 3.1.1.1. Tool steel

AISI H13 is perhaps the most versatile hot work tool steel available for many years and its application covers pressure die casting, extrusion, hot forging and extrusion mandrels. Guo et al. [3] concluded that hard machining hardened steel can be cheaper, faster, more flexible, and more environmentally friendly compared to grinding and other finishing process. Elbestawi et al. [4] investigated the white layers formed in high-speed milling of hardened AISI H13 using PCBN ball-nose end mills, and found that the white layer was dependant on edge preparation and tool wear. Axinte and Dewes [5] demonstrated the influence of cutting speed and feed rate on surface roughness using a full factorial experimental design with two levels of each factor in milling hardened H13 steel (HRc 47-49) by TiAlN coated carbide tools. However, no white layers or other microstructural alterations were observed even with worn tools under the higher levels of cutting speed and feed rate. Ghani et al. [6] has shown that the use of high cutting speed,

low feed rate and low depth-of-cut leads to a good surface finish in semi-finish and finish machining hardened AISI H13 steel with TiN-coated carbide insert tools. Li et al. [7] studied surface integrity produced by cutting tools with different initial flank wear values when end milling AISI H13, including surface finish, subsurface microstructure and microhardness. Guo et al. [3] conducted a review of experimental study on surface integrity characterization after machining hardened steel.

Koster and Field [8] suggested that the main mechanical property affected by machining is high cycle fatigue strength and the actual endurance limit depends on the particular process used and the severity of operation. Historically, performance of the parts was often attributed to surface roughness parameter  $R_a$  (arithmetic average). Koster [9] summarized experimental work on fatigue strength of different workpiece materials (iron, nickel and titanium based alloys) subject to a range of machining processes: finish grinding, milling and turning. He found that the endurance limit of steel was dependent on surface roughness while other two were not. Surface residual stress has also been suggested to be an important indicator of fatigue performance. Guo and Yen [10] concluded that the slope of a compressive residual stress profile is important for rolling contact fatigue damage. Brinksmeier et al. [11] suggested that machining induced residual stress can be recognized as one of the main factors which will significantly affect fatigue life. Matsumoto et al. [12] studied the effect of machining processes on the fatigue strength of AISI 4340 and they found that the average fatigue life of cut samples was higher than those ground samples. Taylor and Clancy [13] concluded that surface roughness had a distinct effect on the fatigue life.

### 3.1.1.2. Nickel-based superalloy

The Inconel family of alloys was first developed in 1940s to support the development of jet engines for aerospace applications. They are well suited for service in extreme conditions due to their high oxidation and corrosion resistance. In particular, they are usually employed in the hot sections of gas turbines, jet motors, rocket engines and spacecraft since they are more creep-resistant than steels after precipitation hardening and thus retain strength over a wide temperature range. Inconel 718 is one of the most commonly used nickel-based alloys in aerospace industry. It is known to be among the most difficult-to-cut materials due to its high strength even at high temperatures, low thermal conductivity, and especially rapid work hardening. Sharman et al. [14] reported hook-shaped residual stress profiles in turning Inconel 718, with tensile stress at the surface for  $TiCN/Al_2O_3/TiN$  coated and uncoated fresh  $WC$  tools. Both sharp and worn uncoated  $WC$  tools produce less tensile residual stresses than those by the coated tools. It is very interesting to note while the worn uncoated  $WC$  tools produces more compressive residual stress at the surface than those by the new uncoated  $WC$  tools. Kim et al. [15] applied three different cutting environments: dry, flood coolant and compressed chilly-air coolant to investigate the tool flank wear evolution when high-speed milling Inconel 718. Alauddin et al. [16] used uncoated tungsten carbide inserts in end milling Inconel 718 under dry conditions to test tool life on the basis of flank wear. Sharman et al. [17] outlined a 3 factor, full factorial cutting experiment at two levels to study tool life when high speed end milling Inconel 718 with ball nose cutter. From ANOVA results for tool life, they concluded that tool coating was the main factor affecting tool life, followed by cutting speed and workpiece angle.

Jeelani and Collins [18] investigated the effect of electric discharge machining on surface integrity (including surface roughness and microhardness) and tension-compression fatigue life

of Inconel 718 alloy at room temperature. The experimental results indicated that microhardness and roughness of machined surfaces slightly increased compared to parent specimens but remained unchanged with variations in cutting speed. The fatigue lives of the machined specimens slightly decreased but were not sensitive to changes of cutting speed. Huang and Ren [19] presented a study on formation of surface integrity (including surface roughness, residual stresses) produced by turning and grinding nickel-based superalloy GH33A. They also compared the effects of surface integrity on high-cycle and low-cycle fatigue lives at both room temperature and 550 °C. The results from experimental work showed that under high-cycle stress-controlling fatigue condition, the main factors affecting fatigue life are surface roughness and residual stresses, while under low-cycle strain-controlling fatigue condition, fatigue lives are mainly affected by surface roughness.

### 3.1.2. Tool condition monitoring methods

Majority of the manufacturing activities in industry are dealing with the production of lot sizes with broad range. Since the contact between tool and workpiece will certainly initiate tool wear when sufficient cutting time is given, tool wear is unavoidable and is an accumulating process. When a tool has been used for cutting various parts, a decision must be made whether or not the worn tool should be replaced before next cutting in order to maintain dimensional accuracy and repeatability. The safest way for getting machined components of desired quality in the subsequent cutting process is to replace the old tool and put a new one. However, this will obviously increase the manufacturing cost and reduce the production efficiency since more tools will be used and extra time for replacement should also be considered. In order to achieve maximum production efficiency, desired surface integrity and thus product performance with

minimum manufacturing cost, accurate measurements for tool wear is necessary to avoid premature of tools.

Various methods for tool wear measurement have been developed and they can be classified into direct (optical, radioactive, and electrical resistance, etc.) and indirect (AE, spindle motor current, cutting force, vibration, etc.) sensing methods. Li, Wong and Nee [20] presented a vision-based approach for tool wear identification in finish turning using an adaptive resonance theory (ART2) neural network embedded with fuzzy classifiers. This approach is based upon the fact that the optical scattering image of a turned surface is related to the tool wear and thus the state of tool wear can be determined from captured images obtained by laser scattering from the machined surfaces. Li, Djordjević and Venuvinod [21] also used neuro-fuzzy technique to monitor the tool wear. They performed machining tests on a CNC lathe over a range of turning conditions and the change of the estimated feed cutting force with time was used to monitor the tool wear. Many researchers have also contributed to the development of monitoring the cutting processes indirectly. Acoustic emission (AE) is one of the most effective ways of indirectly sensing tool wear. Iwata and Moriwaki [22] started using an AE signal to monitor tool wear in cutting process. They found that the total AE count was closely related to the tool wear, which established the basis and proved the feasibility of AE-based sensing methodologies for tool wear monitoring. Guo and Ammala [2] investigated the sensitivity of a broad AE signal parameters including RMS, frequency and count rate to white layer, surface finish and tool wear by a real-time acoustic emission monitoring system. They showed that RMS values and the frequency decreased when the tool flank wear develops until white layer appears. However, AE count rate has been proved to be not sensitive to the thickness of white layer. They provided fundamental information to develop on-line AE monitoring system for surface integrity in hard machining.

Kim et al. [23] observed the purely progressive tool wear in turning and they found that the relationship between the AE signal and tool wear is nonlinear. The AE signal could be widely used for tool wear monitoring if an effective mathematical model to map the relationship between the two can be found. Vajpayee and Sampath [24] concluded that AE count rate is a reliable parameter for predicting the flank wear of a cutting tool.

The existing indirect tool wears measurement techniques are based on cutting force, vibration or acoustic emission and they may not be sensitive enough to detect tool wear. If smaller depth of cut or lower feed rate was used, the magnitude of the signal is relatively not as significant against the background noise. Li, Wong and Nee [20] noticed that for direct techniques, the machined surface roughness may not correlate very well with the intensity of its optical scattering pattern or the measurement of the workpiece dimension and its surface roughness by which to monitor tool wear is not suitable for on-line utilization. Optical method may provide nondestructive means for evaluating cutting tool flank wear by capturing optical images of the tool flank face. Pavel et al. [25] investigated typical tool crater wear pattern and tool flank wear pattern by using a stereo microscope and a scanning electron microscope with X-ray Energy Dispersive Spectrometer. While, no quantitative tool wear values were measured or reported.

### 3.1.3. Research objectives

In the present study, a novel on-line optical tool monitoring system has been proposed and utilized to monitor tool conditions (flank wear, build-up edge, adhesion etc.) in end milling tool steel AISI H13 and superalloy Inconel 718. The monitoring system can be integrated with CNC machine tool during milling experiments. In end milling AISI H13 and Inconel 718,

monitoring tool flank wear evolution may provide useful guide on when to replace the current worn tool with fresh one to avoid inconsistent surface integrity and performance of machined components. SEM (scanning electron microscope) was also applied at certain intervals during end milling Inconel 718 in order to obtain overview of the cutting edge to fully analyze and characterize the typical fast tool deterioration process. Based on the optical monitoring system and SEM, the tool wear development in end milling Inconel 718 can be comprehensively observed and quantitatively studied.

### 3.2. Experimental procedure

Both end milling of AISI H13 and Inconel 718 experiments were carried out on a 3-axis CINCINNATI Arrow 500 CNC vertical machining center. Tool wear and flank build-up formation of the above three materials were monitored respectively by on-line optical tool monitoring system integrated with CNC machining center. No coolant was applied in end milling AISI H13. General purpose synthetic coolant was used throughout end milling Inconel 718 to slow down the tool wear rate and better capture the characteristics of tool deterioration process.

#### 3.2.1. On-line optical tool monitoring system

The setup of on-line optical tool inspection system for milling is shown in Figure 3.1. The system is consisted of fiber optic illuminator, optical camera, fixture, and optical imaging system. An illuminator provided light source for the optical monitoring system and fiber optics transmitted the light signals to the microscope camera. Optical camera takes image of object online and sends it to the optical imaging system which records and processes the images.

Fixture can provide support for the optical camera and fix the position of the whole capturing system. The milling tool can be monitored by shifting flank face above the optical lens in the system and then images of the tool can be captured. No disassembly of the cutting tool is needed when examining on flank face and in-situ investigation of tool flank wear is achieved which improves measurement efficiency. The flank wear values can also be determined by measuring the wear length on the flank face.

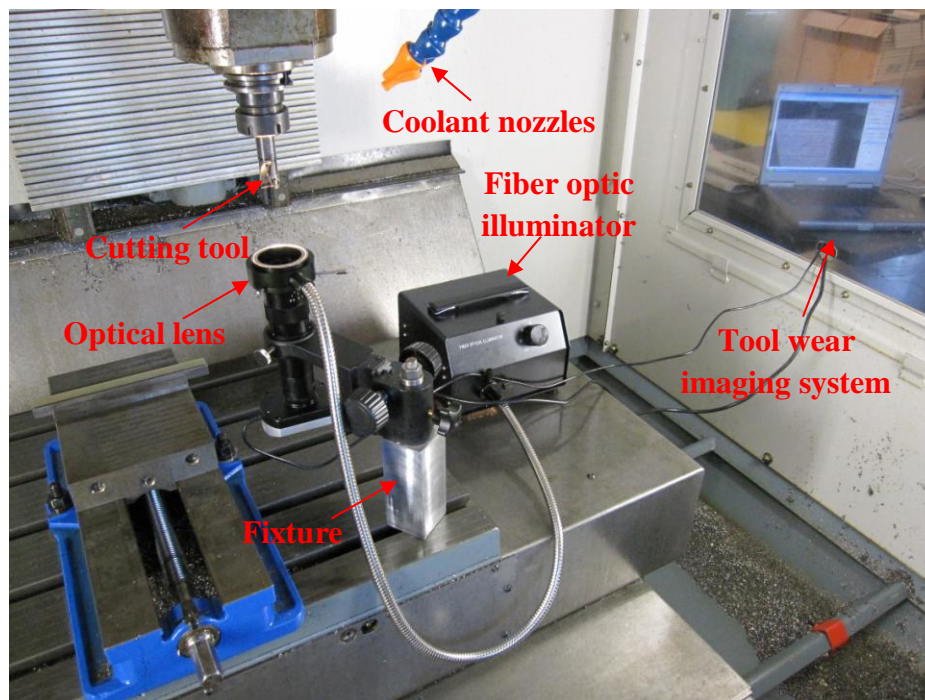


Fig. 3.1 On-line optical tool wear inspection system in milling.

### 3.2.2. Work material and cutting tool

#### 3.2.2.1. AISI H13 and PVD insert

The AISI H13 workpiece samples used in end milling experiment were 203.2 mm × 21 mm × 12.7 mm rectangular blocks. They were thoroughly hardened and tempered to  $50 \pm 1$  HRC.

The cutting tool used in the machining tests was a 20 mm diameter end milling cutter with two PVD (Ti, Al) N-TiN-coated carbide inserts. The tool holder and the PVD-coated inserts were made by SECO Tool Company.

### 3.2.2.2. Inconel 718 and PVD insert

Superalloy Inconel 718 was also prepared for end milling experiments. Table 3.1 shows the nominal chemical composition of the precipitation hardened Inconel 718. The dimension of the workpiece block was 200 mm × 22 mm × 13 mm with a bulk hardness of 45 ± 1 HRC. The cutting tool used in the machining tests was a 20 mm diameter end milling cutter with one PVD (Ti, Al) N/TiN-coated carbide insert. The tool holder and the insert were also made by SECO Tool Company.

Table 3.1 Chemical composition of Inconel 718 (wt %).

Element	wt %
Ni	51.49
Cr	18.31
Fe	Balance
Cb	5.03
Mo	2.93
Ti	1.04
Al	0.54
Co	0.20
Si	0.07
Mn	0.070
C	0.043
P	0.007
Cu	0.039
B	0.002
Ta	0.001
S	0.0007

### 3.2.3. Milling conditions

Before end milling tests, the AISI H13 and Inconel 718 blocks were face milled on top and bottom surfaces to remove the heat treatment induced surface defects and ensure flatness to eliminate errors that may affect experimental results. Tool wear was generated continuously by removing material layer by layer using the end milling cutter. Table 3.2 and Table 3.3 give the cutting parameters applied in the test to study the tool wear evolution with machining time when end milling AISI H13 and Inconel 718 specimens.

Table 3.2 Milling parameters for AISI H13.

Axial depth of cut $a_p$ (mm)	Radial depth of cut $a_e$ (mm)	Cutting speed $V_c$ (m/min)	Feed per tooth $f_z$ (mm/tooth)
1	0.5	250	0.1

Table 3.3 Milling parameters for Inconel 718.

Cutting speed $V_c$ (m/min)	Axial depth of cut $a_p$ (mm)	Feed rate $v$ (mm/min)	Radial depth of cut $a_e$ (mm)	Rotational speed $N$ (rpm)
60	0.5	143.3	0.5	955.4

## 3.3. Results and discussions

### 3.3.1. Tool wears in end milling

As the schematic shown in Figure 3.2, tool wear usually refers to the gradual loss of cutting tool materials in three basic types: (1) flank wear, (2) nose wear, (3) crater wear, which

happen on flank face, tool nose region and rake face respectively. An example of tool wear after machining is shown in Figure 3.3. All these three types of tool wear cannot be studied independently since they are geometrically correlated to each other and the formation processes will interact with one another.

Flank wear describes erosion of the portion of cutting tool which is in contact with the finished part and therefore it is most commonly caused by abrasive wear of the cutting edge against the machined surface. Generally, flank wear will result in the formation of a wear land which can be monitored in production by examining the tool or checking the geometry change of the tool and machined part. Flank wear is characterized by the wear land size  $VB$  and it is the most important parameter when discussing tool wear.

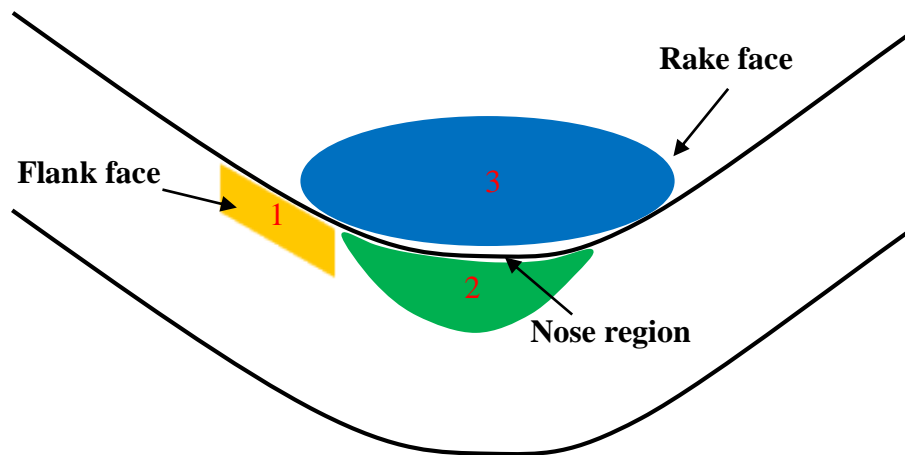


Fig. 3.2 Schematic of tool wear zones (1: flank wear, 2: nose wear, 3: crater wear).

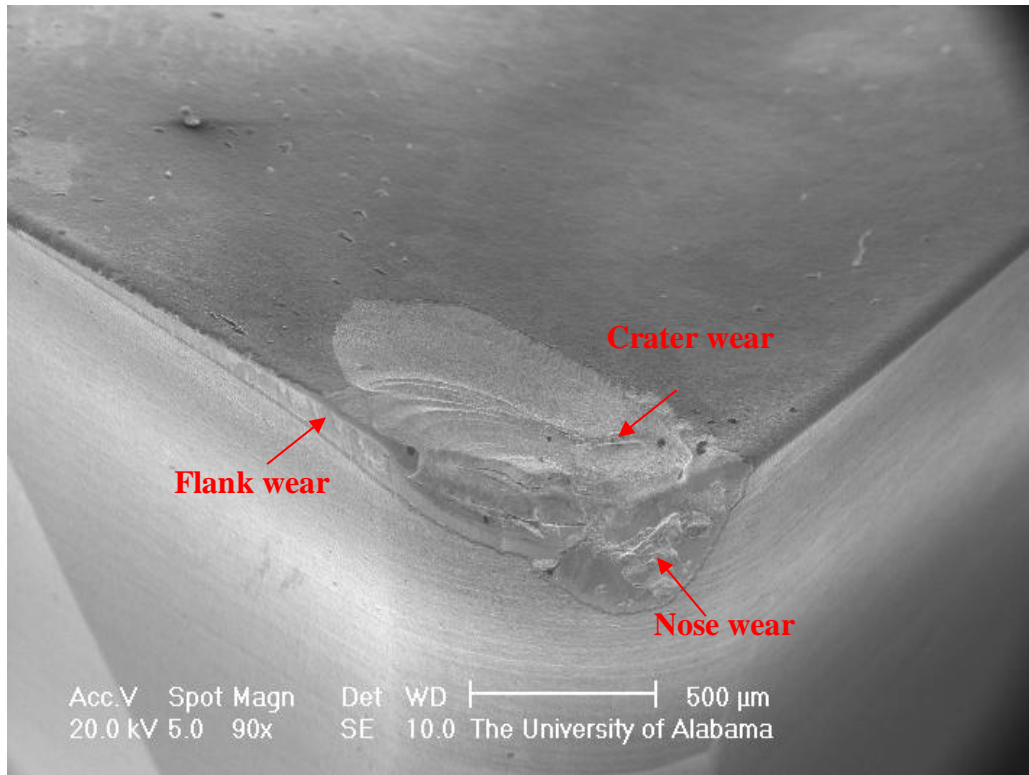


Fig. 3.3 Typical tool wear image.

Due to the abrasion between tool nose and workpiece, the tool material can be rubbed away which leads to the geometry change of the nose. The material loss happened on tool nose region will also form a wear land and this type of wear can be defined as nose wear. It occurs on the nose region of the tool and on the trailing edge near the end of the flank face. Flank wear and nose wear mutually help contributing to the formation of crater wear. Unlike flank wear, nose wear was not broadly studied since it is difficult to observe and quantify the wear land on tool nose without utilizing microscopy techniques. However, quantitatively investigating nose wear is important for analyzing the initiation and progression of wear at tool nose region.

When machined chips flow across the rake face, scars are left due to the severe friction between chips and rake face. Gradually, the rake face erodes during the continuous cutting process and then crater wear will form. Crater wear may change the actual rake angle of the tool and affect the strength of the cutting edge. It is normal for cutting tools while it does not seriously affect performance of a tool until it causes a cutting edge failure. Therefore, crater wear is usually believed to be less important than flank wear and nose wear.

Characterizing tool wear is crucial to study the wear development with cutting time and thus to justify tool life after tool wore out. For flank wear and nose wear characterization, only length of the wear land needs to be measured. While for crater wear, two or more parameters are necessary to characterize it since a concave area of no regular shape is formed after a large volume of material was removed from rake face. The complexity of crater wear geometry makes characterization work much more challenging than for flank wear.

#### 3.3.1.1. AISI H13

With the help of on-line optical tool monitoring system, the deterioration process of tool flank face when milling AISI H13 by PVD coated carbide inserts was recorded and analyzed. During the milling process, the flank faces of the two inserts were examined at an interval of 3 minute machining time. Cotton swabs damped with ethanol were used to clean the flank faces before each measurement. The optical camera took pictures of the flank face for each insert and the tool flank wear can be determined by measuring the wear length on the flank face. The maximum allowable tool flank wear has been set to be  $VB_{\max} = 250 \mu\text{m}$  which means that cutting will be stopped if one of the inserts reaches  $VB = 250 \mu\text{m}$ . Take insert 1 for example, representative optical images of tool flank wear can be seen in Figure 3.4. The relationship between tool flank wear and cutting time has been shown in Figure 3.5. Since no obvious

material loss was observed at the top right corner of tool from optical images, which indicates that nose wear and crater wear are insignificant in this milling test, only flank wear was examined.

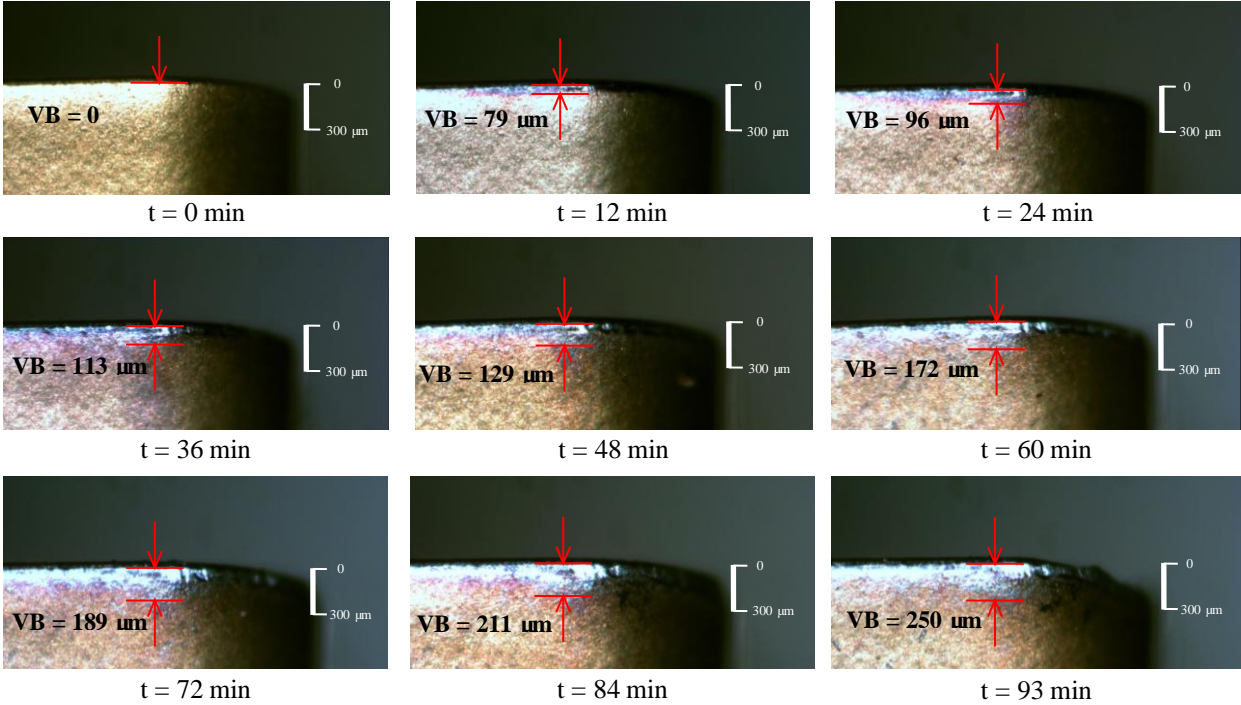


Fig. 3.4 Flank wear evolution in dry hard milling AISI H13 (PVD coated inserts).

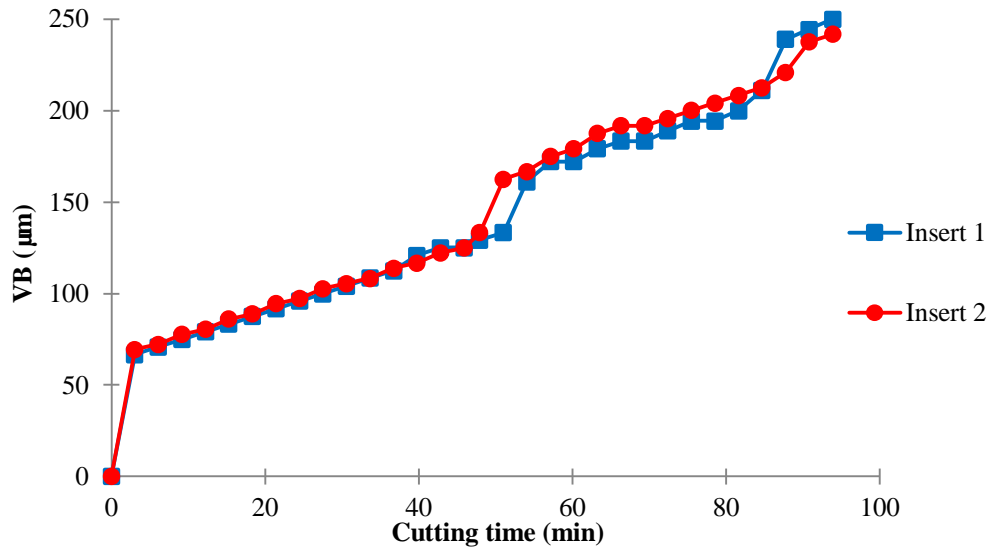


Fig. 3.5 Tool flank wear evolution in dry hard milling AISI H13 (PVD coated inserts).

Based on the flank wear evolution curve, the tool flank wear developed very fast in the first 3 minutes, from 0 to almost 70  $\mu\text{m}$ . Then, when cutting time was between 3 minutes to around 50 minutes, the flank wear steadily increased with time on the two inserts with approximately uniform increments. In this period, tool wear grew rapidly after its initiation. There were sharp increases of flank wear on both inserts from 48 to 54 minutes. After that, the tool wear increments became stable again but were slightly smaller compared with 3 - 50 minutes period. This stage can be considered as “stable zone” of the evolution curve where tool wear developed relatively slow. There was another large increase of tool wear after 84 minutes. The tool wear of insert 1 reached 250  $\mu\text{m}$  first at cutting time of 93 minutes.

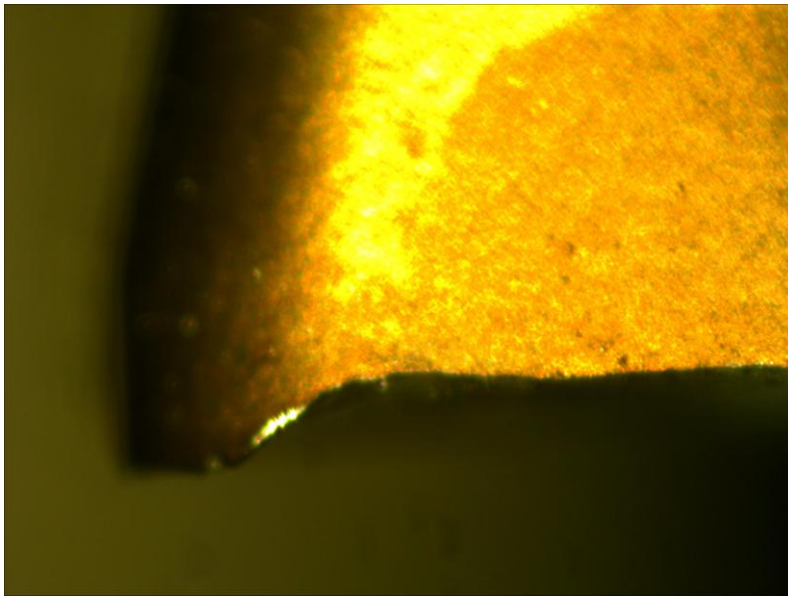


Fig. 3.6 Tool chipping (PVD coated insert).

Tool chipping happened when a piece of material broken from the bulk material of the tool, see Figure 3.6. Due to the frictional contact between the cutting tool and work material (tool flank face/work, tool rake face/chip), the work material is removed from the surface of workpiece and the tool material loss is also inevitable. The particles of tool material can be rubbed away gradually by the interfacial friction and this tool wear process is continuous. Friction generated high temperature at the cutting tip and sequential quenching by the surrounding air will alter the original mechanical properties of the cutting tool. Since the contact between tool and workpiece in milling process is intermittent instead of continuous, the heat-quench process can be repeated. This repeated heat-quench-heat phenomenon produces an equivalent heat treatment effect on the cutting tool which makes the tool material more brittle. When a critical cutting time has been reached that permits sufficient heat treatment effect, the

increased cutting forces caused by tool wear will make the tool chipping happen. Tool chipping will change the cutting tool geometry and could reduce the dimensional accuracy and repeatability of machined components. Consequently, unacceptable parts are very possible to be produced. Also, the surface roughness of the work may not meet the requirements as a result of tool geometry variation.

#### 3.3.1.2. Inconel 718

Due to the well-known rapid work hardening in machining Inconel 718, a comprehensive view of flank wear, nose wear is necessary to capture the fast tool deterioration process. Both the optical monitoring system and Philips XL 30 SEM were utilized to take images of the cutting tool at an interval of approximately 5.6 minutes. The tool flank wear values can be determined by measuring the wear length on the flank face and dimension of the wear land in tool nose region is estimated based on the scale bar from SEM and the geometrical relationship between cutting insert and electron beam. The wear evolution curves with cutting time were generated by interpolating all the data points recorded during the intervals of end milling. The end milling experiment stopped after cutting Inconel 718 for about 50.2 minutes when a catastrophic tool wear was seen and severe machine tool vibration was noticed.

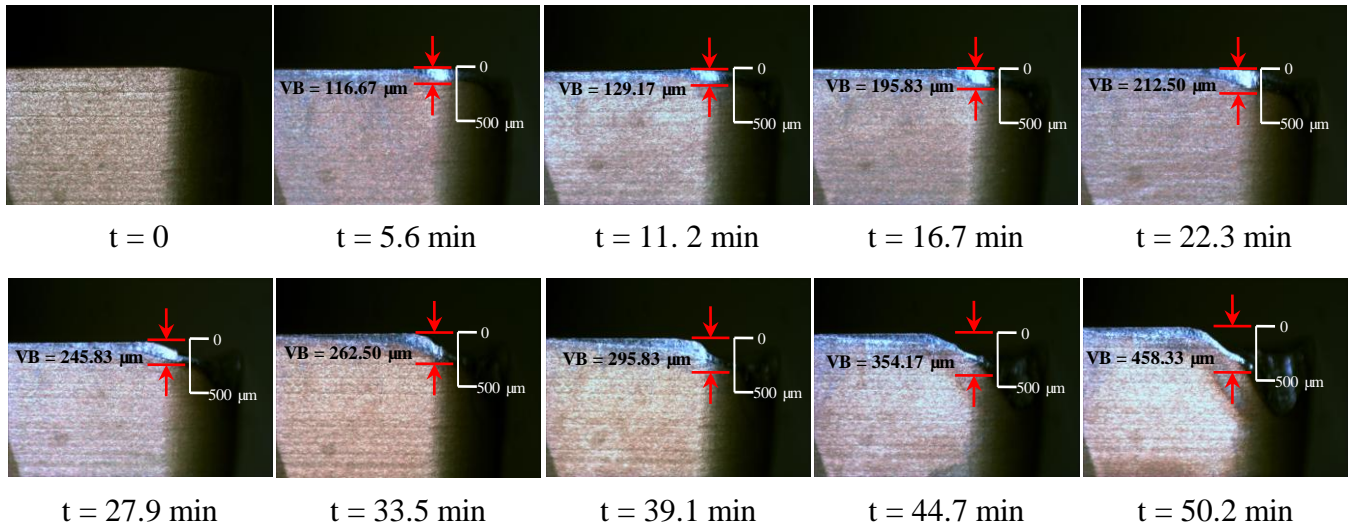


Fig. 3.7 Flank wear evolution in milling Inconel 718.

The tool flank face deterioration process was recorded and analyzed. The optical images of tool flank face at different cutting time are shown in Figure 3.7. The characterized flank wear evolution with respect to machining time is depicted in Figure 3.8.

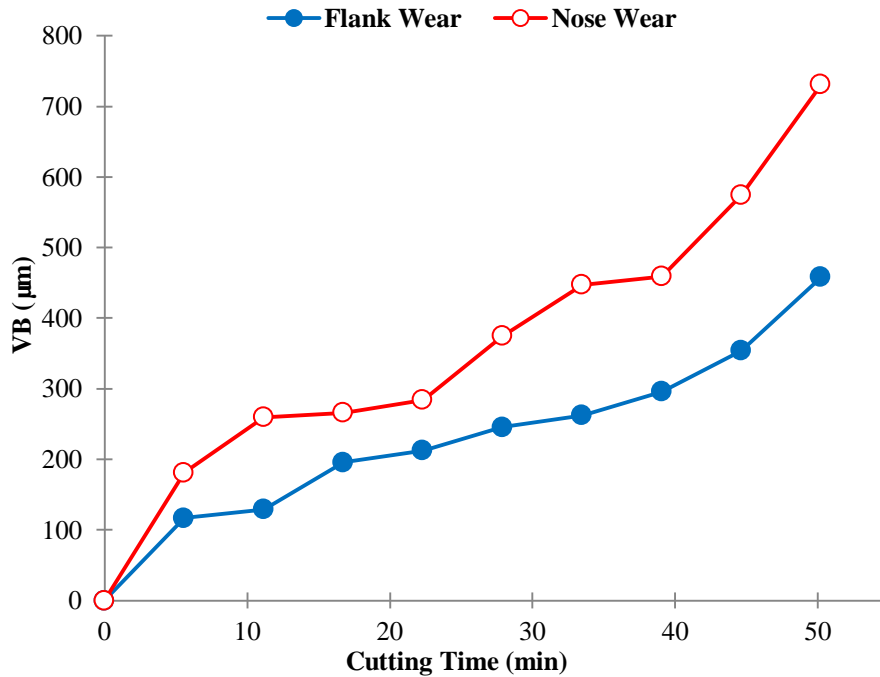


Fig. 3.8 Wear progression in milling Inconel 718.

The initiation and propagation of nose wear were observed via SEM. After examining the flank face of the cutting tool by the optical monitoring system, the insert was released from tool holder and put into sample chamber of SEM for observation. The nose wear evolution at different cutting time is shown in Figure 3.9. The trend of nose wear development is analyzed by connecting all the data points recorded during machining intervals, also see Figure 3.8.

Even though crater wear is not as significant as the previous two types of wear, we still can qualitatively analyze the development of crater wear on rake face from the SEM images, see Figure 3.9. From cutting starts to approximately 22 minutes, the cutting insert experienced only a small portion of material loss on rake face. While after around 28 minutes of cutting, an elliptical

shape crater wear began to form near the tool nose region and flank face on the rake face. It did not expand very much peripherally but developed deeper, penetrating rake face with time. Finally, large amount of material on rake face has been removed by the cutting tool and a catastrophic crater wear was observed.

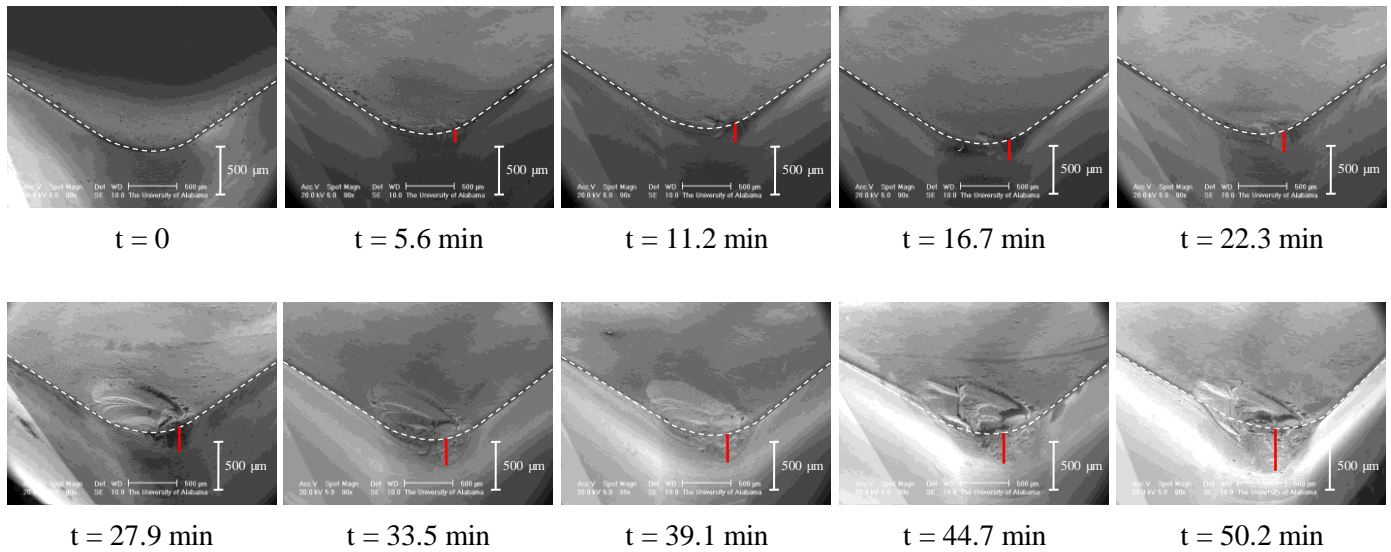


Fig. 3.9 Nose wear evolution in milling Inconel 718.

### 3.3.2. Tool wear mechanism

Tool wear can be essentially described as geometry change of cutting edge caused by the frictional contact between cutting tool and workpiece. Due to the complex nature of contact mechanism, it is uncertain where the tool wear may start and how tool wear may develop. Three basic types of tool wear: flank wear, nose wear and crater wear are seen in most of the cutting cases. However, crater wear is not often considered to be a key factor determining tool life since it does not seriously affect the use of tool until it causes failure of cutting edge. Even though various methods for tool wear monitoring have been developed by different researchers as

discussed in Section 1.2, more attention was paid to tool flank wear since it directly determines the surface integrity of machined components. As a result, its value was always considered to be the primary tool failure criterion. Actually, the nose wear will propagate and interact with wear on flank face which can eventually degrade the machined surface integrity. A catastrophic wear from either of the two types may be referred as a signal for overall tool failure. Experimental outputs, such as increased noise from cutting, more severe vibration of the machine tool, poorer work surface finish, and higher surface temperature, can also indicate the forthcoming of tool life.

The main tool failure criteria reported are crater wear and flank wear which are generally resulting from basic wear mechanisms. Dearnley and Grearson [26] evaluated principal wear mechanisms of cemented carbides and ceramics used for machining titanium alloy IMI 318 as dissolution/diffusion and attrition. Pavel et al. [25] found that the major wear mechanism was the abrasion of the binder material by the hard particles of the workpiece when using PCBN inserts to cut 1117 steel and 1137 steel. Poulachon et al. [27] concluded that the main wear mechanism of the PCBN tools when cutting AISI 52100 is abrasion by hard alloy carbide particle contained in the workpiece and the utilization of TiN coated PCBN could improve tool life.

Since tool wear is composed of several different types, tool life is therefore strongly dependent on the predetermined tool failure criteria, such as a certain maximum wear value, tool chipping, etc. As discussed above, flank wear was widely believed to be the primary parameter that determines tool life in machining. While, as shown in the overview images by SEM and wear evolution curves, nose wear develops much faster than flank wear and eventually it may induce tool chipping or severely damage the performance of the tool. Even though tool nose region does not directly contact with the machined surface, its rapid propagating should also be paid enough attention to avoid premature of cutting tool. With this consideration, tool life is not

dependent on the flank wear criterion alone and measurement of wears at different locations of cutting edge is necessary to mutually define tool failure.

### 3.4. Conclusions

The on-line optical tool monitoring system provides nondestructive evaluation of tool flank wear during milling process. No action of disassembling the tool from the spindle is needed when examining on flank face and thus in-situ monitoring tool condition can be achieved. Visible results from optical camera directly reflect what was happening on the tool/material interface and it is not necessary to correlate the object of interest with other indirect parameters. The tool deterioration process was well recorded and studied. The key results of this study can be summarized as follows:

- Tool flank wear evolution with respect to cutting time in milling AISI H13 by PVD coated inserts were observed and analyzed. Tool wear evolution curve vs. cutting time was generated by interpolating all the data points obtained. Two stages when tool wear was developing with relatively different speed were detected.
- A two-parameter method to characterize tool wear in end milling Inconel 718 including not only flank wear, but also nose wear has been proposed as a new criterion to determine tool failure in machining. Nose wear may act as a necessary supplement to the current tool failure criteria which mainly consider exclusively flank wear. Compared to flank wear on tool flank face, nose wear was developing much faster in tool nose region which quickly smoothens tool nose and makes material loss in corner area more obvious.

### 3.5. References

- [1] Kannatey-Asibu E, Dornfeld DA. A study of tool wear using statistical analysis of metal-cutting acoustic emission. *Wear* 1982; 76: 247-261.
- [2] Guo YB, Ammula SC. Real-time acoustic emission monitoring for surface damage in hard machining. *International Journal of Machine Tools & Manufacture* 2005; 45: 1622-1627.
- [3] Guo YB, Li W, Jawahir IS. Surface integrity characterization and prediction in machining of hardened and difficult-to-machine alloys: a state-of-art research review and analysis. *Machining Science and Technology* 2009; 13 (4): 437-470.
- [4] Elbestawi MA, Chen L, Becze CE, El-Wardany TI. High-speed milling of dies and molds in their hardened state. *Annals of the CIRP* 1997; 46 (1): 57-62.
- [5] Axinte DA, Dewes RC. Surface integrity of hot work tool steel after high speed milling-experimental data and empirical models. *Journal of Materials Processing Technology* 2002; 127: 325-335.
- [6] Ghani JA, Choudhury IA, Hassan HH. Application of Taguchi method in the optimization of end milling parameters. *Journal of Materials Processing Technology* 2004; 145 (1): 84-92.
- [7] Li W, Guo YB, Barkey ME, Guo C, Liu ZQ. Surface integrity and fatigue strength of hard milled surfaces. *Proceedings of the ASME 2011 International Manufacturing Science and Engineering Conference, Corvallis, OR 2011.* p. 199-206.
- [8] Koster WP, Field M. Effects of machining variables on the surface and structural integrity of titanium. *Proceedings of the North American Manufacturing Research Conference 1973.* SME 2, p. 67-87.
- [9] Koster WP. Effect of residual stress on fatigue of structural alloys. *Proceedings of the Third International Conference, ASM International, Indianapolis, IN 1991.* p. 1-9.
- [10] Guo YB, Yen DW. Hard turning versus grinding - the effect of process-induced residual stress on rolling contact. *Wear* 2004; 256: 393-399.
- [11] Brinksmeier E, Cammett JT, König W, Leskovic P, Peters J, Tönshoff HK. Residual stresses-measurement and causes in machining processes. *Annals of the CIRP* 1982; 31 (2): 491-510.
- [12] Matsumoto Y, Magda D, Hoepfner DW, Kim TY. Effect of machining processes on the fatigue strength of hardened AISI 4340 steel. *ASME J. Eng. Ind.* 1991; 113: 154-159.

- [13] Taylor D, Clancy OM. The fatigue performance of machined surfaces. *Fatigue Fract. Eng. Mater. Struct.* 1991; vol. 14, No. 2-3: 329-336.
- [14] Sharman ARC, Hughes JI, Ridgway K. An analysis of the residual stresses generated in Inconel 718TM when turning. *Journal of Materials Processing Technology* 2006; 173: 359-367.
- [15] Kim SW, Lee DW, Kang MC, Kim JS. Evaluation of machinability by cutting environments in high-speed milling of difficult-to-cut materials. *Journal of Materials Processing Technology* 2001; 111: 256-260.
- [16] Alauddin M, El Baradie MA, Hashmi MSJ. Tool-life testing in the end milling of Inconel 718. *Journal of Materials Processing Technology* 1995; 55: 321-330.
- [17] Sharman ARC, Dewes RC, Aspinwall DK. Tool life when high speed ball nose end milling Inconel 718. *Journal of Materials Processing Technology* 2001; 118: 29-35.
- [18] Jeelani S, Collins MR. Effect of electric discharge machining on the fatigue life of Inconel 718. *International Journal of Fatigue* 1988; 10 (2): 121-125.
- [19] Huang Q, Ren JX. Surface integrity and its effects on the fatigue life of the nickel-based superalloy GH33A. *International Journal of Fatigue* 1991; 13 (4): 322-326.
- [20] Li XQ, Wong YS, Nee AYC. Intelligent tool wear identification based on optical scattering image and hybrid artificial intelligence techniques. *Proceedings of the Institution of Mechanical Engineers* 1999. 213 B, p. 191-196.
- [21] Li XL, Djordjevich A, Venuvinod PK. Current-sensor-based feed cutting force intelligent estimation and tool wear condition monitoring. *IEEE Transactions on Industrial Electronics* 2000; 47: 697-702.
- [22] Iwata K, Moriwaki T. Application of acoustic emission measurement to in-process sensing of tool wear. *Annals of the CIRP* 1977; 26 (1-2): 21-26.
- [23] Kim K, Kim K, Hwang H. Progressive tool wear sensing in turning operations via acoustic emission signal processing. *American Society of Mechanical Engineers, Production Engineering Division PED* 1986. 21, p. 297-307.
- [24] Vajpayee S, Sampath A. Acoustic emission as an indirect parameter for tool monitoring. *Proceedings of Manufacturing International ASME, NY* 1988. 1, p. 321-325.
- [25] Pavel R, Marinescu I, Deis M, Pillar J. Effect of tool wear on surface finish for a case of continuous and interrupted hard turning. *Journal of Materials Processing Technology* 2005; 170: 341-349.
- [26] Dearnley PA, Grearson AN. Evaluation of principal wear mechanisms of cemented

carbides and ceramics used for machining titanium alloy IMI 318. *Material Science and Technology* 1986; 2: 47-58.

- [27] Poulachon G, Moisan A, Jawahir IS. Tool-wear mechanisms in hard turning with polycrystalline cubic boron nitride tools. *Wear* 2001; 250: 576-586.

## CHAPTER 4

### AN INVESTIGATION ON PROCESS DESIGN SPACE FOR OPTIMAL SURFACE INTEGRITY IN FINISH HARD MILLING OF TOOL STEEL

#### Abstract

Hard milling has the potential to replace finish grinding in manufacturing dies and molds. A significant impediment for wide-spread application of hard milling is the lack of understanding and control on the surface integrity of machined surface and subsurface. In this study, a Taguchi design-of-experiment based dry finish milling of AISI H13 tool steel ( $50 \pm 1$  HRc) with (Ti, Al)N/TiN coated cutting tools was conducted to investigate the process-induced surface integrity. The mechanism of surface integrity in hard milling was investigated to understand the effects of mechanical/thermal loads on surface microstructure and properties. The microstructure, microhardness and residual stresses were characterized. Phase transformation was not observed under the process parameters, while the increased microhardness and high compressive residual stresses obtained are beneficial for improving fatigue properties and wear resistance of the machined components. Finally, the process design space for the desired surface properties has been established via the microhardness and residual stress maps.

#### 4.1. Introduction

AISI H13 tool steel possesses good resistance to thermal softening and heat checking as well as a high hardenability, strength, and toughness. It is widely used to produce many types of hot work dies for forging, extrusion, and die-casting applications. Compared to grinding, electrical discharge machining (EDM), and manual finishing, the benefits of hard milling are substantial in terms of reduced machining costs and lead time.

Hard milling is characterized by high stress, strain rate, and temperature during the chip formation process along with a short interaction time between the tool and workpiece. The highly localized and rapid thermal/mechanical loading results in changes to the microstructure. The reliability of a machined component depends to a large extent on the surface integrity of the machined surface including residual stresses (RS), microstructure, and microhardness.

Depending on the nature of residual stress (compressive or tensile), it could either enhance or reduce the performances of a machined component to withstand severe loading in service. It is well documented that compressive residual stresses on the machined surface have beneficial effects on thermal fatigue, crack propagation, and stress corrosion [1,2]; while tensile residual stress reduces the component's performance. Furthermore, residual stress on a component may cause dimensional instability (distortion) after machining [3]. The increased surface hardness has been reported at gentle machining conditions and shown to improve wear resistance in sliding contact [4-6]. In the absence of a phase transformed "white layer", the increased surface hardness aids in increasing the fatigue life of components [7]. However, a

hardened layer is not necessarily beneficial. Rather, it could be harmful if the layer is associated with a poor surface finish, tensile residual stress, microstructure change, or severe surface oxidation [8].

During milling AISI H13 at different process parameters, it was found that cutting speed and feed per tooth were the significant process parameters affecting residual stresses. The increase of cutting speed and feed per tooth caused the compressive stresses to decrease due to the likely increase in thermal effect on the machined surface [9]. The tool geometry changes the contact length between tool and workpiece as well as the cutting temperature and cutting forces. Therefore, different tool geometries result in unique residual stress profiles [10]. Chen et al. [11] reported that honed edges could be employed for hard turning H13 steel. Chamfered edges produced less compressive residual stresses on the surface; however, it penetrates deeper into the workpiece. As tool wear increases, residual stress at the machined surface shifts to the tensile stress range and the residual compressive stress beneath the machined surface increases greatly [12-14]. Warren and Guo [15] further compared the characteristics of residual stress by hard cutting and grinding with various tool/wheel wear conditions. A comprehensive review of experimental study on surface integrity characterization on hardened steel alloys has been made by Guo et al. [16].

High tensile stresses were also formed in the surface layer when cutting with a coated tool, while cutting with an uncoated tungsten carbide insert at the same operating parameters produced deep compressive stresses in the subsurface [17].

The severe plastic deformation of surface material may lead to phase transformations in

the subsurface, which in turn could dramatically change the surface microstructure and its properties, for example a white layer. The hardness of a white layer is significantly higher than the tempered martensite bulk material and the grain size is in the submicrometer range between 30 and 500 nm [7,18]. So far, there are some explanations about white layer's properties and formation mechanism. Elbestawi et al. [19] found that the white layer was dependent on edge preparation and tool wear in high-speed milling of hardened AISI H13 using PCBN ball-nose end mills. However, no white layers were observed on the machined surfaces even with worn tools under the higher levels of cutting speed and feed rate in milling hardened AISI H13 steel (47-49 HRC) using the TiAlN coated carbide tools [9]. Guo and Janowski [20] suggested that mechanical deformation and thermal effects are of different relative importance in white layer formation during grinding and turning. Mechanical deformation plays a more important role in the formation of white layer during turning. While in grinding, thermal effects are greater.

The changes of microstructure and properties of the machined surface layer are influenced by many process parameters. Therefore, it is necessary to have a deeper understanding on the effects of process parameters on surface integrity of the machined surface, which enables finding a process space for the critical process parameters to achieve optimal surface integrity. In this study, a Taguchi's method based design-of-experiment of dry milling AISI H13 tool steel ( $50 \pm 1$  HRC) with (Ti, Al) N/TiN coated carbide tools has been conducted. The effects of cutting process parameters on surface integrity were analyzed. Then, a design space of process parameters for optimal surface integrity has been identified based on the experimental results.

## 4.2. Experimental procedure

### 4.2.1. Work material, machine tool and cutting tool

The workpiece material used in this study was AISI H13 tool steel with normal chemical composition and material properties listed in Tables 4.1 and 4.2, respectively. The work material was hardened and tempered to  $50 \pm 1$  HRc. Samples were sectioned into  $125 \times 25 \times 20$  mm rectangular blocks and then face milled on the top and bottom surfaces to remove any surface defects.

Table 4.1 Normal chemical composition of AISI H13 steel (wt %).

C	Mn	Si	Cr	Mo	V	Ni	Fe
0.32-0.45	0.20-0.50	0.80-1.20	4.75-5.50	1.10-1.75	0.80-1.20	0-0.30	Balance

Table 4.2 Material properties of AISI H13 steel.

Density (Kg/m <sup>3</sup> )	Young's Modulus (GPa)	Hardness (HRc)	Yield Strength (MPa)	Reduction in area (%)	Thermal conductivity (W/m K)
7800	210	$50 \pm 1$	1579	23.0	25.6

The hard milling experiments were conducted using a computer numerical controlled vertical machining center (CINCINNITI Arrow-500) without cutting fluid. The cutting tool used in the machining tests was a 20 mm diameter milling cutter equipped with two inserts. The tool-holder and the (Ti, Al) N/TiN coated carbide inserts were made by SECO Tool Company.

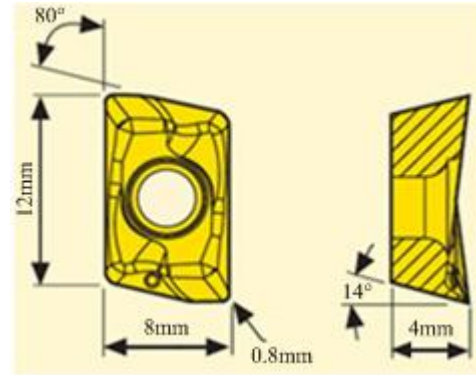
Details of the milling cutter geometry are given in Table 4.3 and shown in Figure 4.1. Only one insert was used for each set of experimental conditions. Using one insert eliminates the influence of tool tip run-out on tool wear that is commonly associated with a two-insert cutting tool. Each surface was milled using a fresh cutting edge so that the tool-wear effect on surface formation would be the same and the variation due to the wear can be minimized. The SEM (Scanning Electron Microscope) images of cutting edge before and after milling in Figures 4.1(c) and 4.1(d) indicate that tool wear is minimal even at the most abusive condition (highest cutting speed and feed). The evolution of surface integrity with tool wear will be conducted in a future study.

Table 4.3 Geometry of milling cutter.

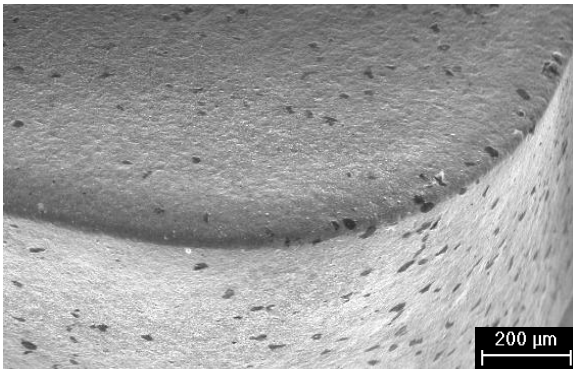
Item	Parameters
Tool holder	R217.69 - 1820.0 - 12 - 2A
Insert designation	XOMX 120408TR
Coating technique	PVD
Coating material	(Ti, Al) N/TiN
Insert clamping	Screw
Tool diameter (mm)	20
Overhang length (mm)	60
Axial rake angle (deg)	+3
Radial rake angle (deg)	-12
Clearance angle (deg)	14
Number of insert	1
Corner radius (mm)	0.8
Insert thickness (mm)	4
Insert length (mm)	12
Insert width (mm)	8



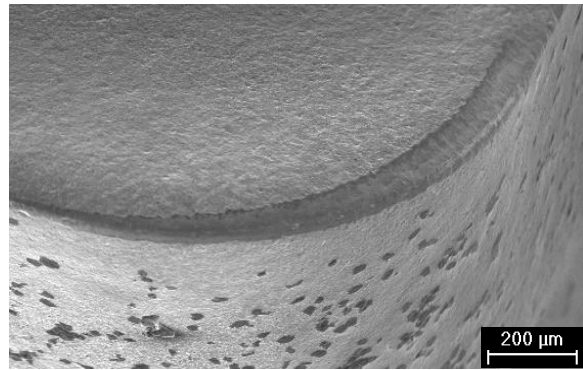
(a) Tool-holder



(b) Dimensions of cutting insert



(c) Tool edge before milling



(d) Tool edge after milling (Exp. #16)

Fig. 4.1 Edge geometry of the milling cutter: (a) Tool-holder, (b) Dimensions of cutting insert, (c) Tool edge before milling, and (d) Tool edge after milling (Exp. #16).

#### 4.2.2. Experimental design

For an experiment with four factors at four levels, Taguchi's design of experiment with a standard  $L_{16}$  ( $4^4$ ) orthogonal array was employed to conduct the hard milling experiment. The benefits of using Taguchi methods are only the main effects and two factor interactions are considered, and higher-order interactions are assumed to be non-existent [21]. The orthogonal

array was chosen because of its minimum number of required experimental trials. Four process parameters are axial depth-of-cut, radial depth-of-cut, cutting speed, and feed per tooth, respectively. Four levels of each factor were represented by '2', '1' '-1' or '-2' in the matrix. The factors and levels were assigned in Table 4.4 according to the finishing conditions for hard milling H13 steel. Each row of the matrix represents one trial. Table 4.5 shows the experimental condition according to Taguchi's design-  $L_{16} (4^4)$ . The experiments at the same condition were repeated at least 3 times to obtain representative results.

Table 4.4 Factor levels of process parameters in milling experiments.

Process parameter	Level			
	2	1	-1	-2
A—Axial depth of cut $a_p$ (mm)	1.0	1.5	2.0	2.5
B—Radial depth of cut $a_e$ (mm)	0.3	0.4	0.5	0.6
C—Cutting speed $v$ (m/min)	100	150	200	250
D—Feed per tooth $f_z$ (mm/tooth)	0.05	0.10	0.15	0.20

Table 4.5 Design-of-experiment milling experiments based on the Taguchi method -  $L_{16} (4^4)$ .

Experiment #	Process parameter				Sample #
	A ( $a_p$ )	B ( $a_e$ )	C ( $v$ )	D ( $f_z$ )	
1	2	2	1	2	Sample 1
2	2	1	2	-2	Sample 2
3	2	-1	-2	-1	Sample 3
4	2	-2	-1	1	Sample 4
5	1	2	-1	-2	Sample 5
6	1	1	-2	2	Sample 6
7	1	-1	2	1	Sample 7
8	1	-2	1	-1	Sample 8
9	-1	2	-2	1	Sample 9
10	-1	1	-1	-1	Sample 10
11	-1	-1	1	-2	Sample 11
12	-1	-2	2	2	Sample 12
13	-2	2	2	-1	Sample 13
14	-2	1	1	1	Sample 14
15	-2	-1	-1	2	Sample 15
16	-2	-2	-2	-2	Sample 16

#### 4.2.3. Sample preparation and measurement

##### 4.2.3.1. Surface characterization

Before surface integrity characterization, the milled samples were degreased by successive ultrasonic cleaning for 15 minutes in acetone and then rinsed with deionized water. Residual stresses of the machined surfaces in the feed and step-over directions were measured using an x-ray diffractometer (Bruker-AXS) with the multiple psi ( $\psi$ ) tilt method. The diffraction parameters are presented in Table 4.6. The detail of residual stress measurement method can be found in [15]. Microhardness measurements for the machined surface were conducted in two

measurement orientations; i.e., parallel and perpendicular to feed directions. The microhardness of the surface was measured at a load of 50 g for 10 s by the Knoop indenter.

Table 4.6 X-ray measurement of residual stress.

Apparatus	D8 Discovery (Bruker-AXS)
Target	Co
Wavelength $K\alpha$	1.790260 Å
Diffraction angle	$2\theta=99.7^\circ$
Diffraction plane $[hkl]$	$\alpha$ Fe [211]
Voltage	40kV
Current	35mA
Measurement method	$\text{Sin}^2\psi$
Collimator diameter	0.8 mm
Number of psi ( $\psi$ ) angles	9 (-40°; -30°; -20°; -10°; 0°; 10°; 20°; 30°; 40°)

#### 4.2.3.2. Subsurface characterization

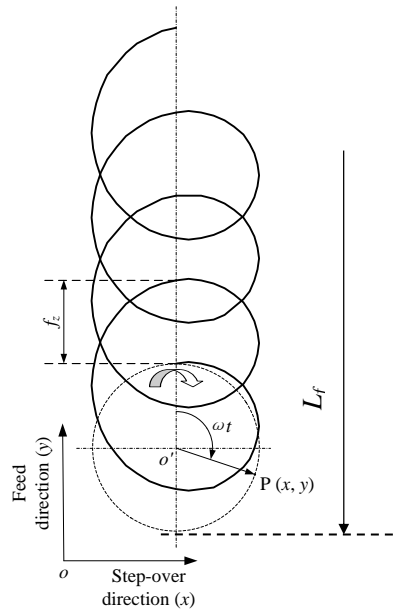
The machined samples were cross-sectioned with an abrasive cut-off saw at gentle cutting conditions to avoid excessive modification of the workpiece microstructure. The mounted specimens in cold setting epoxy were gently ground and polished in alumina powder to a mirror finish. The specimens were then etched using a 4% nital solution (4% nitric acid + 96% ethanol, by volume) for 30 s, rinsed in cold water, and dried again by air. The specimen's microstructure was viewed using optical microscopy equipped with a CCD camera (Epiphot 200, made by NIKON, Japan). Subsurface hardness was measured in approximately 10  $\mu\text{m}$  increments to a depth of 100  $\mu\text{m}$  using a Knoop indenter. In order to ensure measurement

repeatability, three measurements were made and then averaged at the same depth in the subsurface.

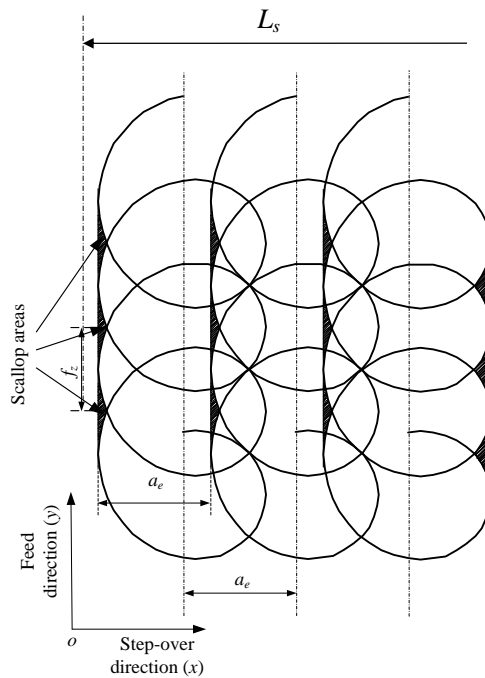
### 4.3. Results and discussions

#### 4.3.1. Surface formation mechanism

The trajectory of a cutting insert in feed direction is cycloid due to the combination of translational and rotational motions of the end mill. The cutting insert path is shown in Figure 4.2. Since only one insert is used in the present work, the interval between two successive cycloidal cutting loci is equal to the feed per tooth. When the milling cutter proceeds along the  $i$ th tool rotation, the material in the sweeping area of the cutting edge will be continuously removed by the next tool rotation. During the first cutting rotation, the surface material experiences severe plastic deformation, which leads to work-hardening and residual stresses at the machined surface and subsurface. Therefore, when a sequential cutting rotation takes place, the workpiece is in a different pseudo-initial material state, and microhardness and residual stress pattern for the second cutting rotation will also be changed from that which exists at the end of the first cutting rotation. In other words, the overlapping number of the tool locus significantly influences the variation of microhardness and the distribution of residual stresses.



(a) Cycloidal cutting locus in one pass



(b) Overlapping cutting loci in consecutive passes

Fig. 4.2 Cutting loci in end milling: (a) Cycloidal cutting locus in one pass and (b) Overlapping cutting loci in consecutive passes.

In the milling process, the overlapping number of tool locus in one cutting pass in feed direction can be calculate by

$$N_f = \text{int} \left\lfloor \frac{L_f}{f_n} \right\rfloor + 1 \quad (4.1)$$

Since only one insert ( $n = 1$ ) was used in the milling experiments, feed per revolution  $f_n$  is equal to feed per tooth  $f_z$  ( $f_n = n \cdot f_z$ ). Eq. (4.1) can be expressed as

$$N_f = \text{int} \left\lfloor \frac{L_f}{f_z} \right\rfloor + 1 \quad (4.2)$$

According to Eq. (4.2), the overlapping number of tool locus, or the number of scallop areas, on the milled surface in feed direction are determined by feed per tooth. As the feed per tooth decreases, the overlap between successive tool loci increases. The faster the tool moves in the feed direction, the surface material experiences larger strain and strain rates which further influence surface deformation.

Similarly, the overlapping number of tool locus in step-over direction is the function of the cutting length in step-over direction and radial depth-of-cut and can be calculated as

$$N_s = \text{int} \left\lfloor \frac{L_s}{a_e} \right\rfloor + 1 \quad (4.3)$$

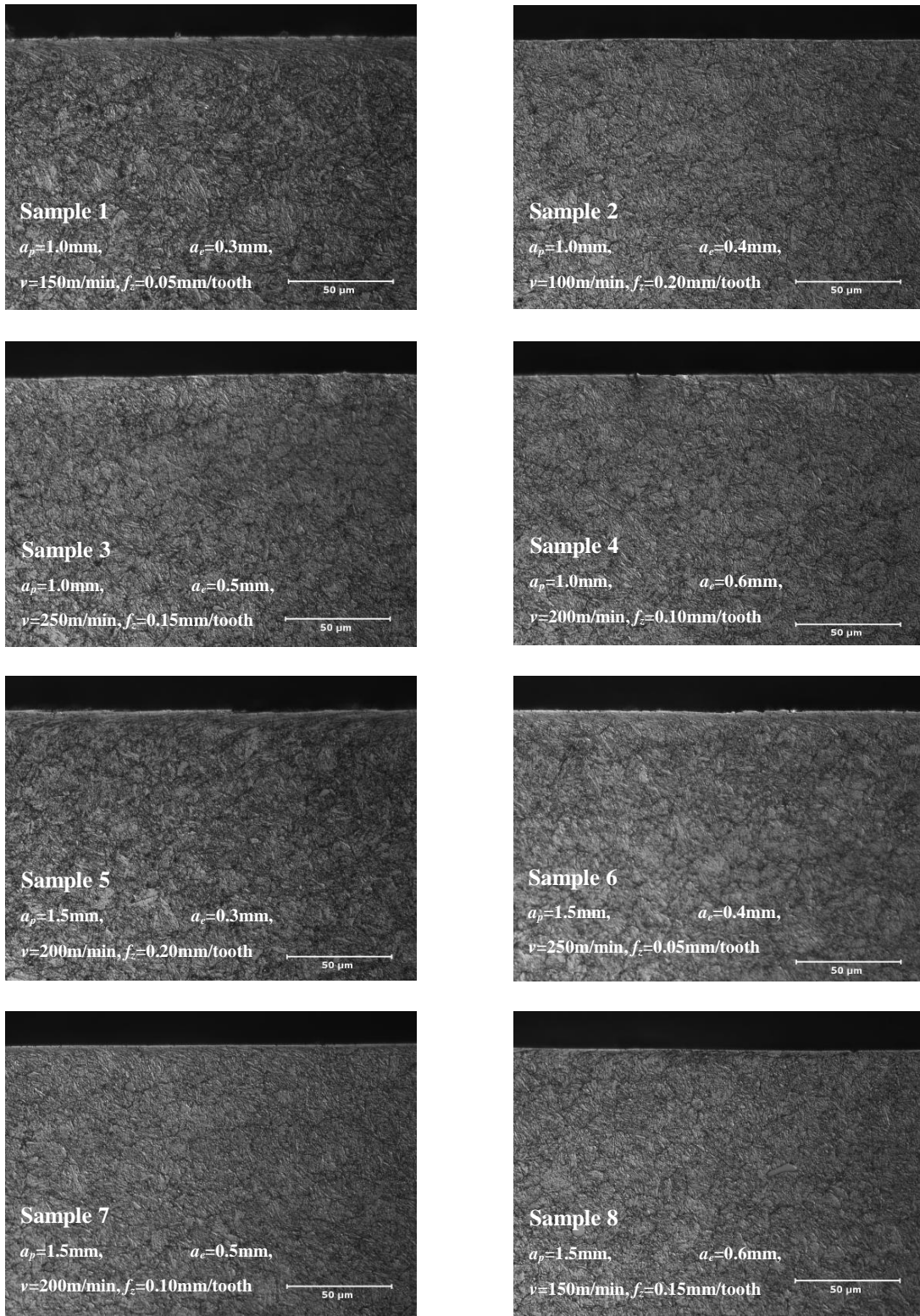
According to the above analysis, the resultant surface topography, microstructure, and metallurgical properties are determined by multiple loading cycles induced by the cutting process and subsequent rubbing effects when the cutting tool moves and rotates. Although no materials are further removed by the cutting tool in the following cutting passes, the rubbing between the tool edge and the machined surface also modify the microstructure and related surface properties

generated by the previous cut.

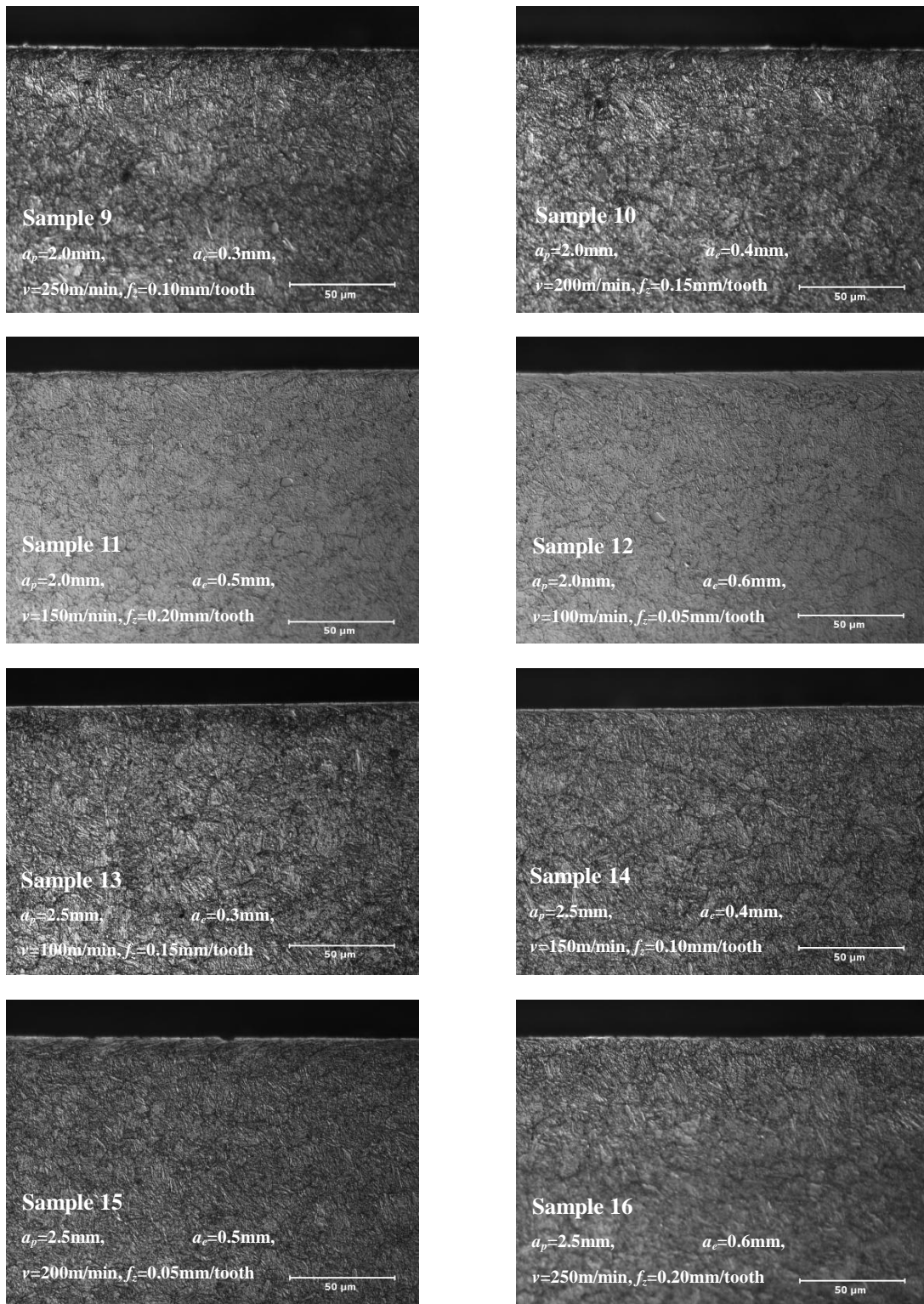
#### 4.3.2. Surface integrity characterization

##### 4.3.2.1. Microstructure

The cross-sections of the machined samples are shown in Figure 4.3. No white layers are observed even under the cutting conditions with high cutting speeds and low radial depth-of-cut (Tables 4.4 and 4.5). It indicates that the thermal effect induced by the relatively sharp cutting tool in Figure 4.1 in hard milling process is relatively small, which cannot result in a white layer. Clear shear deformation can be seen immediately beneath machined surface in most of the cases which is a significant effect of mechanical deformation, for example, sample 1 vs. sample 2. Refined grains may be produced by severe plastic deformation up to 10  $\mu\text{m}$  below the machined surface.



(a) sample 1 ~ sample 8



(b) sample 9 ~ sample 16

Fig. 4.3 Optical images of subsurface microstructure.

During hard milling process, the chips take away the majority of cutting heat, and only a small portion of heat transfers into the workpiece. For a sharp cutting tool, the contact area between the cutting tool and the machined surface is much smaller than that for a worn tool, and the percentage of the cutting heat conducted into the machined surface is very low. Considering the small flank wear as shown in Figure 4.1, the maximal temperature of the machined surface would be much lower than the austenitizing temperature during hard milling process, and there is no possibility to form a white layer on the machined surface.

#### 4.3.2.2. Microhardness

Microhardness measurements at the load of 50g were conducted in two directions: parallel and perpendicular to feed direction. Six measurements were conducted at the surface. Taking sample 5 as an example, the representative measurement array at the surface is shown in Figure 4.4. The microhardness of machined surfaces under different process parameters is shown in Figure 4.5, which is in the range of 693-1115  $HK_{0.05}$ . From this figure, it can be seen that the measurement orientations have more or less effects on the microhardness variation (up to 200  $HK_{0.05}$ ). That is to say, there is somewhat a relationship between the value of microhardness and the measurement orientation; therefore, it's necessary to specify the measurement orientation when the microhardness is measured and characterized.

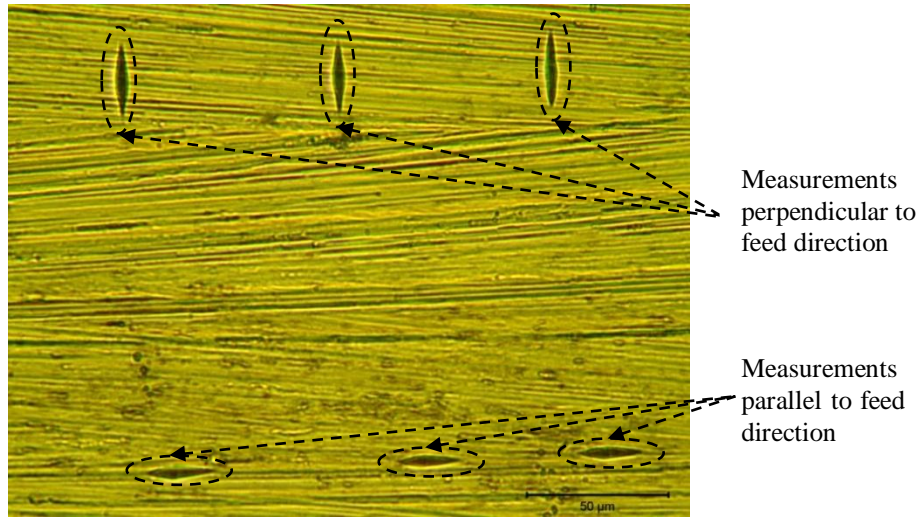


Fig. 4.4 Micro-indentation array on the top surface.

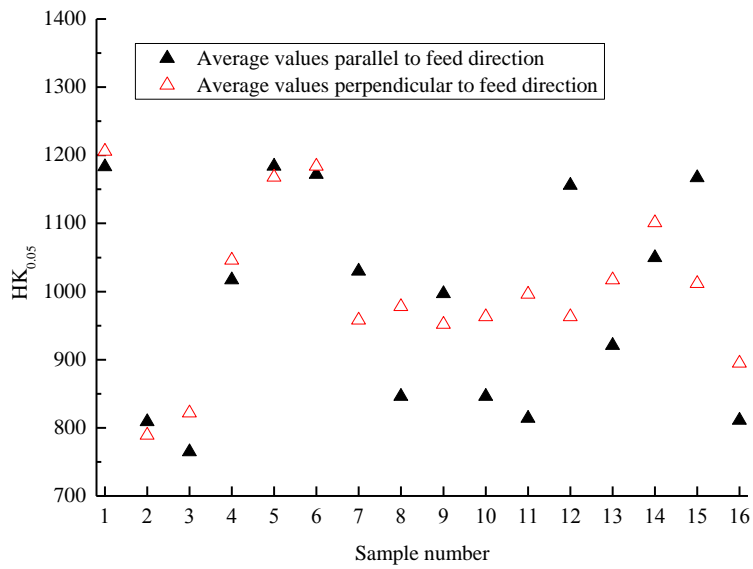


Fig. 4.5 Surface microhardness variation in parallel and perpendicular to feed directions.

Taking sample 5 as an example, the representative measurement array in the subsurface is shown in Figure 4.6. Microhardness measurement in the subsurface was conducted in a diagonal pattern to avoid interference from neighboring measurements. Each row was offset 10  $\mu\text{m}$  in the depth direction and shifted 25  $\mu\text{m}$  in the horizontal direction. The first measurement was made at an approximation of 5  $\mu\text{m}$  below machined surface. As shown in Figure 4.7, the microhardness on the machined surface is significant higher than that in the subsurface, which means there is a thin strain-hardened layer.

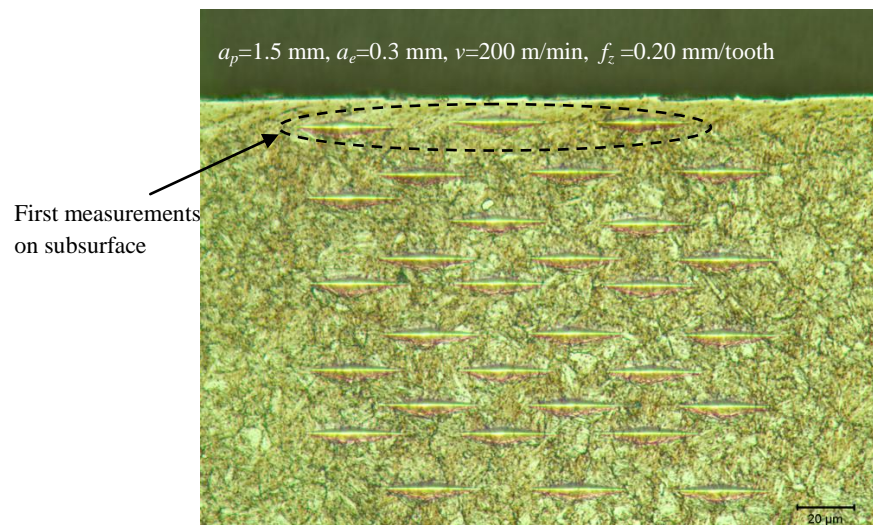
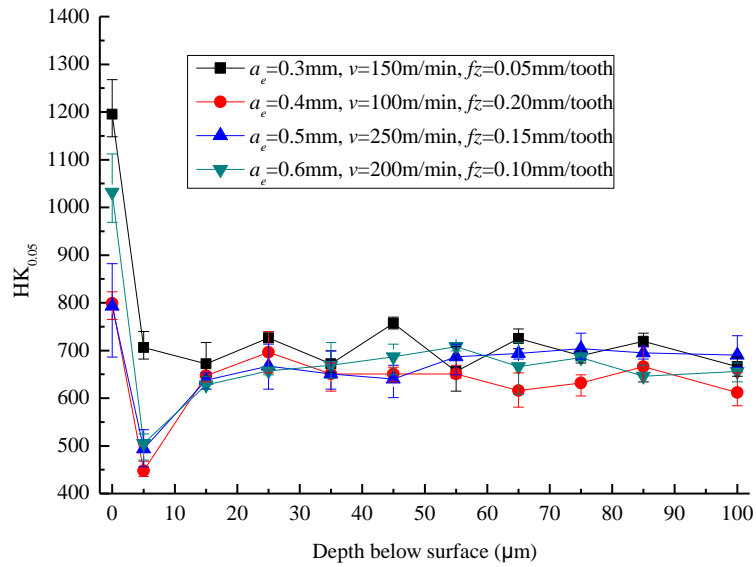
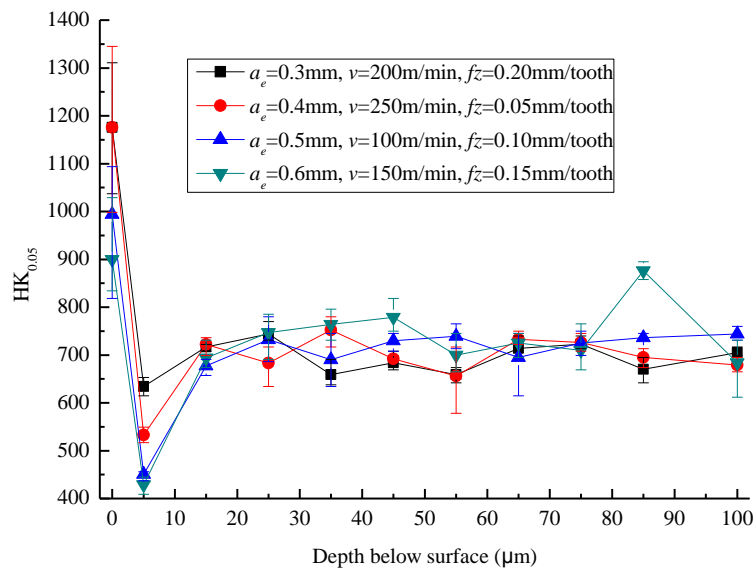


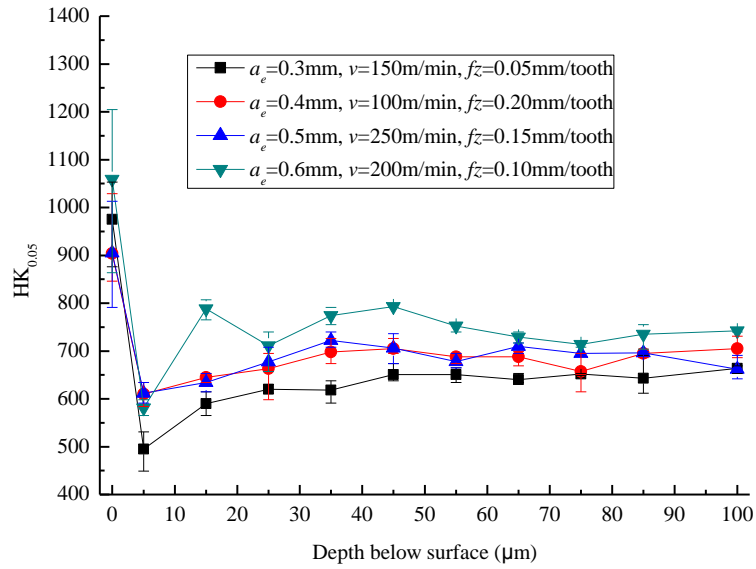
Fig. 4.6 Micro-indentation array in the subsurface.



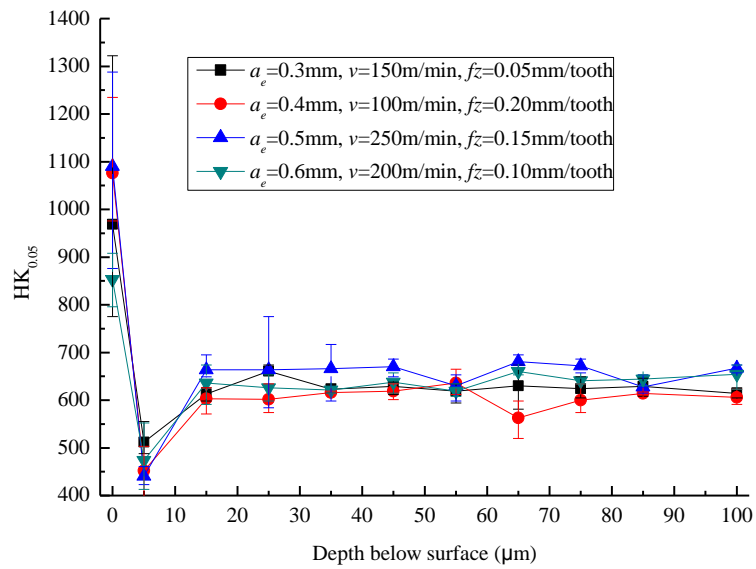
(a) Axial depth-of-cut  $a_p=1.0\text{mm}$



(b) Axial depth-of-cut  $a_p=1.5\text{mm}$



(c) Axial depth-of-cut  $a_p=2.0\text{mm}$



(d) Axial depth-of-cut  $a_p=2.5\text{mm}$

Fig. 4.7 Microhardness distributions in the subsurface.

During metal cutting process, the thermal loads often result in softening effect on workpiece materials, while mechanical loads usually introduce work-hardening effect to the workpiece materials. The final result is the sum of the above two effects. Because only a small part of cutting heat is transferred into the workpiece surface, the mechanical effects from cutting forces and rubbing between the tool edge and the workpiece surface are the predominant factors determining the microhardness variation. When subsurface depth is greater than 15  $\mu\text{m}$ , the microhardness in the subsurface becomes uniform. From Figure 4.7, it is also observed that microhardness is the lowest at the positions nearest to the top surface. However, the apparent softening is not due to thermal effects, but rather is caused by the lack of material between the indented area and the top surface which results in less resistance to deformation by a microindenter [22].

Feed rate  $v_f$  along feed direction can be calculated as

$$v_f = f_z \cdot n \cdot N \quad (4.4)$$

Similarly, only one insert ( $n = 1$ ) was used in the cutting experiments. The feed rate can be expressed as

$$v_f = f_z \cdot N \quad (4.5)$$

Because feed rate in Eq. (4.5) simultaneously combines the effects of feed per tooth and tool rotational speed (i.e. cutting speed), feed rate may be more suitable to describe the effect of individual feed per tooth and cutting speed on surface integrity. Therefore, surface integrity is mainly determined by feed rate and radial depth-of-cut. Based on the microhardness at the machined surface, the surface microhardness map under different combination of feed rate and

radial depth-of-cut is illustrated in Figure 4.8. According to the experimental results, it can be seen that the microstructure and microhardness were mainly determined by the mechanical effects from cutting forces and rubbing between the tool flank land and the workpiece surface rather than the thermal effect since the major cutting heat were carried away by the high-speed flowing chips under these cutting conditions. Therefore, there was no observed phase transformation, while the microhardness of the machined surface became higher than the bulk of the material.

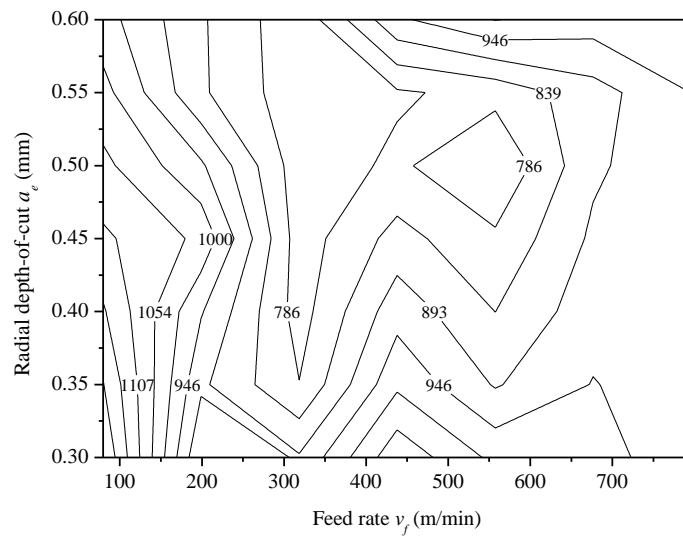


Fig. 4.8 Surface microhardness ( $HK_{0.05}$ ) contour under the combined influence of feed rate and radial depth-of-cut.

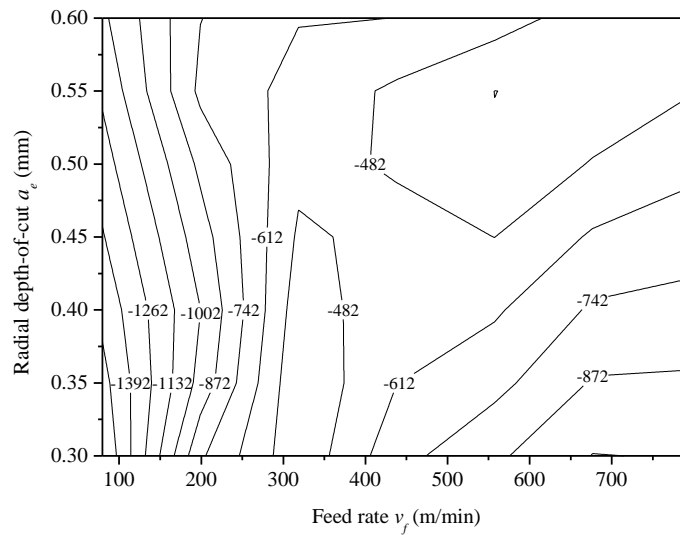
When low feed rates ( $v_f \leq 200$  mm/min) were used, the decrease of surface microhardness with the increase of the radial depth-of-cut can be explained by the reduced rubbing effect with

the increase of radial depth-of-cut. The mechanical effect rather than thermal effect becomes a predominant factor for determining microhardness. When moderate to high feed rates (from 200 to 800 mm/min) were employed, the feed rate has little influence on the variation of microhardness with the radial depth-of-cut. When the radial depth-of-cut was lower than 0.5 mm, the surface microhardness decreased with the increase of radial depth-of-cut. In contrast, when the radial depth-of-cut was higher than 0.5 mm, surface microhardness increased with the increase of radial depth-of-cut.

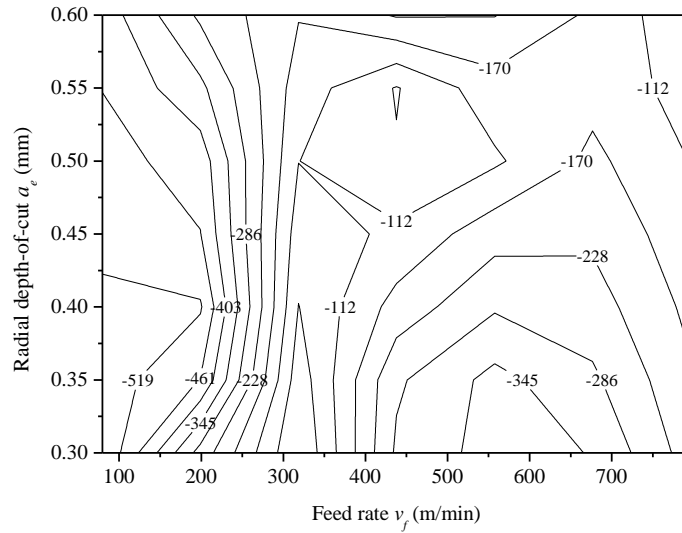
#### 4.3.2.3. Residual stresses

The measured normal residual stresses in feed and step-over directions under the combined influence of feed rate and radial depth-of-cut are shown in Figures. 4.9(a) and 4.9(b). The normal residual stresses in feed and step-over directions were all compressive, which indicates the mechanical effect is dominant while the thermal effect is secondary. In most cases, the magnitudes of normal residual stresses in feed and step-over directions decrease with the increase of radial depth-of-cut or feed rate. Comparing the residual stresses contours in the two directions, it can be seen that the magnitudes of normal residual stresses in feed direction are much larger than that in step-over direction. The normal residual stresses in feed direction are up to -1392 MPa, while the maximal magnitude in step-over direction is only -519 MPa. The experimental data of residual stress indicates that the measured normal residual stresses are very directional. The result can be explained that during finish hard milling process, feed per tooth is much smaller than radial depth-of-cut, which results in the very different mechanical and thermal loads in feed direction from that in step-over direction.

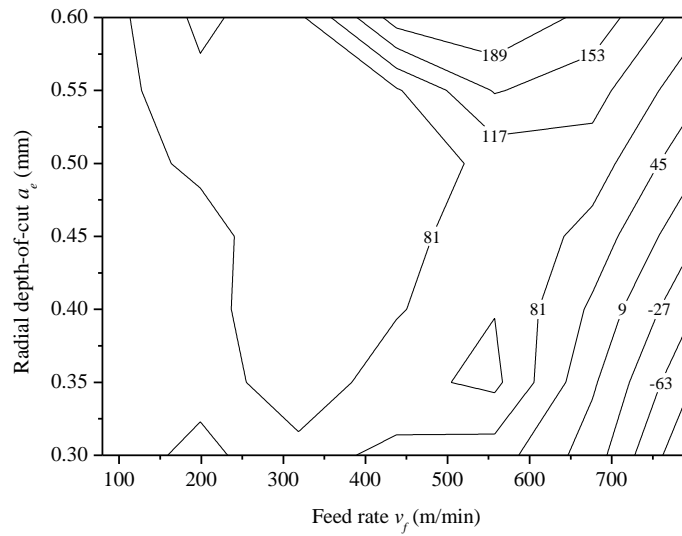
The shear residual stresses are plotted in Figure 4.9(c). The magnitudes of the shear residual stresses vary from -63 to 189 MPa, which are very small compared with those normal residual stresses. The effect of shear residual stresses on component performance would be negligible.



(a) Normal residual stress (MPa) in feed direction



(b) Normal residual stress (MPa) in step-over direction



(c) Shear residual stress (MPa)

Fig. 4.9 Residual stress contours under the combined influence of feed rate and radial depth-of-cut: (a) Normal residual stress in feed direction, (b) Normal residual stress in step-over direction, and (c) Shear residual stress.

#### 4.3.3. Process parameter space for desired surface integrity

The microstructural alteration, microhardness, residual stresses, as well as surface finish, all influence fatigue, corrosion, and tribology performances of the machined components. In general, in order to improve fatigue resistance, phase transformation (white layer) should be avoided; while work-hardening and compressive residual stresses are desired [23]. As analyzed above, phase transformation, microhardness variation and residual stresses induced by hard milling are all related to process parameters. Thus, by optimizing process parameters, a desired surface integrity may be obtained to improve fatigue, corrosion, and wear resistance of machined components.

Under the concerned process parameters in Table 4.5, no white layers were formed on the machined surfaces. According to Figures 4.8 and 4.9, it can be seen that the process space of low feed rate ( $v_f \leq 200$  mm/min) and radial depth-of-cut ranging from 0.3 to 0.6 mm can introduce high microhardness and compressive residual stresses. Therefore, in order to generate a desired surface integrity, the process space of low feed rate ( $v_f \leq 200$  mm/min) and radial depth-of-cut ranging (0.3 - 0.6 mm) would be suitable for finish hard milling of AISI H13 tool steel with (Ti, Al) N/TiN coated cutting tools.

#### 4.4. Conclusions

A Taguchi design-of-experiment based dry finish milling hardened AISI H13 steel with (Ti, Al) N/TiN coated end mill has been conducted to investigate the effects of process

parameters on surface integrity. Process parameter spaces for desired surface integrity have been found via experimental results. The major results may be summarized as follows:

- The machined subsurface of about 10  $\mu\text{m}$  has experienced severe shear deformation. However, no phase transformation induced white layer can be observed.
- A significant strain-hardening zone of about 15  $\mu\text{m}$  in the subsurface occurred, which shows that the milled surfaces have a higher microhardness.
- The measurement orientations have substantial influence on microhardness data. It is necessary to specify the measurement orientation when microhardness is measured, characterized, and reported.
- The normal residual stresses in feed and step-over directions were all compressive and increase with the increase of radial depth-of-cut and feed rate, which is beneficial for surface performance in service. Compared to the magnitudes of normal residual stresses, the shear residual stresses are very small and, therefore, could be neglected.
- The process parameter space for desired surface integrity via the feed rate and radial depth-of-cut has been recommended based upon their combined effects on microstructure, microhardness, and residual stress distributions.
- The characteristics of surface integrity in hard milling AISI H13 would be similar to those in milling of other die/mold steels.

#### 4.5. Nomenclature

$a_e$  = Radial depth-of-cut (mm)

$a_p$  = Axial depth-of-cut (mm)

$f_z$  = Feed per tooth (mm/tooth)

$f_n$  = Feed per revolution (mm/tooth)

$v_f$  = Feed rate (mm/min)

$N$  = Rotational speed of spindle (rev/min)

$n$  = Number of the insert

$L_f$  = Cutting length in feed direction (mm)

$L_s$  = Cutting length in step-over direction (mm)

$N_f$  = Overlapping number of the tool locus in one cutting pass

$N_s$  = Overlapping number of the tool locus in step-over direction

#### 4.6. References

- [1] Moshier MA, Hillberry BM. The inclusion of compressive residual stress effects in crack growth modeling. *Fatigue & Fracture of Engineering Materials & Structures* 1999; 22: 519-526.
- [2] Toribio J. Role of crack-tip residual stresses in stress corrosion behaviour of prestressing steel. *Construction and Building Materials* 1998; 12: 283-287.
- [3] Schultz R, Karabin M. Characterization of machining distortion by strain energy density and stress range. *Mater. Sci. Forum* 2002; 404-407: 61-67.

- [4] Guo YB, Warren AW. Microscale mechanical behavior of the subsurface by finishing processes. *ASME J. Manuf. Sci. Eng.* 2004; 127: 333-338.
- [5] Sasahara H. The effect on fatigue life of residual stress and surface hardness resulting from different cutting conditions of 0.45% C steel. *Int. J. Mach. Tools Manuf.* 2005; 45: 131-136.
- [6] Viáfara CC, Castro MI, Vázquez JM, Toro A. Unlubricated sliding wear of pearlitic and bainitic steels. *Wear* 2005; 259: 405-411.
- [7] Schwach DW, Guo YB. A fundamental study on the impact of surface integrity by hard turning on rolling contact fatigue. *Int. J. Fatigue* 2006; 28: 1834-1844.
- [8] Zarudi I, Zhang LC. Mechanical property improvement of quenched steel by grinding. *J. Mater. Sci.* 2002; 37: 3935-3943.
- [9] Axinte DA, Dewes RC. Surface integrity of hot work tool steel after high speed milling-experimental data and empirical models. *J. Mater. Process. Technol.* 2002; 127: 325-335.
- [10] Marques MJ, Outeiro J, Dias AM, M Saoubi R, Chandrasekaran H. Surface integrity of H13 ESR mould steel milled by carbide and CBN tools. *Mater. Sci. Forum* 2006; 514-516: 564-568.
- [11] Chen L, El-Wardany TI, Nasr M, Elbestawi MA. Effects of edge preparation and feed when hard turning a hot work die steel with polycrystalline cubic boron nitride tools. *Annals of the CIRP* 2006; 55: 89-92.
- [12] König W, Klinger M, Link R. Machining hard materials with geometrically defined cutting edges - field of applications and limitations. *Annals of the CIRP* 1990; 39: 61-64.
- [13] Tönshoff HK, Wobker HG, Brandt D. Hard turning - influences on the workpiece properties. *Trans. NAMRI/SME* 1995; 23: 215-220.
- [14] Liu M, Takag J, Tsukuda A. Effect of tool nose radius and tool wear on residual stress distribution in hard turning of bearing steel. *J. Mater. Process. Technol.* 2004; 150: 3234-3241.
- [15] Warren AW, Guo YB. Characteristics of residual stress profiles in hard turned versus ground surfaces with and without a white layer. *ASME J. Manuf. Sci. Eng.* 2009; 131:

1-10.

- [16] Guo YB, Li W, Jawahir IS. Surface integrity characterization and prediction in machining of hardened and difficult-to-machine alloys: a state-of-art research review and analysis. *Machining Science and Technology* 2009; 13(4): 437-470.
- [17] Sharman ARC, Hughes JJ, Ridgway K. Workpiece surface integrity and tool life issues when turning Inconel 718 nickel based superalloy. *Machining Sci. and Tech.* 2004; 8: 399-414.
- [18] Akcan S, Shah S, Moylan SP, Chhabra PN, Chandrasekar S, Yang HTY. Formation of white layers in steels by machining and their characteristics. *Metall. Mater. Trans. A* 2002; 33: 1245-1254.
- [19] Elbestawi MA, Chen L, Becze CE, El-Wardany TI. High-speed milling of dies and molds in their hardened state. *Annals of the CIRP* 1997; 46: 57-62.
- [20] Guo YB, Janowski GM. Microstructural characterization of white layers by hard turning and grinding. *Trans. NAMRI/SME* 2004; 34: 367-374.
- [21] Taguchi G. *Taguchi on robust technology development: bringing quality engineering upstream.* ASME Press, New York 1993.
- [22] Warren AW, Guo YB. On the clarification of surface hardening mechanisms by hard turning and grinding. *Trans. NAMRI/SME* 2006; 34: 309-316.
- [23] Guo YB, Warren AW, Hashimoto F. The basic relationships between residual stress, white layer, and fatigue life of hard turned and ground surfaces in rolling contact. *CIRP J. Manuf. Sci. Tech.* 2010; 2: 129-134.

## CHAPTER 5

### A FUNDAMENTAL STUDY OF TOOL WEAR EFFECT ON SURFACE INTEGRITY AND FATIGUE LIFE OF TOOL STEEL BY DRY HARD MILLING

#### Abstract

Hard milling is a competitive finishing process in mold/die manufacturing. Tool wear during hard milling adversely affects surface integrity and fatigue performance of the machined components. Surface integrity and machining accuracy deteriorate when tool wear progresses. In this paper, the effect of tool wear on surface integrity and its impact on fatigue performance of AISI H13 tool steel ( $50 \pm 1$  HRC) by dry milling using PVD coated tools are studied. The evolutions of surface integrity including surface roughness, microstructure, residual stresses, and microhardness were characterized at three levels of tool flank wear ( $VB = 0, 0.1$  mm,  $0.2$  mm). At each level of tool flank wear, the effects of cutting speed, feed, and radial depth-of-cut on surface integrity were investigated respectively. It shows that surface roughness in the step-over direction is much higher than that in the feed direction under all the milling conditions. The increased tool wear did not necessarily produce a rougher surface in both directions. Optical images of the subsurface microstructure of the 21 machined samples do not show a noticeable white layer or heat affected zones which may be explained by the characteristic of periodic tool/work contact in milling compared to turning and grinding. Residual stresses are compressive in both directions and are more compressive in the step-over direction than in the feed direction.

Four-point bending fatigue tests were performed using the samples machined at different flank wear conditions. The results show that generally a worn tool reduces fatigue life, and the larger the tool wear, the shorter the fatigue life. The fractured surfaces of fatigued samples were characterized. Fatigue endurance limits of the machined surfaces at different reliability levels were estimated and correlated with the experimentally determined fatigue life.

### 5.1. Introduction

Dry hard milling is a sustainable machining process to make precision molds, dies, and other various mechanical components. However, tool wear is undesirable but inevitable in machining of hardened steels since it may cause poor surface integrity and fatigue performance of a machined surface.

Tool wear is a complex phenomenon occurring in the metal cutting process. Tool wear refers to the degradation of the cutting tool in three basic modes: (a) gradual loss of tool materials; (b) fracture of the cutting edge; and (c) reduced mechanical properties of the tool [1]. When a tool is used for cutting mechanical parts, a decision must be made whether a worn tool should be replaced by a new one before the next cutting, or if the worn tool can still be used but the cutting parameters need to be changed to adapt to the tool condition. The most conservative way to get components machined with desired quality is to replace the worn tool with a new one. However, this will increase manufacturing cost and reduce the production efficiency since more tools will be used and extra time for replacement will be spent.

Tool wear is considered to be a critical factor that determines the economy of a machining process since it is closely related to cutting tool life and thus the overall cost of production. Two types of tool wear will occur: flank wear (the portion of the tool in contact with

the newly machined surface) and crater wear (the portion of the tool on the tool/chip interface). Generally, crater wear only has a minor effect on surface integrity of a machined component unless it causes a cutting edge failure. Therefore, flank wear is always the most important wear mode when surface integrity is concerned. A worn tool increases cutting temperature which may result in a thin white layer and tensile residual stress on the machined surface [2]. Compared with a sharp tool, a worn tool will produce poor surface integrity and fatigue performance of the machined surfaces. Surface integrity and fatigue performance of the machined surfaces would deteriorate to an unacceptable level due to the progression of tool wear. Consequently, surface integrity and fatigue performance cannot be guaranteed and more energy is expected to be consumed in machining when a worn tool is used. It is the primary objective for manufacturers to produce as many quality parts as possible while minimizing machining costs. However, few researchers have bridged between tool wear and surface integrity of machined components under the progression of tool wear. In order to achieve multiple objectives of production efficiency, fatigue life, and manufacturing cost, the relationship between tool wear, surface integrity, and fatigue performance of machined components needs to be thoroughly studied to provide a general guidance for production.

In this research, the effect of tool flank wear on surface integrity, fatigue strength, and fatigue life of components by dry hard milling was studied. The evolution of surface integrity at different levels of tool flank wear and various combinations of process parameters was investigated. Tool wear values were measured by an on-line optical tool inspection and measurement system [3]. Surface integrity to be characterized includes surface roughness, microstructure, residual stress, and microhardness. The endurance limits and fatigue life of the machined components were experimentally determined. By correlating tool flank wear, surface

integrity, and fatigue performance, a process space with acceptable tool flank wear can be determined for designed fatigue life with controlled variance for machined components.

## 5.2. Literature review

Machined components have broad applications. Component performance is always the first concern from the customers' perspective regardless of specific application. The performance of machined components largely depends on the machining process which generally defines surface integrity. Tool wear is the dominant factor that affects surface integrity. Therefore, the relationship between tool wear, process parameters, and surface integrity should be well studied in order to maintain the desired quality of products in mass production. In this context, experiments have been done to link the surface integrity of machined parts and cutting tool flank wear, process parameters.

AISI H13 is one of the most versatile hot work tool steels in pressure die casting, extrusion, hot forging and extrusion mandrels [4]. Dry machining hardened steel can be cheaper, faster, more flexible, and more environmentally friendly compared to grinding and other finishing processes [5]. Experimental studies on the relationship between chip morphology, phase transformation, and process space for optimal surface topography in finish hard milling AISI H13 have been conducted by Zhang and Guo [6]. Surface integrity, including microstructure and microhardness, generated by hard milling AISI H13 tool steel has been characterized and analyzed by Li et al. [7]. Elbestawi et al. [8] found that white layer was dependent on edge preparation and tool-wear in high-speed milling of hardened AISI H13 using PCBN ball-nose end mills. Sharp edge preparations outperform honed and chamfered edges and produced a thinner white layer. However, no white layers or other microstructural alterations

were observed on the machined surfaces even with worn tools under the higher levels of cutting speed and feed rate when hardened H13 steel (HRC 47-49) was machined using TiAlN coated carbide tools [9]. Axinte et al. [9] investigated the influence of cutting speed and feed rate on surface roughness using a full factorial experimental design in milling hardened AISI H13 steel with TiAlN coated tools. Surface roughness values increased when cutting speed increased and feed per tooth decreased due to higher process instability in the ball nose end milling tests. Ghani et al. [10] has shown that the use of high cutting speed, low feed rate and low depth-of-cut leads to a good surface finish in semi-finish and finish machining hardened AISI H13 steel with TiN-coated carbide insert tools. A review of experimental study on surface integrity characterization has been made by Guo et al. [5]. They concluded that residual stress has been generally recognized as the key factor among all surface integrity parameters which not only significantly affects product performance, but also serves as a key criterion for process selection.

The effects of cutting tool flank wear and surface integrity on fatigue life of machined components were also studied by several investigators. Koster and Field [11] suggested that the main mechanical property affected by machining is high cycle fatigue strength and the actual endurance limit depends on the particular process used and the severity of operation. In early fatigue models [12-14], fatigue life was often attributed to surface roughness parameter Ra (arithmetic average). Koster [15] summarized experimental work on fatigue strength of different workpiece materials (iron, nickel and titanium based alloys) subject to a range of machining processes: finish grinding, milling and turning. He found that the endurance limit of steel was dependent on surface roughness while other two were not. Surface residual stress has also been suggested to be an important indicator of fatigue performance. Taylor and Clancy [16] concluded that surface roughness had a distinct effect on the fatigue life. Machining induced residual stress

has been recognized as one of the main factors which will significantly affect fatigue life [15,17]. Matsumoto et al. [18] studied the effect of machining processes on the fatigue strength of AISI 4340 and they found that the average fatigue life of cut samples was higher than those ground samples. Guo et al. [19] concluded that the nature of surface residual stress and the depth of maximum compressive residual stress in the subsurface are important for rolling contact fatigue damage.

### 5.3. Tool wear vs. surface integrity experiment

End milling of AISI H13 experiments were carried out without coolant on a 3-axis CINCINNATI Arrow 500 CNC vertical machine. Tool flank wear was monitored and measured by an on-line optical tool monitoring system integrated with the CNC machine.

#### 5.3.1. Work material and cutting tool

The AISI H13 work samples used in dry hard milling experiments were 20 mm × 21 mm × 13 mm rectangular blocks. They were thoroughly hardened and tempered to  $50 \pm 1$  HRC. Before milling tests, the top and bottom sample surfaces were ground to remove the heat treatment induced surface defects and ensure flatness to eliminate machining errors.

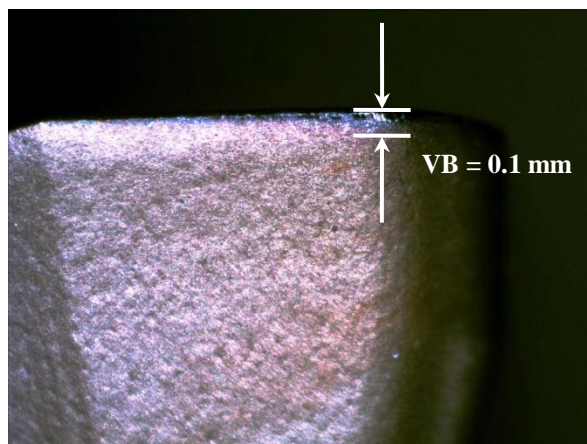
The cutting tool used in the milling tests was a 20 mm diameter end milling cutter with two PVD (Ti, Al) N-TiN-coated carbide inserts. The tool holder and the PVD-coated inserts were made by SECO Tool Company.

### 5.3.2. Experimental design

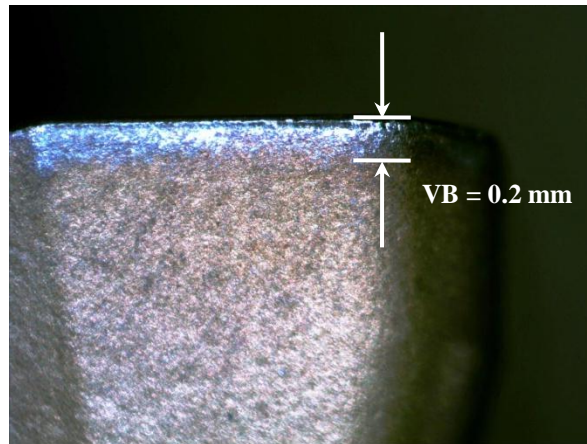
Table 5.1 lists the process conditions for the milling experiments. 21 cutting tests (7 different cutting conditions, with 3 levels of initial tool flank wear:  $VB = 0$ ,  $VB = 0.1$  mm, and  $VB = 0.2$  mm used for each cutting condition, see Figure 5.1) were planned to study the effect of tool flank wear on surface integrity under a variety of cutting parameter combinations.



(a) Fresh tool (flank wear = 0)



(b) Tool with flank wear = 0.1 mm



(c) Tool with flank wear = 0.2 mm

Fig. 5.1 Initial tool flank wear.

Table 5.1 End milling plan for tool wear vs. surface integrity experiment.

Sample #	VB (mm)	Cutting condition #	Cutting speed [m/min]	Feed per tooth [mm/tooth]	Radial DOC [mm]
1	0	1	100	0.1	0.5
2	0.1				
3	0.2				
4	0	2	200	0.1	0.5
5	0.1				
6	0.2				
7	0	3	300	0.1	0.5
8	0.1				
9	0.2				
10	0	4	200	0.05	0.5
11	0.1				
12	0.2				
13	0	5	200	0.2	0.5
14	0.1				
15	0.2				
16	0	6	200	0.1	0.3
17	0.1				
18	0.2				
19	0	7	200	0.1	0.4
20	0.1				
21	0.2				

### 5.3.3. Sample preparation

The machined samples were degreased by successive ultrasonic cleaning for 15 minutes in acetone, and then rinsed with deionized water before characterization of surface integrity. Then, the samples were cross-sectioned with an abrasive cut-off saw at gentle cutting conditions to avoid excessive modification of surface integrity. After being mounted in cold setting epoxy, the samples were gently polished to a mirror-like finish. The samples were then etched using a 4% nital solution (4% nitric acid + 96% ethanol, by volume), rinsed in cold water, and air dried.

### 5.3.4. Surface integrity characterization

Machining induced surface integrity can be generally described by its topological, mechanical, metallurgical and chemical states [20]. Surface integrity factors including: surface roughness, microstructure, residual stresses, and microhardness were characterized in this study.

#### 5.3.4.1. Surface roughness

Surface roughness along feed direction and step-over direction was measured by a Sloan Dektak II profiler. In order to get statistical stable data, three measurements along each direction were made at different locations when tracing 4 mm on the machined surfaces. Figure 5.2 shows the measurement configuration for the machined surfaces. The measured surface roughness along the feed direction and the step-over direction was shown in Figure 5.3.

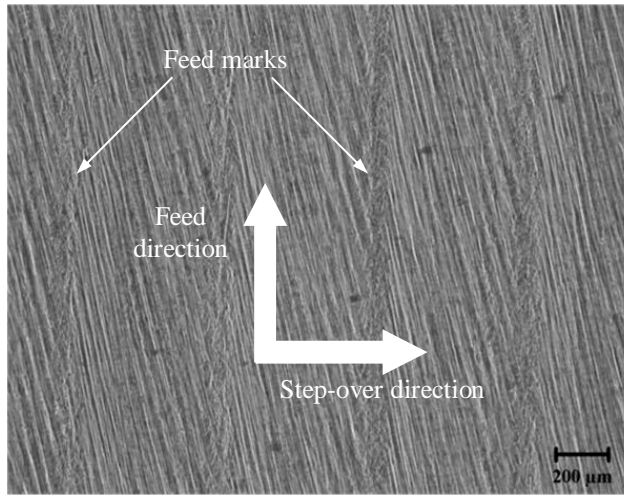


Fig. 5.2 Texture of machined surface.

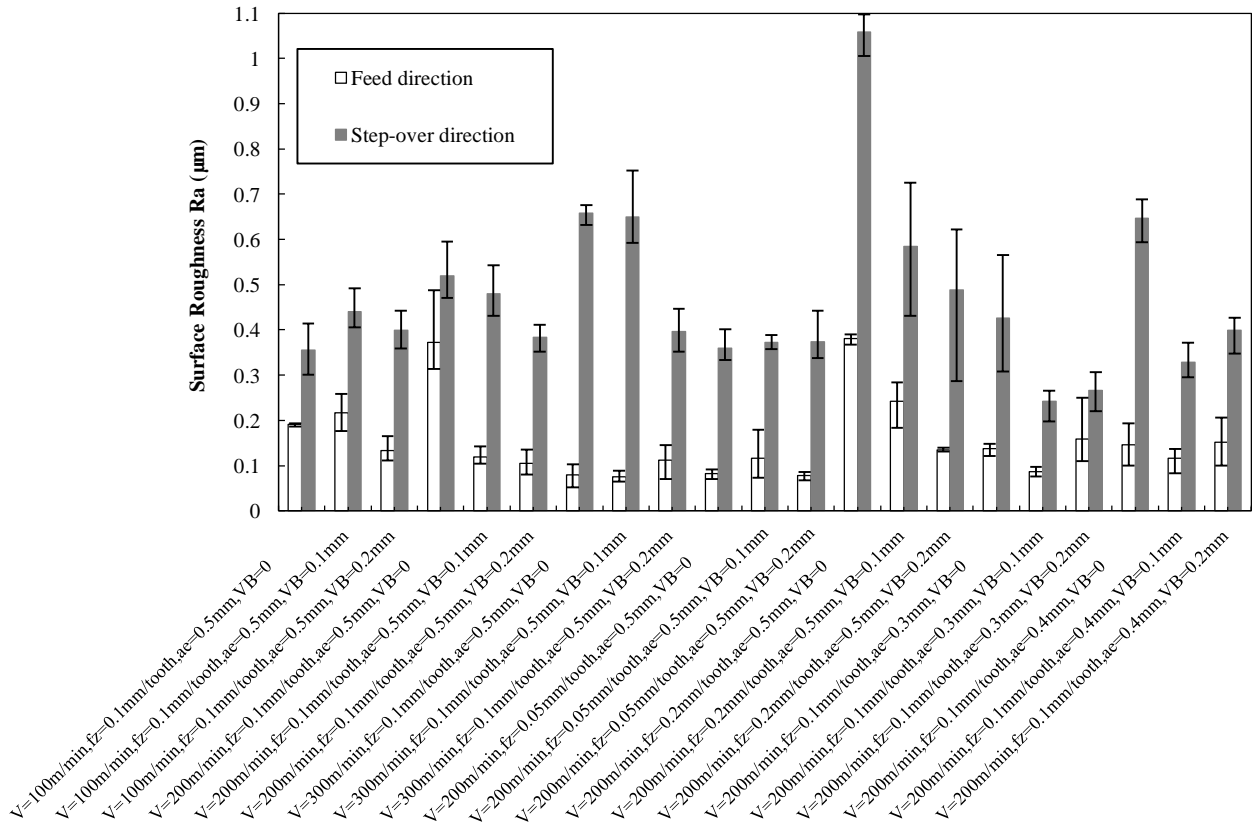


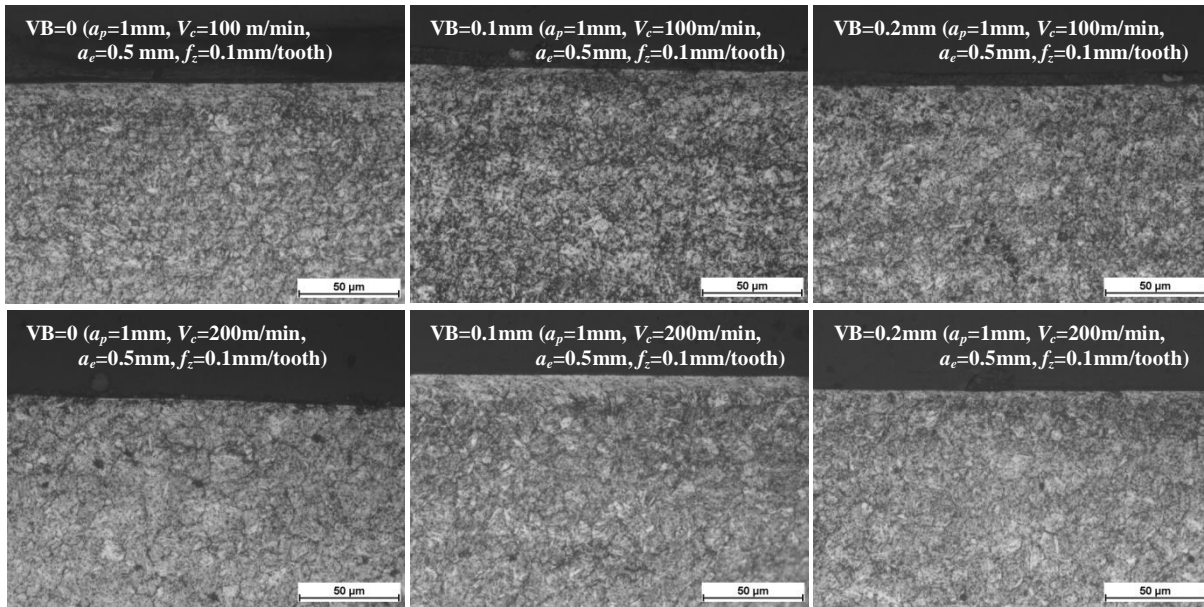
Fig. 5.3 Average, maximum, and minimum surface roughness ( $R_a$ ) in the feed and the step-over directions.

It shows that surface roughness in the step-over direction is much higher than that in the feed direction under all the milling conditions in Table 5.1. Seventeen out of the twenty-one milled surfaces have surface roughness value of  $R_a < 0.2 \mu\text{m}$  in the feed direction and the remaining four samples are between  $0.2 \mu\text{m}$  to  $0.4 \mu\text{m}$ . Surface roughness reduces or at least does not change dramatically when tool wear increases (at cutting conditions 2, 3, 4 and 6 in Table 5.1). For  $VB = 0$  and  $VB = 0.1 \text{ mm}$ , surface roughness in the step-over direction generally increases with cutting speed at cutting conditions 1, 2 and 3, while  $R_a$  is almost same at  $VB = 0.2 \text{ mm}$  under the three different cutting speeds. When increasing the feed per tooth from minimum to maximum (at cutting conditions 2, 4 and 5), surface roughness in the step-over direction was also found to increase at all three levels of tool flank wear. However, the increased tool wear (e.g. large  $VB$ ) did not necessarily produce a rougher surface in both step-over direction and feed direction.

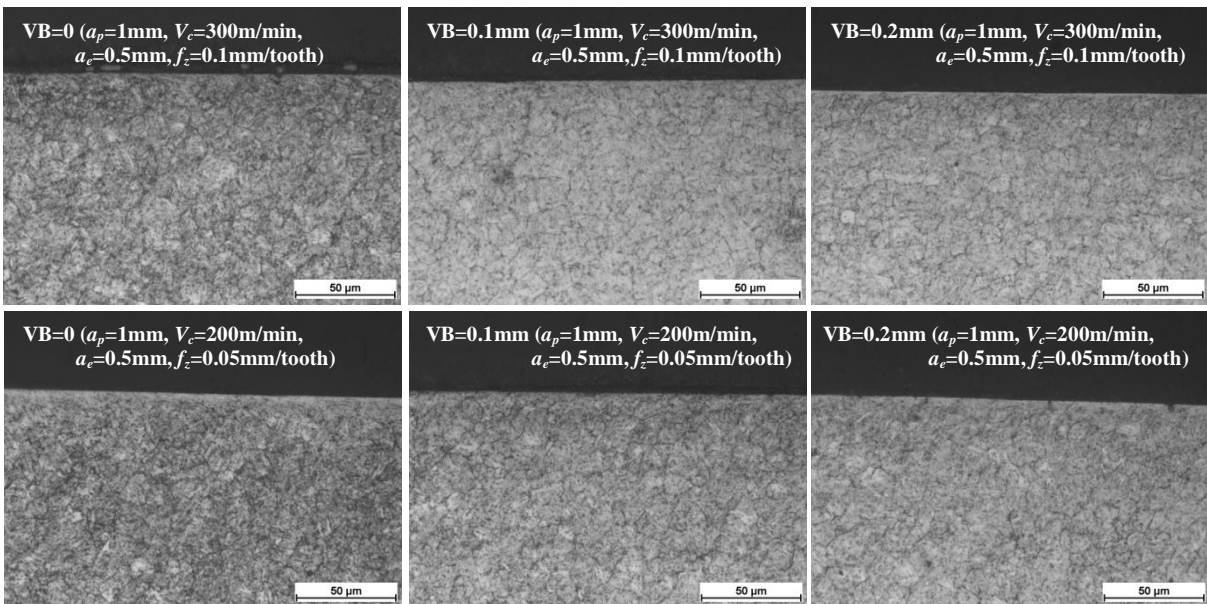
#### 5.3.4.2. Subsurface microstructure

Although machining chips carry away the majority of heat generation in dry hard milling, a certain percentage of heat still dissipates into the machined surface. If the maximum temperature of the machined surface is below the austenitizing temperature, it would not be possible for the machined surface to form a heat-induced white layer. With higher values of cutting parameters (cutting speed, feed rate, tool flank wear), it is expected that higher temperatures will be produced and more heat will conduct into the workpiece. Thus, it is more likely that phase transformation would happen on the machined surface. Subsurface microstructure of the machined samples was taken using an optical microscope equipped with a CCD camera (NIKON Epiphot 200). However, optical images of the subsurface microstructure of the 21 samples do not show a noticeable white layer (Figure 5.4). The possible reason is that

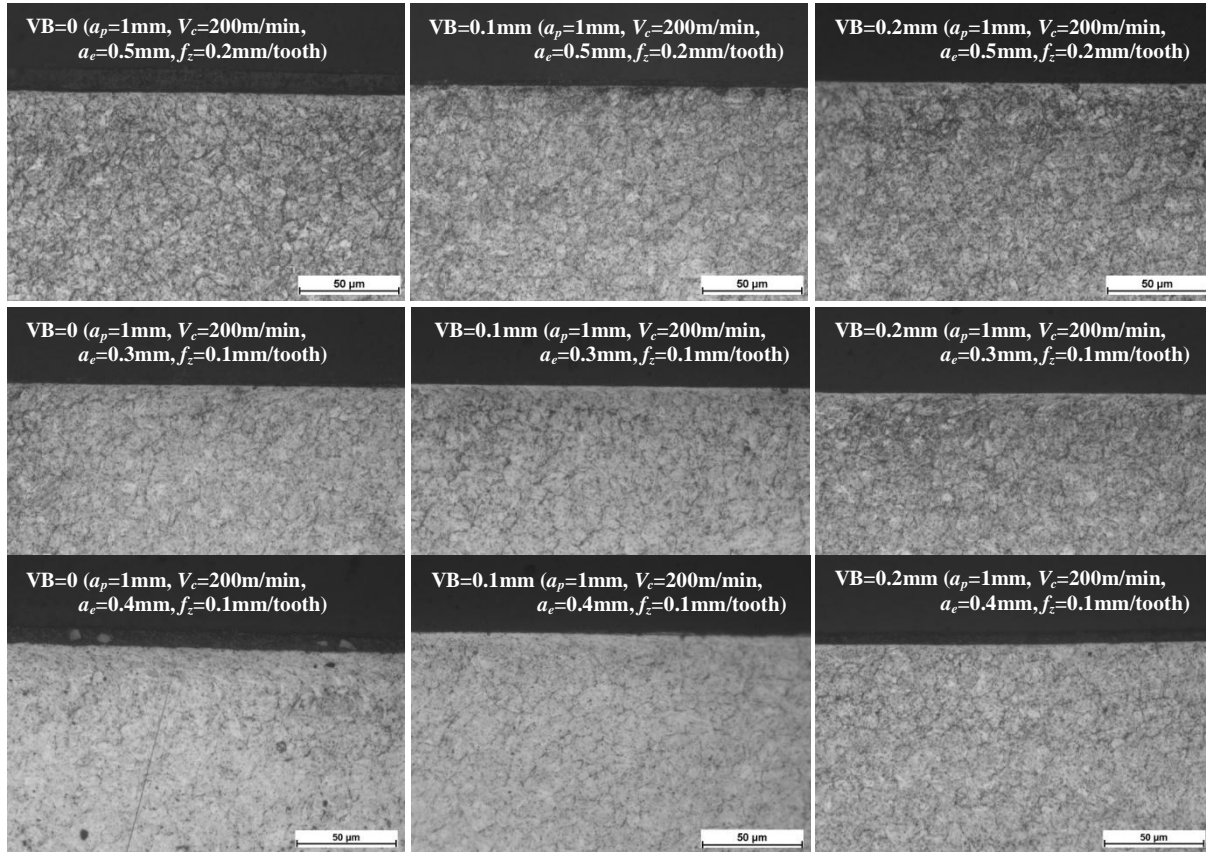
with spindle rotating in milling, the periodic tool/work contact reduces the time of heat dissipation into the machined surface. Compared with the continuous tool/work contact in turning and grinding processes, milling would have less chance to induce thermal white layer at the same level of tool wear. This may explain why white layer or heat affected zones (HAZ) can be generated much more easily in turning and grinding processes.



(a) sample #1 – sample #6



(b) sample #7 – sample #12



(c) sample #13 – sample #21

Fig. 5.4 Optical images of subsurface microstructure.

#### 5.3.4.3. Residual stresses

Residual stresses were measured using 4-axis Bruker D8 machine. X-rays with  $\lambda = 0.1790$  nm wavelength were generated applying 35 mA and 40 kV power to X-ray tube with cobalt source.  $\{2\ 1\ 1\}$  crystallographic planes corresponding to  $2\theta = 99.7^\circ$  were utilized to measure residual strains and then residual stresses were calculated by the  $\sin^2\psi$  technique.

Surface residual stress:

Figure 5.5 shows surface residual stresses are compressive in both feed and step-over directions. Furthermore, the residual stresses in the step-over direction are more compressive than in the feed direction for the majority of machined samples. In most cases, the machined surfaces have the maximum compressive residual stresses due to the work hardening effect. This observation is consistent with the maximum microhardness values at the surface.

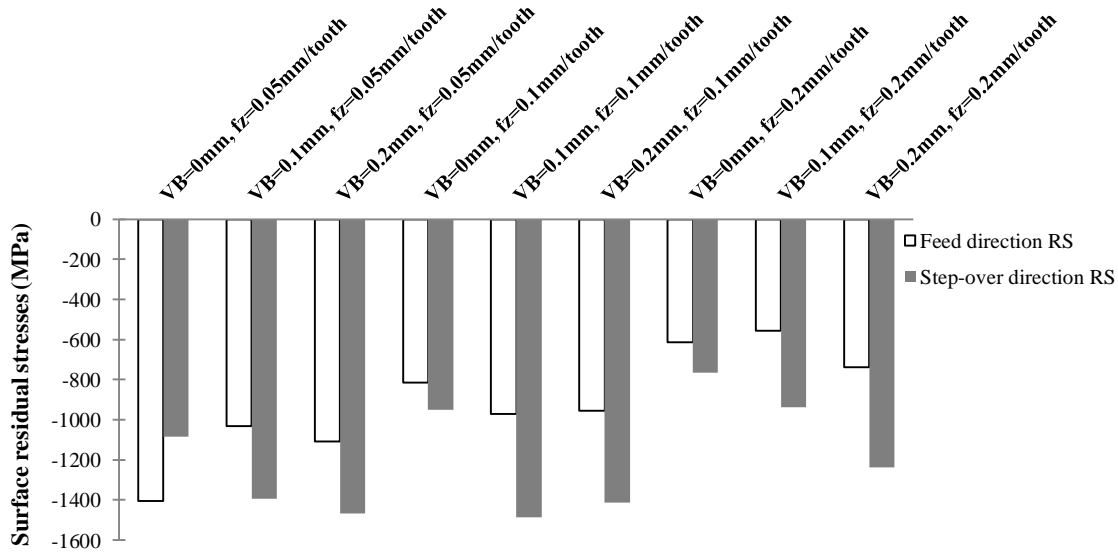


Fig. 5.5 Residual stresses at the machined surface.

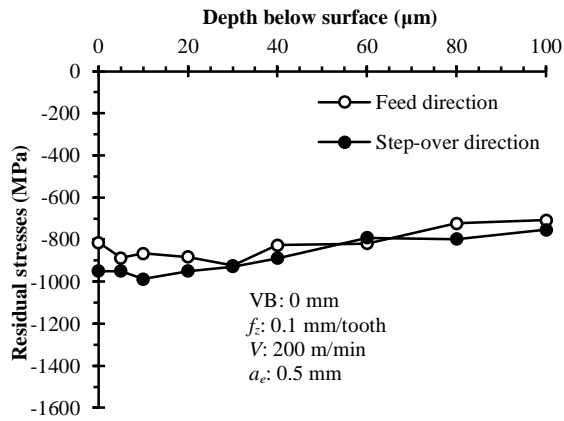
In the feed direction, it is clear that the increased feed resulted in less compressive residual stresses. At  $f_z = 0.05$  mm/tooth, the compressive residual stresses are all greater in magnitude than -1000 MPa (sample #10 ~ #12); at  $f_z = 0.1$  mm/tooth, the compressive residual stresses are in the range of -800 ~ -1000 MPa (sample #4 ~ #6); at the maximum  $f_z = 0.2$  mm/tooth, surface compressive residual stresses are all less than -750 MPa in magnitude (sample #13 ~ #15). This conclusion holds true for each tool flank wear level, which can be seen by a comparison between the samples milled by tools with the same tool wear values. For example,

samples #10, #4 and #13 were milled by fresh tools ( $VB = 0$ ) but with different feeds. The surface residual stresses became less compressive with increased feed in the three samples.

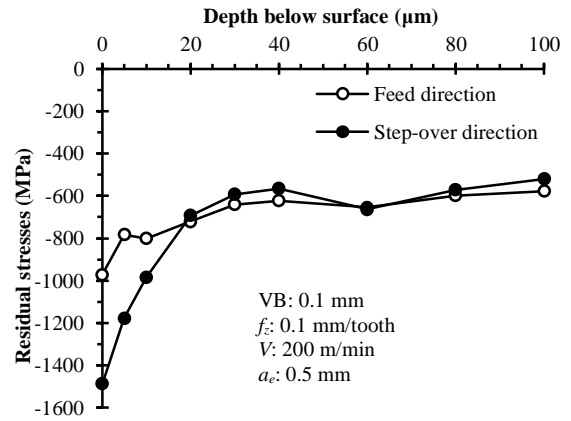
In the step-over direction, the samples tend to produce more compressive residual stresses with increased VB values at each feed level, except for sample #5. When comparing samples #10 ~ #12 and samples #13 ~ #15, the trend of increased compressive residual stresses can be easily observed. As for the effect of feed at the same flank wear level, increasing feed results in less compressive residual stress (samples #10, #4, #13 and samples #12, #6, #15) which is consistent with the observation in the feed direction.

Subsurface residual stress:

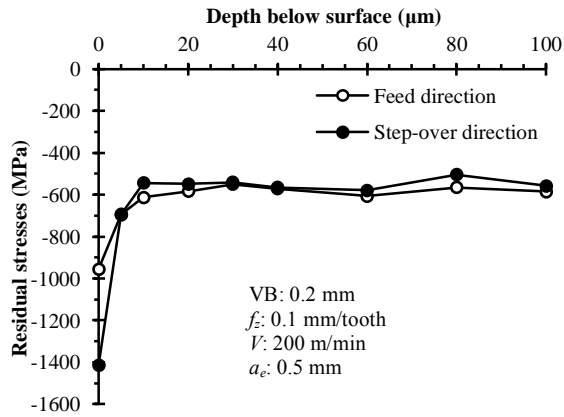
Figure 5.6 (a - i) shows the residual stress profiles in the subsurface, the compressive residual stresses in both feed and step-over directions share similar profile characteristics. Residual stress in the step-over direction is more compressive in the near subsurface than in the feed direction. At increased depth in the subsurface, residual stress becomes less compressive and the gradient becomes small between consecutive readings, approaching  $-500 \sim -800$  MPa at the depth of around  $100 \mu\text{m}$  below the machined surface. It is expected that the residual stress becomes much less compressive in the deeper subsurface.



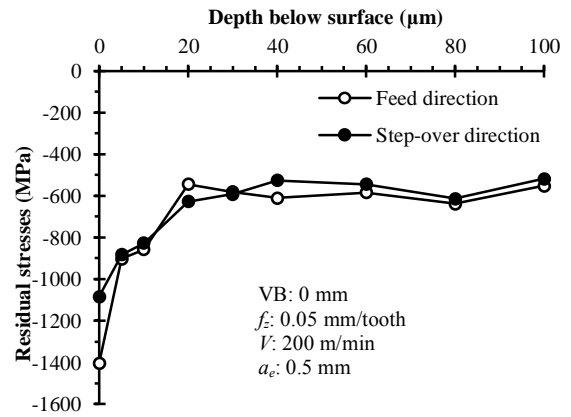
(a) sample #4



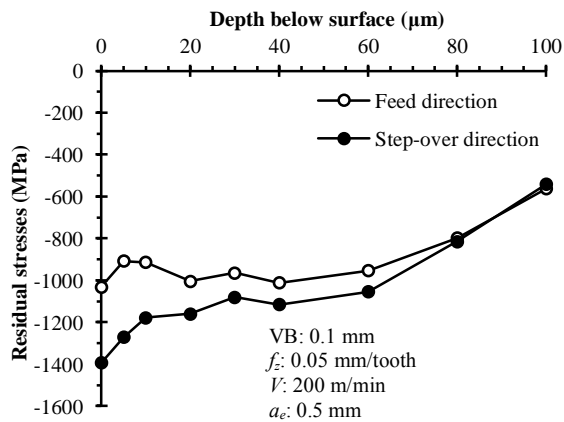
(b) sample #5



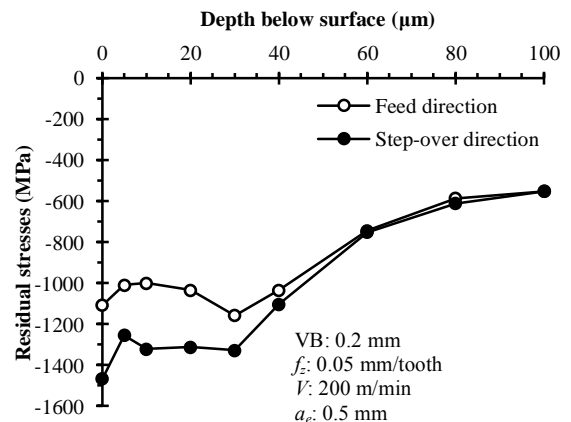
(c) sample #6



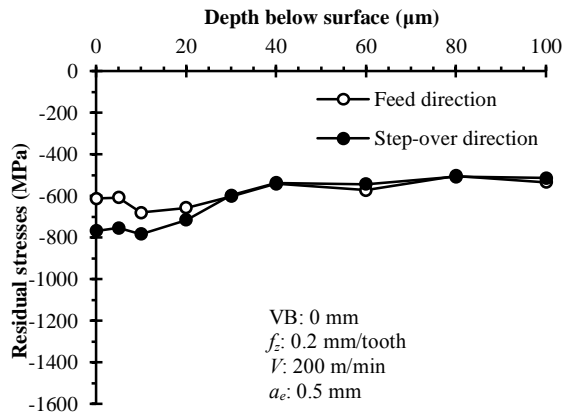
(d) sample #10



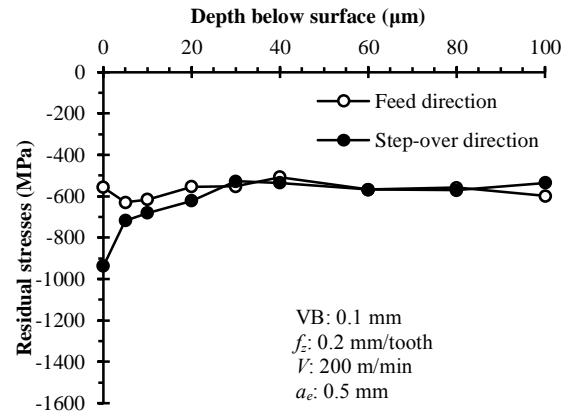
(e) sample #11



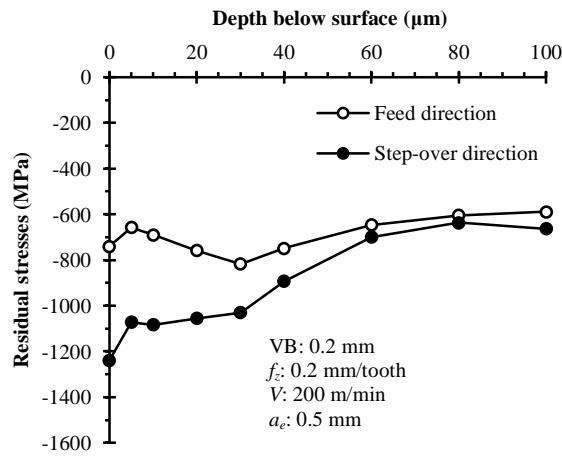
(f) sample #12



(g) sample #13



(h) sample #14



(i) sample #15

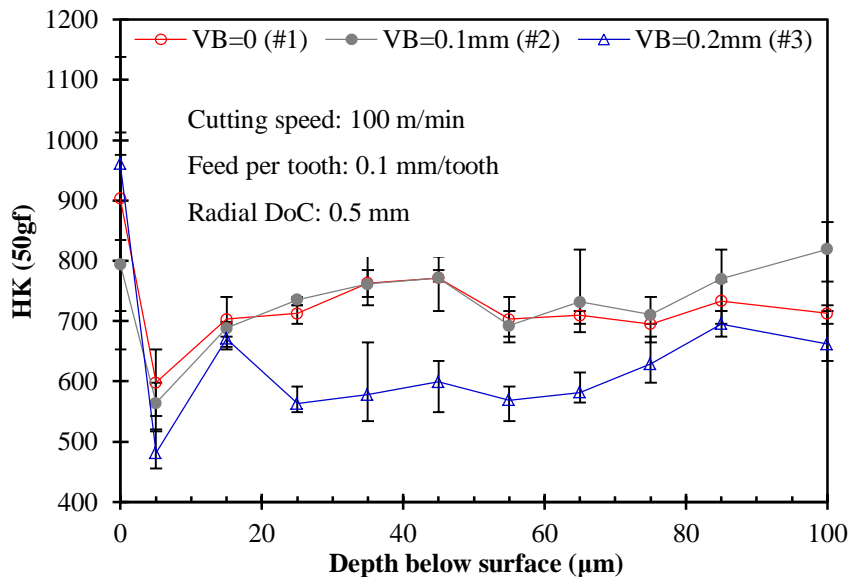
Fig. 5.6 Residual stresses distribution profiles.

#### 5.3.4.4. Surface and subsurface microhardness

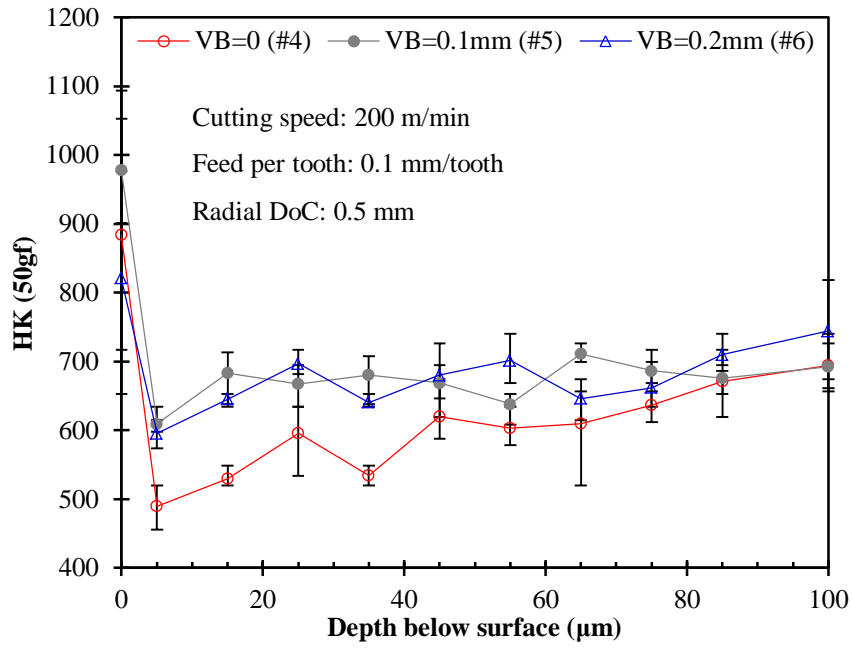
Microhardness on the surface and in the subsurface was measured at a load of 50 g for 10s using a Knoop indenter. Microhardness of the machined surfaces was measured in two orientations: parallel and perpendicular to the feed direction. Three measurements were performed in each direction and an average of 6 measured values was used as surface microhardness. In the subsurface, microhardness measurements were taken at about 10  $\mu\text{m}$

intervals between successive readings up to 100  $\mu\text{m}$ . Similarly, 3 measurements were made at the same depths in the subsurface. Figure 5.7 (a ~ g) illustrates the microhardness profiles for all 7 different cutting conditions.

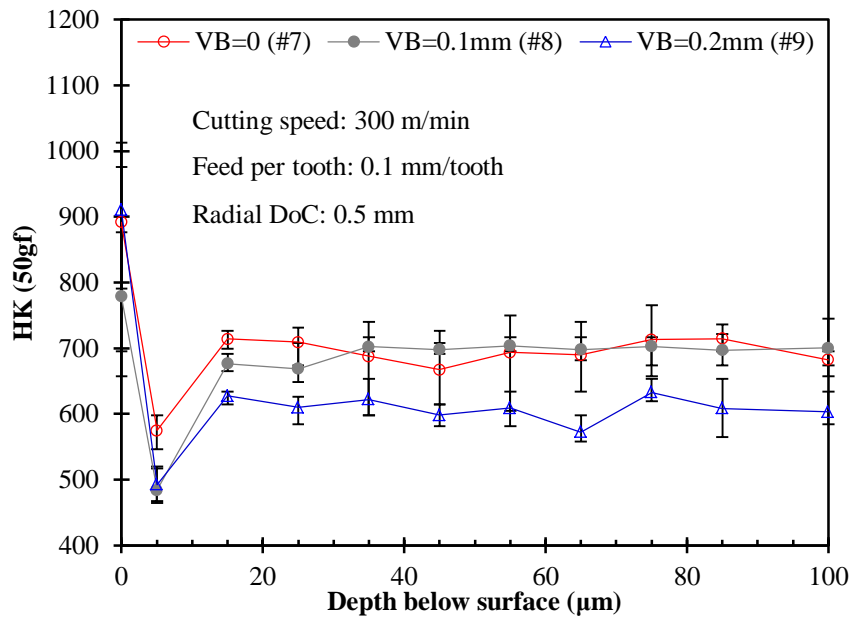
The surface material experienced both thermal and mechanical loading in milling. Surface properties depend on the additive effects of the two loadings. As discussed above, thermal loading in milling has the characteristics of discontinuity and short duration, while mechanical loading would be the predominant factor determining the surface properties. Based on the measured microhardness data for all the samples, the work-hardening effect on the machined surface may be dominant since much higher microhardness occurred on the surface than the subsurface. Alternatively, low microhardness at approximately 5  $\mu\text{m}$  into the subsurface is more likely induced by the edge effect of micro-indenter rather than thermal effect. The detailed mechanism of the measured low hardness was explained in [21].



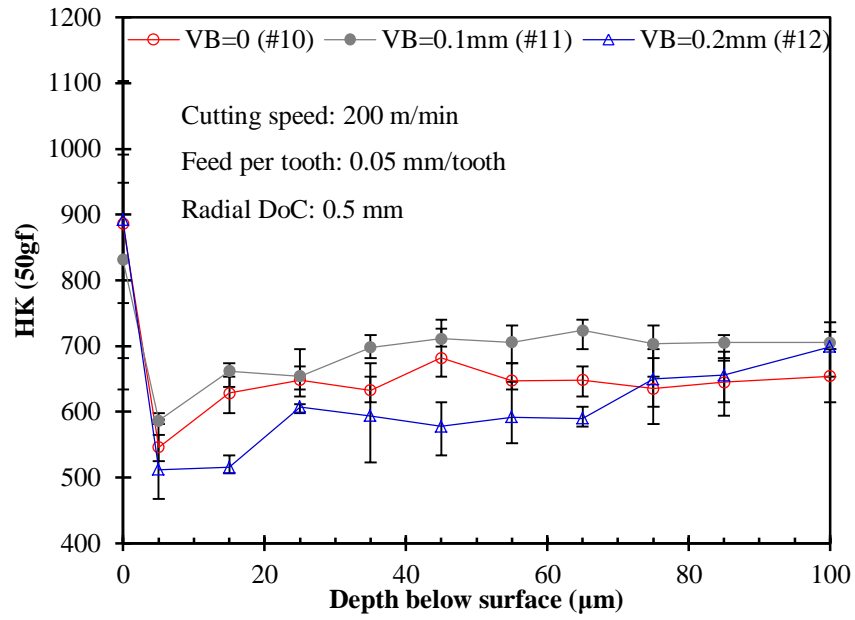
(a) Microhardness profile for samples 1 ~ 3



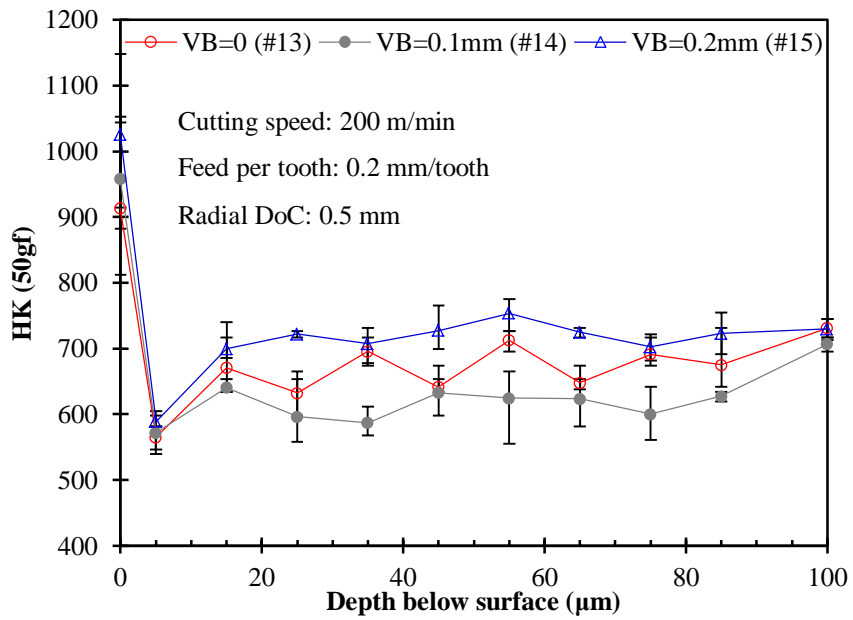
(b) Microhardness profile for samples 4 ~ 6



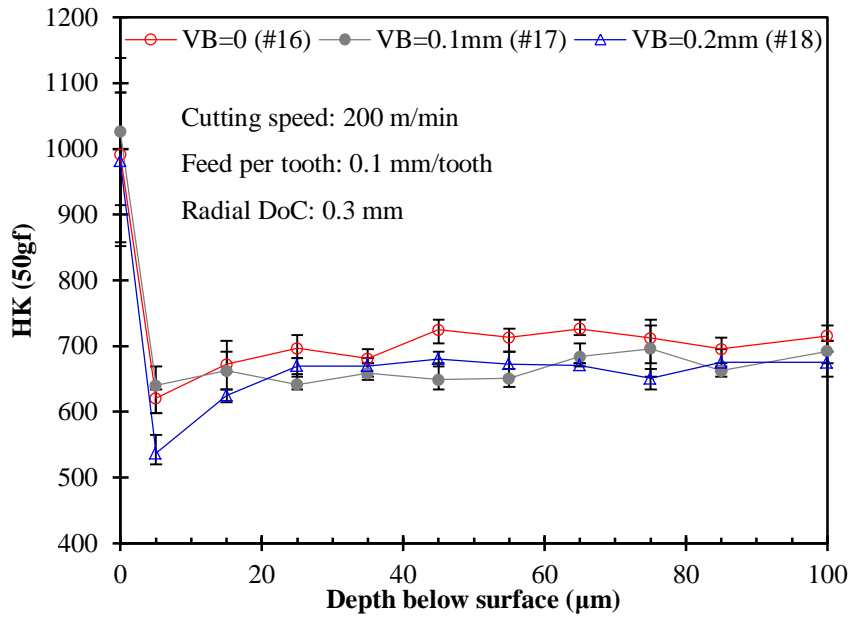
(c) Microhardness profile for samples 7 ~ 9



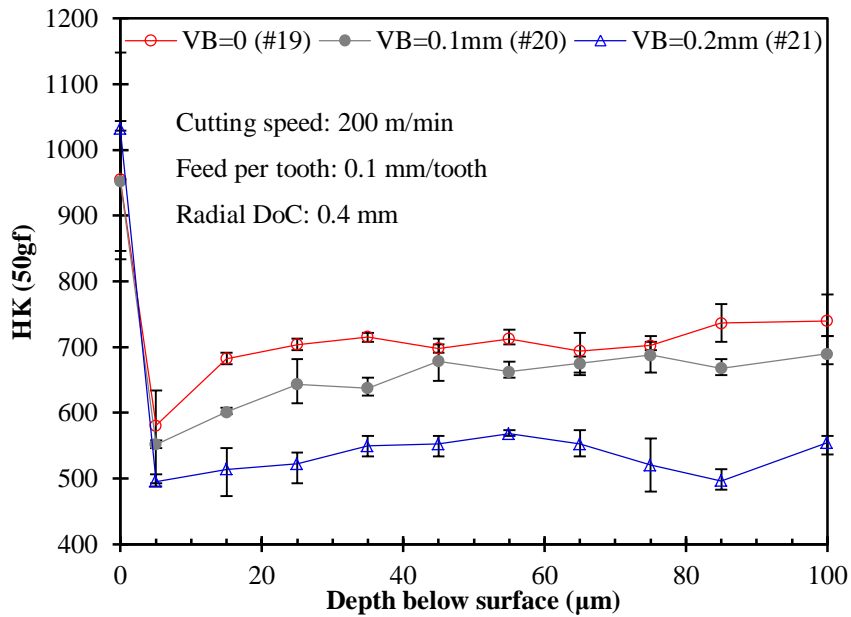
(d) Microhardness profile for samples 10 ~ 12



(e) Microhardness profile for samples 13 ~ 15



(f) Microhardness profile for samples 16 ~ 18



(g) Microhardness profile for samples 19 ~ 21

Fig. 5.7 Microhardness profiles in the subsurface.

Under cutting conditions 1, 3, 4 and 7 in Table 5.1, microhardness values for  $VB = 0.2$  mm into the subsurface are generally lower than  $VB = 0$  and  $VB = 0.1$  mm. This indicates that a larger tool/work friction occurs due to the increased tool flank wear, producing more thermal loading which leads to more softening effect in the subsurface.

#### 5.4. Four-point bending fatigue test

##### 5.4.1. Fatigue sample preparation

Four-point bending tests were performed to investigate the fatigue life evolution of the machined samples with tool flank wear.

Five H13 rectangular blocks (sample #F1 - sample #F5) were hard milled by the cutting tools with five wear levels:  $VB = 0, 0.05$  mm,  $0.1$  mm,  $0.15$  mm, and  $0.20$  mm, respectively. Before fatigue testing, the samples' edges were polished using a 600-grit sandpaper to eliminate the effects of burrs and sharp-edges on fatigue life.

To study the effect of tool flank wear on fatigue life of machined samples, Table 5.2 lists the machining parameters. The tool holder and inserts are same as those to prepare samples for surface integrity characterization.

Table 5.2 End milling parameters to prepare fatigue samples.

Cutting speed (m/min)	Axial depth-of-cut (mm)	Feed rate (mm/min)	Radial depth-of-cut (mm)
250	1	796	0.5

#### 5.4.2. Fatigue testing setup

Four-point bending fatigue tests were run at room temperature on a MTS 810 test system (Figure 5.8) with the maximum load capacity of 225 kN. The MTS 810 test system consists of a servo-hydraulic fatigue testing machine, a Flextest SE digital controller, and the MultiPurpose TestWare Software (MPT). The test sample sits on the loading fixture which is bolted to the oscillating piston. The oscillating piston moves up and down with the loading fixture at a certain frequency. The supporting fixture is fixed at the supporting ends to keep the loading direction constant.

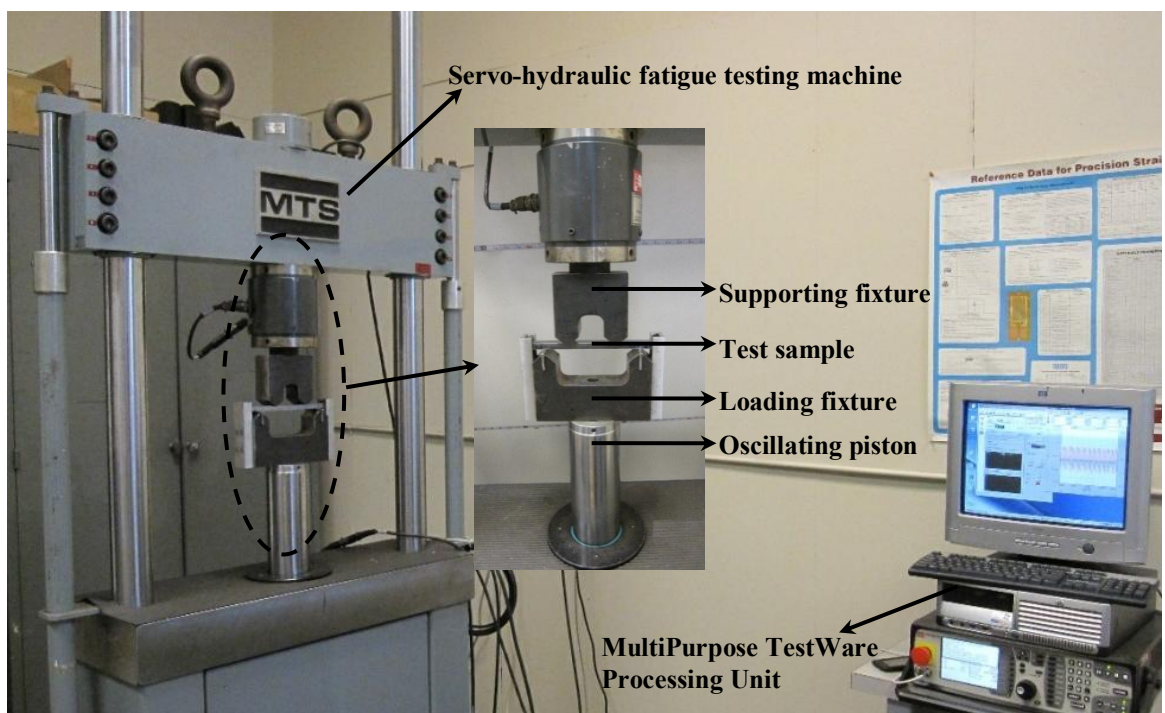


Fig. 5.8 MTS four-point bending fatigue testing system.

A cyclic load was applied at a frequency of 10 Hz and with a sinusoidal waveform. The nominal stress can be calculated by the beam theory:

$$\sigma = \frac{3Pa}{wh^2} \quad (5.1)$$

where sample width  $w = 20.32$  mm, height  $h = 10.7$  mm,  $a = \frac{1}{2} b = 38.1$  mm (Figure 5.9).

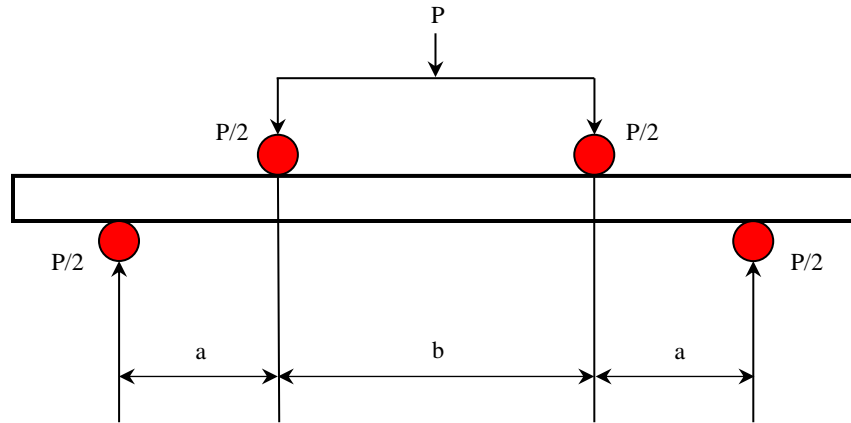


Fig. 5.9 Four-point bending fatigue testing configuration.

The maximum tensile stress  $\sigma_{\max}$  at the bottom of test samples was set to be 50% of the ultimate tensile strength of AISI H13. As shown in Figure 5.3, the load-span  $b$  was set to 76.2 mm, support-span =  $2a + b = 152.4$  mm, and the stress amplitude ratio  $R = 0.1$ . The fatigue testing conditions are listed in Table 5.3.

Table 5.3 Four-point bending fatigue testing condition.

Max. stress $\sigma_{\max}$ (MPa)	900
Min. stress $\sigma_{\min}$ (MPa)	90
Stress ratio $R$ ( $\sigma_{\min}/\sigma_{\max}$ )	0.1
Mean stress $\sigma_m = (\sigma_{\min} + \sigma_{\max})/2$ (MPa)	495
Stress amplitude $\sigma_a = (\sigma_{\max} - \sigma_{\min})/2$ (MPa)	405
Frequency (Hz)	10

### 5.4.3. Fatigue performance

#### 5.4.3.1. Four-point bending fatigue testing

The fatigue life variation versus tool wear is shown in Figure 5.10. It shows that fatigue life of the sample milled by fresh tool ( $VB = 0$ ) exhibited the longest number of cycles to failure ( $N \approx 1.23 \times 10^6$  cycles) which is expected since a fresh tool should have the best performance as a sharp cutting edge produces better surface integrity which delays fatigue crack initiation. With the increased tool wear to  $VB = 0.05$  mm, fatigue life dropped slightly down to  $N \approx 1.16 \times 10^6$  cycles. When the tool wear developed from  $VB = 0.05$  mm to  $VB = 0.10$  mm, a sharp decrease in fatigue life occurred. While the tool wear value reached  $VB = 0.15$  mm, the machined sample had a very slightly increased fatigue life compared with the sample machined by a tool of  $VB = 0.10$  mm. However, the 5th sample which was machined by worn tool with flank wear of 0.20 mm fatigued at very early life of  $N \approx 0.044 \times 10^6$  cycles. The general trend is clear that a worn tool reduces fatigue life, and the larger the tool wear, the shorter the fatigue life. It suggests that worn out tools need to be replaced with fresh tools after used for a certain cutting time.

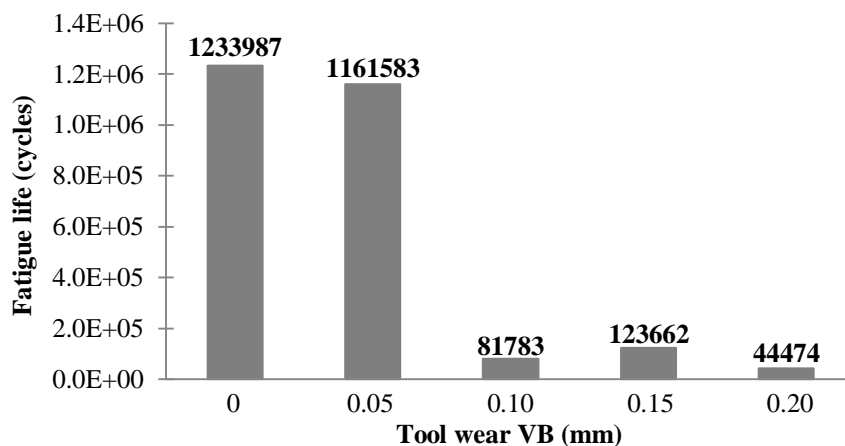


Fig. 5.10 Fatigue life vs. tool wear.

It is very common in industry to cut multiple parts using the same tool for reducing tooling cost. It should be realized that component life will vary with tool wear. The key concern is that component life needs to be within a specified range under the deterioration of tool wear. It is extremely critical for manufacturers in mass production to be able to guarantee that machined parts would have identical performance (e.g. fatigue life), or at least within a specified variation. Therefore, fatigue life management under the progression of tool wear is necessary for controlling fatigue performance of machined components to meet customers' needs.

#### 5.4.3.2. Endurance limit estimation

In  $S-N$  diagrams of steels, a knee point usually occurs and its corresponding  $\sigma$  (stress) amplitude is termed endurance limit,  $S_e$ . Endurance limit  $S_e$  is used to characterize the amplitude of cyclic stress that can be applied to the material without causing fatigue failure. For fatigue analysis, an estimation of endurance limit is needed for steel samples. Generally, the endurance limit of the controlled laboratory specimen,  $S_e'$ , is determined first and then it can be modified by multiplicative factors by incorporating the effects of surface finish, sample size, loading mode, temperature, and miscellaneous items. The endurance limit  $S_e$  of the machined AISI H13 samples for four-point bending fatigue testing is estimated below.

Since the tensile strength of AISI H13,  $S_{ut}$ , is 1800 MPa, the endurance limit of the controlled laboratory specimen  $S_e'$  is estimated as  $S_e' = 740$  MPa based on rule of thumb:

$$S_e' = \begin{cases} 0.5 S_{ut}, & \text{when } S_{ut} \leq 1460 \text{ MPa} \\ 740 \text{ MPa}, & \text{when } S_{ut} > 1460 \text{ MPa} \end{cases} \quad (5.2)$$

Then, modifying factors  $K_a, K_b, K_c, K_d, K_e, K_f$  are applied to compensate the difference of lab controlled samples and the machined samples [22], see Table 5.4.

Table 5.4 Modifying factors of endurance limit.

Surface factor $K_a = aS_{ut}^b$	0.619 ( $a = 4.51, b = -0.265$ )
Size factor $K_b = 1.24d_e^{-0.107}$	0.95 ( $d_e = 0.808(\text{height} \times \text{width})^{0.5}$ )
Loading factor $K_c$	1 (bending mode)
Temperature factor $K_d$	1 (room temperature)
Reliability factor $K_e = 1 - 0.08 \cdot z_\alpha$	1 (reliability=50%, $z_\alpha=0$ ) 0.814 (reliability=99%, $z_\alpha=2.326$ )
Miscellaneous factor $K_f$	1

From the Marin equation [23],

$$S_e = K_a K_b K_c K_d K_e K_f S_e' \quad (5.3)$$

By substituting all the values from (5.2) and Table 5.4 into (5.3), the endurance limit can be expressed as:

$$S_e = 435.615 \times (1 - 0.08 \cdot z_\alpha)$$

where the endurance limit  $S_e$  is a function of reliability factor  $K_e$  and it varies with the transformation variate  $z_\alpha$  determined by the reliability. Let's consider two cases:

(i) Reliability = 50% ( $z_\alpha = 0$ )

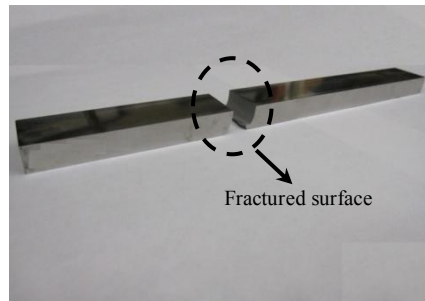
For 50% testing reliability ( $z_\alpha = 0$ ),  $S_e = 435.615 \text{ MPa} > \sigma_a = 405 \text{ MPa}$ , which means the amplitude of applied cyclic stress is below the estimated endurance limit. It is expected that the fatigue life will be at least  $10^6$  cycles or even longer.

(ii) Reliability = 99% ( $z_\alpha = 2.326$ )

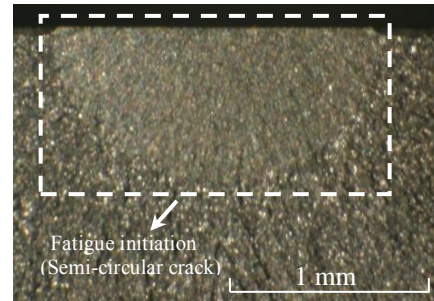
For 99% testing reliability ( $z_\alpha = 2.326$ ),  $S_e = 354.556 \text{ MPa} < \sigma_a = 405 \text{ MPa}$ , which means the amplitude of applied cyclic stress is above the estimated endurance limit and the fatigue life could be less than  $10^6$  cycles.

#### 5.4.3.3. Fatigued sample characterization

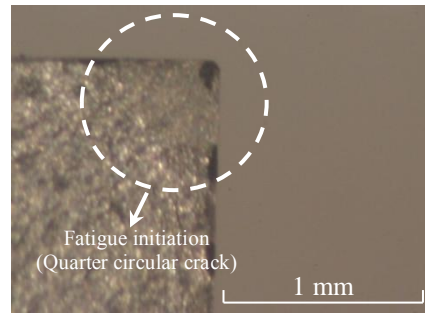
The cross-sections of the fatigued surfaces were examined under optical microscope. Representative images of the cross-section of fractured surface are shown in Figure 5.11. From Figure 5.11, typical semi-circular cracks on the fatigued surface were observed and they all initiated from the bottom surface of the test sample where the maximum tensile stress exists. However, the cracks did not always locate at the same position along the edge of the fractured surface. For samples #F2 and #F5, quarter circular cracks were found at the corner. Theoretically, the distribution of possible crack initiation locations in the sample can be random, depending on where the “weakest” point (void, inclusion, surface flaw, etc.) exists. In addition to surface integrity, it is also noticed that edge finishing such as burrs also affect the random life of machined samples. The tool steel’s characteristic of brittleness strongly influences crack initiation and thus also brings randomness to fatigue life.



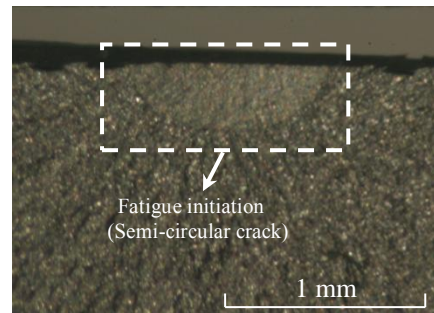
(a) Fatigued sample



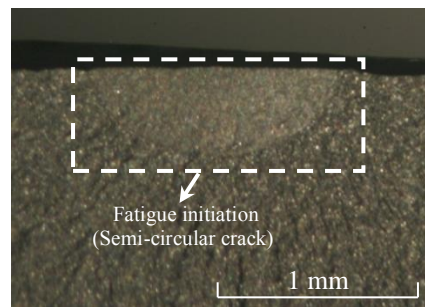
(b) Fatigue crack on fractured surface of sample #F1 (VB = 0)



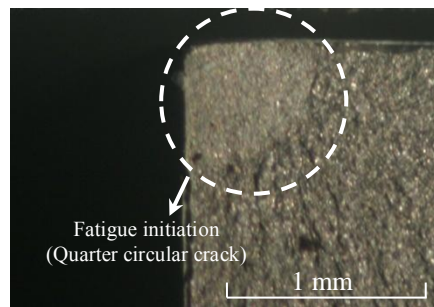
(c) Fatigue crack on fractured surface of sample #F2 (VB = 0.05 mm)



(d) Fatigue crack on fractured surface of sample #F3 (VB = 0.10 mm)



(e) Fatigue crack on fractured surface of sample #F4 (VB = 0.15 mm)



(f) Fatigue crack on fractured surface of sample #F5 (VB = 0.20 mm)

Fig. 5.11 Cross-section of fatigued samples.

## 5.5. Conclusions

The major results of this study may be summarized as follows:

- Surface roughness in the step-over direction is much higher than that in the feed direction under all the milling conditions. Increased tool wear does not necessarily produce a rougher surface in both directions. With increased feed per tooth, surface roughness in the step-over direction is found to be increasing at all 3 levels of tool flank wear.
- No obvious white layer or heat affected zones (HAZ) is observed in the optical images of the subsurface microstructure of the 21 milled samples. A possible explanation is that the characteristic of periodic tool/work contact in milling reduces the time of heat dissipation into the machined surface compared to turning and grinding.
- All the residual stresses measured are compressive. Residual stresses in both directions share similar profile characteristics. Surface residual stresses in the step-over direction are more compressive than in the feed direction. With increased tool flank wear, residual stresses in the step-over direction are more compressive. Increased feed per tooth resulted in less compressive residual stresses in the feed direction at each tool flank wear level.
- Much higher microhardness occurred on the surface than the subsurface which gives evidence of work-hardening effect on the machined surface.
- Endurance limit estimation using the Marin equation demonstrated that endurance limit  $S_e$  is a function of reliability factor  $K_e$  and it varies with the transformation

variate  $z\alpha$  which is determined by the testing reliability. Endurance limit estimation can be used to qualitatively evaluate if the possible fatigue life of testing sample can reach a run-out level ( $> 10^6$  cycles) by comparing estimated  $S_e$  and stress amplitude  $\sigma_a$ .

- Four-point bending fatigue tests on AISI H13 samples machined by tools with different flank wears show that the fresh tool produced a sample with longest fatigue life and number of load cycles generally decreased when increasing cutting tool flank wear. It is a key issue for manufacturers to confidently control the variation of fatigue life within an acceptable range in order to meet customers' needs.
- To some extent, the reliability of fatigue testing discussed above is crucial and provides helpful information for fatigue testing design and related fatigue analysis. If a sample is machined, the variation of reliability generally varies within a certain range and this variation range can be affected by the uncertainty of fatigue testing facility, sample uniformity, and designers' risk-taking attitude. It is worth a further study on this topic in the future to better understand the uncertainty of fatigue life and manage fatigue performance.

## 5.6. References

- [1] Kannatey-Asibu E, Dornfeld DA. A study of tool wear using statistical analysis of metal-cutting acoustic emission. *Wear* 1982; 76: 247-261.
- [2] Guo YB, Ammula SC. Real-time acoustic emission monitoring for surface damage in hard machining. *International Journal of Machine Tools & Manufacture* 2005; 45: 1622-1627.
- [3] Li W, Singh HM, Salahshoor M, Guo YB. The development of a novel on-line optical

- inspection system for tool conditions in machining processes. Proceedings of the ASME 2010 International Manufacturing Science and Engineering Conference, Erie, Pennsylvania, USA 2010. p. 607-613.
- [4] Zhang S, Guo YB. An experimental and analytical analysis on chip morphology, cutting temperature, oxidation and their relationship in finish hard milling. *International Journal of Machine Tools & Manufacture* 2009; 49: 805-813.
- [5] Guo YB, Li W, Jawahir IS. Surface integrity characterization and prediction in machining of hardened and difficult-to-machine alloys: a state-of-art research review and analysis. *Machining Science and Technology* 2009; 13 (4): 437-470.
- [6] Zhang S, Guo YB. Taguchi method based process space for optimal surface topography by finish hard milling. *ASME Journal of Manufacturing Science and Engineering* 2009; 131 (051003): 1-9.
- [7] Li W, Guo YB, Barkey ME, Guo C, Liu ZQ. Surface integrity and fatigue strength of hard milled surfaces. Proceedings of the ASME 2011 International Manufacturing Science and Engineering Conference, Corvallis, Oregon, USA 2011. p. 199-206.
- [8] Elbestawi MA, Chen L, Becze CE, El-Wardany TI. High-speed milling of dies and molds in their hardened state. *Annals of the CIRP* 1997; 46 (1): 57-62.
- [9] Axinte DA, Dewes RC. Surface integrity of hot work tool steel after high speed milling-experimental data and empirical models. *Journal of Materials Processing Technology* 2002; 127: 325-335.
- [10] Ghani JA, Choudhury IA, Hassan HH. Application of Taguchi method in the optimization of end milling parameters. *Journal of Materials Processing Technology* 2004; 145 (1): 84-92.
- [11] Koster WP, Field M. Effects of machining variables on the surface and structural integrity of titanium. Proceedings of the North American Manufacturing Research Conference, SME 1973. p. 67-87.
- [12] Thomas WN. Effect of scratches and of various workshop finishes upon the fatigue strength of steel. *Engineering* 1923; 116: 449-485.
- [13] Noll GC, Erickson GC. Allowable stresses for steel members of finite life. Proceedings of the Society of Experts for Stress Analysis 1948; 5 (2): 132-143.
- [14] Fluck PG. The influence of surface roughness on the fatigue life and scatter of test results of two steels. Proceedings of American Society for Testing Materials 1951; 51: 584-592.
- [15] Koster W. Effect of residual stress on fatigue of structural alloys. Proceedings of the Third International Conference, ASM International, Indianapolis, Indiana, USA 1991. p.

1-9.

- [16] Taylor D, Clancy OM. The fatigue performance of machined surfaces. *Fatigue Fract. Eng. Mater. Struct.* 1991; 14: 329-336.
- [17] Brinksmeier E, Cammett JT, Konig W, Leskovar P, Peters J, Tönshoff HK. Residual stresses-measurement and causes in machining processes. *Annals of the CIRP* 1982; 31 (2): 491-510.
- [18] Matsumoto Y, Magda D, Hoepfner DW, Kim TY. Effect of machining processes on the fatigue strength of hardened AISI 4340 steel. *ASME J. Eng. Ind.* 1991; 113: 154-159.
- [19] Guo YB, Warren AW, Hashimoto F. The basic relationships between residual stress, white layer, and fatigue life of hard turned and ground surfaces in rolling contact. *CIRP J. Manuf. Sci. Tech.* 2010; 2/2: 129-134.
- [20] Hashimoto F, Guo YB, Warren AW. Surface integrity difference between hard turned and ground surfaces and its impact on fatigue life. *Annals of the CIRP.* 2006; 55/1: 81-84.
- [21] Warren AW, Guo YB. On the clarification of surface hardening mechanisms by hard turning and grinding. *Trans. NAMRI/SME* 2006; 34: 309-316.
- [22] Budynas R, Nisbett J. *Shigley's Mechanical Engineering Design.* McGraw-Hill, New York 2008.
- [23] Marin J. *Mechanical Behavior of Engineering Materials.* Prentice-Hall, New Jersey 1962.

## CHAPTER 6

### A FUNDAMENTAL STUDY OF TOOL WEAR EFFECT ON SURFACE INTEGRITY AND FATIGUE LIFE OF NICKEL-BASED SUPERALLOY BY END MILLING

#### Abstract

Inconel 718 is known to be among the most difficult-to-cut materials due to its high strength even at high temperatures, low thermal conductivity, and especially rapid work hardening. Machining Inconel 718 is a challenging task since cutting tool wear adversely affects surface integrity and, therefore, product performance of machined components. In this paper, the effect of tool wear on surface integrity and its impact on fatigue performance of Inconel 718 alloy ( $45 \pm 1$  HRC) by end milling using PVD coated tools are studied. The evolutions of surface integrity including surface roughness, microstructure, and microhardness were characterized at three levels of tool flank wear ( $VB = 0, 0.1 \text{ mm}, 0.2 \text{ mm}$ ). At each level of tool flank wear, the effects of cutting speed, feed, and radial depth-of-cut on surface integrity were investigated respectively. End milling can produce surface finish between  $0.1 \text{ }\mu\text{m}$  and  $0.3 \text{ }\mu\text{m}$  under most of the conditions. Roughness is generally higher in step-over direction than feed direction. No obvious white layer is observed in subsurface microstructure. The machined surface is significantly work-hardened due to the dominant mechanical loading. Four-point bending fatigue test shows that none of the milled samples failed within four million cycles. Fatigue endurance limits of the machined samples at different reliability levels were calculated and correlated with the experimentally determined fatigue life.

## 6.1. Introduction

The Inconel family of alloys was first developed in 1940s to support the development of jet engines for aerospace applications. They are well suited for service in extreme conditions due to their high oxidation and corrosion resistance. In particular, they are usually employed in the hot sections of gas turbines, jet motors, rocket engines and spacecraft since they are more creep-resistant than steels after precipitation hardening and thus retain strength over a wide temperature range. Inconel 718 is one of the most commonly used nickel-based alloys in aerospace industry. It is known to be among the most difficult-to-cut materials due to its high strength even at high temperatures, low thermal conductivity, and especially rapid work hardening.

Tool wear is an unavoidable and complicated phenomenon occurring in machining process. When a tool has been used for cutting various parts, a decision must be made that the current worn tool should be either replaced before the next cut or used continuously. When tool wear reaches a certain level, the most conservative way for ensuring machined components with acceptable surface integrity in subsequent cutting is to replace the worn tool with a fresh one. However, this will obviously increase manufacturing cost and reduce production efficiency since more tools will be consumed and more time on replacement will be spent. Undoubtedly, a considerable amount of manufacturing cost has been contributed by cutting tools. Tool wear or tool failure is considered to be a critical factor that determines the machining economy since it is closely related to tool life and thus the production cost.

Basically, two main types of tool wear will occur when machining for a certain time: flank wear (at tool/work interface) and crater wear (at tool/chip interface). Generally, crater wear only has relatively less effect on tool performance and thus machined surface integrity unless it causes a cutting edge failure. Therefore, flank wear has always been considered to be the most

important wear mode if surface integrity is concerned. It is of great interests to machining industry to investigate the inherent relationship among tool flank wear, surface integrity, and fatigue performance of machined components.

In this research, the effects of tool flank wear on surface integrity and fatigue life of components by end milling of Inconel 718 was studied. The variation of surface integrity at different levels of tool flank wear and diverse combinations of process parameters was investigated. Tool wear values were measured and determined by an on-line optical tool inspection and measurement system. The surface integrity characterized includes surface roughness, subsurface microstructure, surface and subsurface microhardness. The four-point bending fatigue test was used to determine the fatigue life of milled Inconel 718 specimens. By correlating tool flank wear, surface integrity, and fatigue performance of the machined components, a process space with acceptable tool flank wear can be determined for designed fatigue life with controlled variance.

## 6.2. Literature review

The main problems encountered when machining Inconel 718 are short tool life, workpiece surface damage, and subsurface metallurgical damage due to work hardening [1]. Aspinwall et al. [2] conducted a comprehensive series of experiments on the effects of cutter orientation and workpiece angle on machinability in high speed milling of Inconel 718. It was found that compressive surface residual stress was generated when a horizontal upwards cutter orientation was employed, while a tensile stress would be observed by employing a horizontal downwards operation. Krain et al. [3] experimentally evaluated the effects of varying feed rate/chip thickness, immersion radio (radial depth of cut), tool material, and geometry on the tool

life, tool wear and productivity when end milling Inconel 718. The results showed that areas can be identified in which a specific combination of tool material and geometry was superior. Kortabarria et al. [4] compared the residual stress profiles induced by different dry face turning conditions employing X-ray diffraction method, hole-drilling method and finite element modeling. Devillez et al. [5] presented results in terms of surface integrity and cutting forces when turning Inconel 718 in wet and dry conditions. They found that all residual stresses profiles present a thin layer exhibiting tensile residual stresses near the machined surface with a maximum tensile stress at the surface. This layer is followed by a zone with compressive stresses, several times thicker than the tensile layer. Kenda et al. [6] presented the influence of cryogenic machining on the surface integrity generated during turning of Inconel 718. They found that the cryogenic machining process generates larger compressive residual stresses, and prevail at deeper levels beneath the machined surface, thus resulting in improved product quality in terms of fatigue life and wear resistance.

Alauddin et al. [7] used uncoated tungsten carbide inserts in end milling Inconel 718 under dry conditions to test tool life on the basis of flank wear. Immersion ratio ( $a_r/D$ : radial depth of cut/cutter diameter) was used to classify end milling processes. Full-immersion and half-immersion end milling operations were utilized for tool life testing. For most of the cutting tests, non-uniform flank wear and localized flank wear were dominant. They also concluded that cutting speed influences the tool life significantly in full-immersion end milling and down cut provides longer tool life than up cut in half-immersion end milling. Sharman et al. [1] outlined a three-factor, two-level full factorial cutting experiment at two levels to study tool life when high speed end milling Inconel 718 with ball nose cutter. From the ANOVA results for tool life, they concluded that tool coating was the main factor affecting tool life, followed by cutting speed and

workpiece angle. They also found that the primary tool wear mechanism was adhesive and a BUE (build-up edge) was seen on the tools. Kim et al. [8] applied three different cutting environments: dry, flood coolant, and compressed chilly-air coolant to investigate the tool flank wear evolution when high-speed milling Inconel 718. Before reaching the maximum flank wear of 0.3 mm, almost similar cutting lengths under the three different environmental conditions were observed at higher cutting speed. It was explained that the cutting fluid and compressed chilly-air failed to infiltrate into the interfaces to quench the thermal friction generated heat due to the great pressure at the tool-chip and tool-workpiece interfaces during high speed machining. Jawaid et al. [9] performed face milling tests with two TiN coated and an uncoated tungsten carbide tools on Inconel 718 superalloy to study the effect of cutting speed and feed rate on tools performance under wet conditions. Wear rate was observed to increase with increased cutting speed for each fixed feed. Coated tools performed better than uncoated tools at most of the cutting conditions which can be attributed to the high wear resistance and low thermal conductivity of TiN coating layer. Li et al. [10] developed an online optical system to inspect tool wear conditions during end milling of AISI H13 and Inconel 718. No action of disassembling the tool from the spindle is needed when examining on flank face and thus in-situ monitoring tool condition can be achieved. Visible results from optical camera directly reflect what was happening on the tool/material interface and it is not necessary to correlate the object of interest with other indirect parameters. Guo et al. [11] conducted a review of experimental study on surface integrity characterization after machining of hardened and difficult-to-cut alloys.

Compared with sharp tools, worn tools will negatively affect surface integrity and fatigue performance of the machined components. The surface integrity and fatigue performance of the

machined components by worn tools would deteriorate to an unpredictable level due to the progression of tool wear. Machined components may be put under various applications. However, no matter what conditions the machined components will be experiencing, their performance is always the first concern from customers' perspective. The performance of the components largely depends on the machining process which generally affects the very thin layer beneath the machined surface and the surface integrity of that thin layer can directly determine the performance. Therefore, the connection among tool wear, surface integrity, and fatigue performance of machined parts should be well recognized in order to maintain the desired quality of products in mass production process. The effects of cutting tool flank wear and workpiece surface integrity on fatigue life of machined components were studied by several investigators. Koster and Field [12] suggested that the main mechanical property affected by machining is high cycle fatigue strength and the actual endurance limit depends on the particular process used and the severity of operation. In early fatigue models [13-15], performance of the parts was often attributed to surface roughness parameter Ra (arithmetic average). Koster [16] summarized experimental work on fatigue strength of different workpiece materials (iron, nickel and titanium based alloys) subject to a range of machining processes: finish grinding, milling and turning. He found that the endurance limit of steel was dependent on surface roughness while other two were not. Machining induced residual stress has been recognized as one of the main factors which will significantly affect fatigue life [16-17]. It has been shown that the presence of a white layer associated with high tensile residual stress by a worn tool is very detrimental for rolling contact fatigue performance [18-19]. Guo and Yen [20] concluded that the slope of a compressive residual stress profile is important for rolling contact fatigue damage. Guo et al. [21] also concluded that the nature of surface residual stress and the depth of maximum compressive

residual stress in the subsurface are important for rolling contact fatigue damage. Li, Guo and Guo [22] comprehensively investigated the fundamental relationships among tool wear, surface integrity, and fatigue in hard milling of tool steel AISI H13. Matsumoto et al. [23] studied the effect of machining processes on the fatigue strength of AISI 4340 and they found that the average fatigue life of cut samples was higher than those ground samples. Denkena's [24] fatigue tests show that the turned samples using fresh tools exhibit higher fatigue strength than the ground ones. Only when a massive tool wear (flank wear 200  $\mu\text{m}$ ) occurs, the fatigue strength of the turned samples drop below the fatigue strength of the ground ones. Taylor and Clancy [25] concluded that surface roughness had a distinct effect on the fatigue life.

Based on different dynamic cyclic loading conditions, a variety of fatigue tests can be performed to determine the fatigue life of machined components, such as four point bending, three point bending, rolling contact, R.R. Moore rotating, etc. Depending on the potential application of machined parts, a proper fatigue testing mode should be selected. Four point bending fatigue test is often used to characterize the flexure strength of a specimen while it is also applicable for fatigue studies. Jeelani and Collins [26] studied the effect of electric discharge machining on the fatigue life of Inconel 718 alloy at room temperature. The fatigue test results indicated that fatigue lives of the machined specimens decreased slightly compared with those of the parent metal specimens, but remained unchanged with variations in cutting speed. Bentley, Mantle and Aspinwall [27] compared the effect of grinding and high speed milling (HSM) on the fatigue strength of a gamma titanium aluminide intermetallic alloy by four-point bend fatigue test. A reduction in fatigue life when finish-grinding has been found compared with rough grinding and polished samples. The fatigue strength of the material was substantially increased by HSM which was explained to be due to the compressive residual stress near the surface. Zhai

et al. [28] carried out four-point bending test using a self-aligning rig to study the fatigue of 8090 Al-Li alloy. The fatigue tests showed that both the lifetime and the fracture position might vary with the sample geometry. By using the same rig, Li et al. [29] performed four-point bending fatigue test on a high-strength AA 2026 Al alloy which was in the form of extrusion bars with square and rectangular cross sections. They made conclusions that fatigue cracks were predominantly initiated at Fe-containing particles on the surface in these 2026 alloys and the fatigue fractographies of the square and rectangular extrusion bars were different due to different grain structures. Yang and Liu [30] studied the impact of machining processes on Ti 6Al-4V samples' fatigue life scatters under identical loading conditions. Fatigue life variance due to the machining process was quantitatively evaluated and process capability of fatigue life was also analyzed. Li, Guo and Barkey [31] estimated fatigue endurance limits of hard milled AISI H13 specimens and the endurance limit was found to be strongly depending on the testing reliability. The fatigue life variation of those AISI H13 samples caused by different tool wears was also experimentally determined by four-point bending test [32]. They drew the conclusion that the number of load cycles before fracture generally decreased when increasing cutting tool flank wear.

### 6.3. Tool wear vs. surface integrity experiment

End milling of Inconel 718 experiments were carried out with flood coolant on a 3-axis CINCINNATI Arrow 500 CNC vertical machining center. Tool flank wear was monitored and measured by an on-line optical tool monitoring system integrated with the CNC machine, see Figure 6.1.

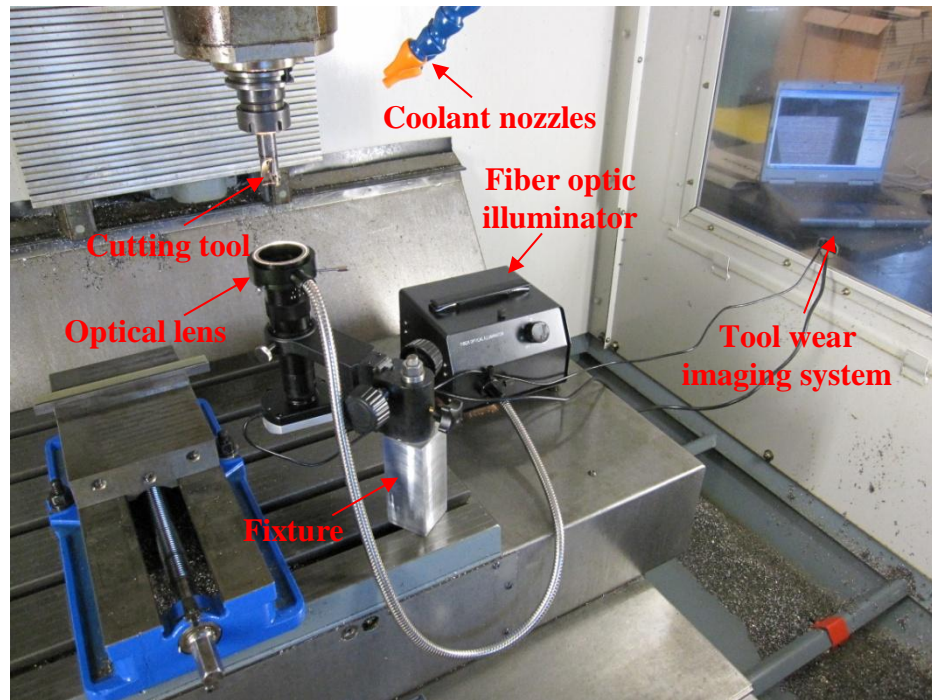


Fig. 6.1 On-line optical tool monitoring system for end milling.

### 6.3.1. Work material and cutting tool

The Inconel 718 work samples used in milling experiments were 25 mm × 21 mm × 13 mm rectangular blocks. They were thoroughly hardened and tempered to  $45 \pm 1$  HRC. Table 6.1 shows the nominal chemical composition of the precipitation hardened Inconel 718. Before milling tests, the top and bottom sample surfaces were face milled to remove the heat treatment induced surface defects and ensure flatness to eliminate machining errors.

Table 6.1 Chemical composition of Inconel 718 (wt.%).

Element	wt-%
Ni	51.49
Cr	18.31
Fe	Balance
Cb	5.03
Mo	2.93
Ti	1.04
Al	0.54
Co	0.20
Si	0.07
Mn	0.070
C	0.043
P	0.007
Cu	0.039
B	0.002
Ta	0.001
S	0.0007

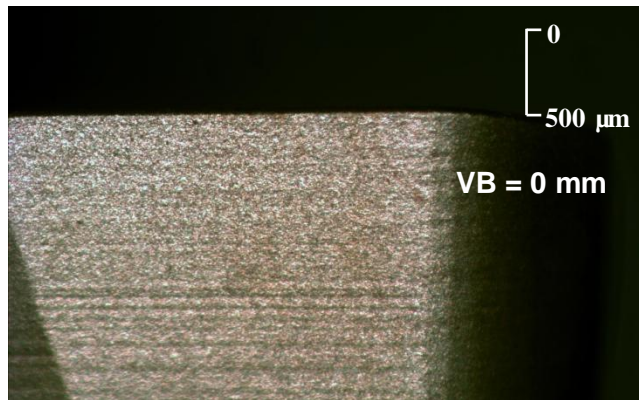
The cutting tool used in the milling tests was a 20 mm diameter end milling cutter with one PVD (Ti, Al) N/TiN-coated carbide inserts. The tool holder and the PVD-coated inserts were made by SECO Tool Company.

### 6.3.2. Experimental design

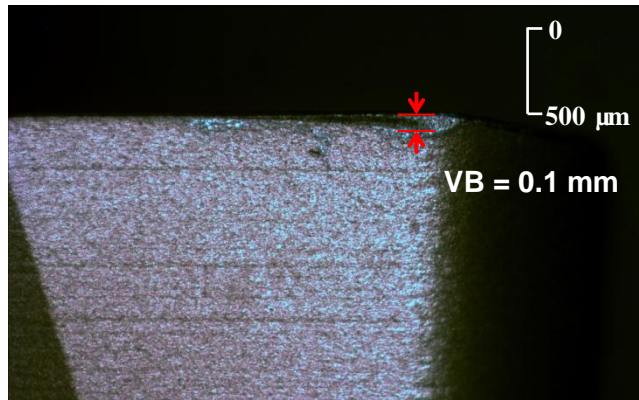
Table 6.2 lists the process conditions for the milling experiments. Twenty-one cutting tests (7 different cutting conditions, with three levels of initial tool flank wear:  $VB = 0$ ,  $VB = 0.1$  mm, and  $VB = 0.2$  mm used for each cutting condition, see Figure 6.2) were planned to study the effect of tool flank wear on surface integrity under a variety of cutting parameter combinations.

Table 6.2 End milling experiment plan to characterize surface integrity.

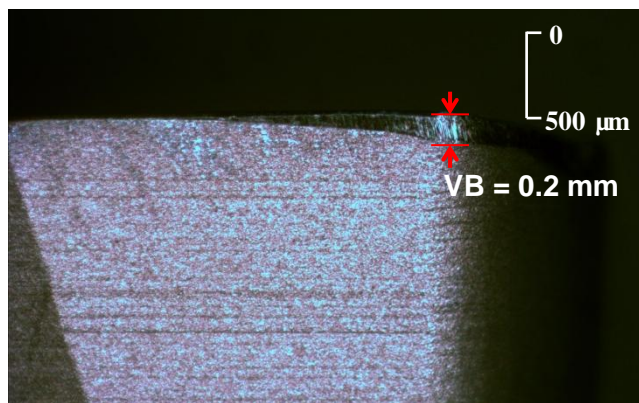
Sample #	VB (mm)	Cutting condition #	Cutting speed [m/min]	Feed per tooth [mm/tooth]	Radial DOC [mm]	Axial DOC [mm]
1	0	1	40	0.15	0.5	0.5
2	0.1					
3	0.2					
4	0	2	60	0.15	0.5	0.5
5	0.1					
6	0.2					
7	0	3	80	0.15	0.5	0.5
8	0.1					
9	0.2					
10	0	4	60	0.1	0.5	0.5
11	0.1					
12	0.2					
13	0	5	60	0.2	0.5	0.5
14	0.1					
15	0.2					
16	0	6	60	0.15	0.3	0.5
17	0.1					
18	0.2					
19	0	7	60	0.15	0.4	0.5
20	0.1					
21	0.2					



(a) Fresh tool (flank wear = 0)



(b) Tool with flank wear = 0.1 mm



(c) Tool with flank wear = 0.2 mm

Fig. 6.2 Initial tool flank wear.

### 6.3.3. Sample preparation

The machined samples were degreased by successive ultrasonic cleaning for 15 minutes in acetone, and then rinsed with deionized water before surface integrity characterization. Then, the samples were cross-sectioned with an abrasive cut-off saw at gentle cutting conditions to avoid excessive modification of surface integrity of the milled workpieces. After being mounted in cold setting epoxy, the samples were gently polished to a mirror-like finish. The samples were then etched with waterless Kalling's reagent (5 g  $\text{CuCl}_2$ , 100 ml HCl, and 100 ml Ethanol), rinsed in cold water, and dried by air.

### 6.3.4. Surface integrity characterization

After end milling test, surface integrity factors including: surface roughness, microstructure, and microhardness were characterized in this study.

#### 6.3.4.1. Surface roughness

Surface roughness along feed direction and step-over direction was measured by a profiler. In order to get statistical stable data, three measurements along each direction were made at different locations when tracing on the machined surfaces. Figure 6.3 shows the machined surface texture. The measured results of surface roughness along two directions were shown in Figure 6.4.

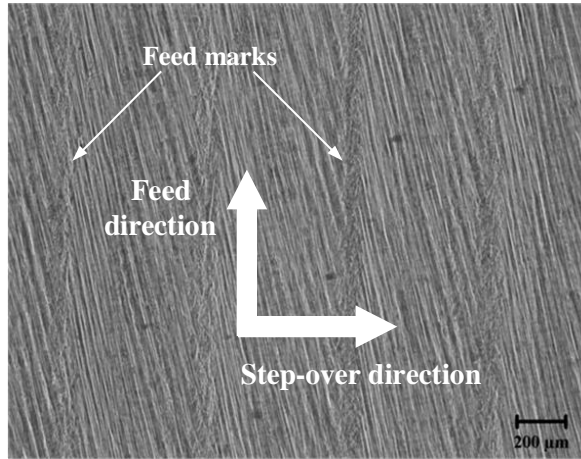


Fig. 6.3 Texture of machined surface.

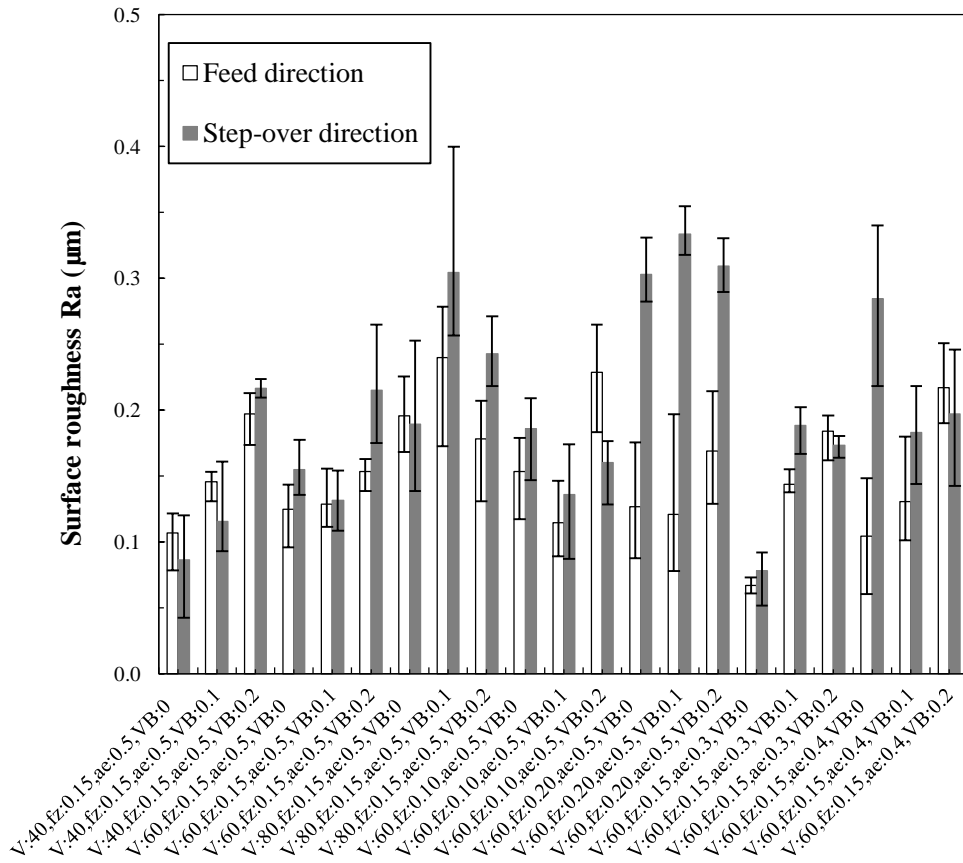


Fig. 6.4 Average, maximum, and minimum surface roughness ( $R_a$ ) in the feed and step-over directions.

It shows that eighteen of all the twenty-one milled surface had much higher roughness along step-over direction than along feed direction under the milling conditions listed in Table 6.2. Only three out of the twenty-one milled surfaces have surface roughness value of  $0.3 \mu\text{m} < R_a < 0.4 \mu\text{m}$  in step-over direction and the remaining samples have surface roughness between  $0.1 \mu\text{m}$  and  $0.3 \mu\text{m}$  in both directions. In step-over direction, surface roughness increases with the increase of cutting speed at  $VB = 0$  and  $VB = 0.1 \text{ mm}$ . In feed direction, surface roughness generally increases when tool flank wear increases at each cutting speed level. The effect of feed per tooth can also be seen that  $f_z = 0.15 \text{ mm/tooth}$  generally produces smaller surface roughness in both directions compared with  $f_z = 0.10 \text{ mm/tooth}$  and  $f_z = 0.20 \text{ mm/tooth}$ .

#### 6.3.4.2. Subsurface microstructure

Although the chips carry away the majority of heat generated in milling process, a certain percentage of heat still dissipates into the machined surface. At abrasive milling conditions (high cutting speed, small feed rate, and large tool wear), it is possible that sufficient heat will conduct into the workpiece and induce phase transformation to form a white layer on the machined surface. However, optical images of the subsurface microstructure of twelve of the twenty-one samples do not show a noticeable white layer (Figure 6.5). The possible reason is that the periodic tool/work contact reduces the amount of heat dissipated into the machined surface. Compared with the continuous tool/work contact in turning and grinding processes, milling would have less chance to induce thermal white layer at the same level of tool wear. This may explain why a white layer could be generated much more easily in turning and grinding.

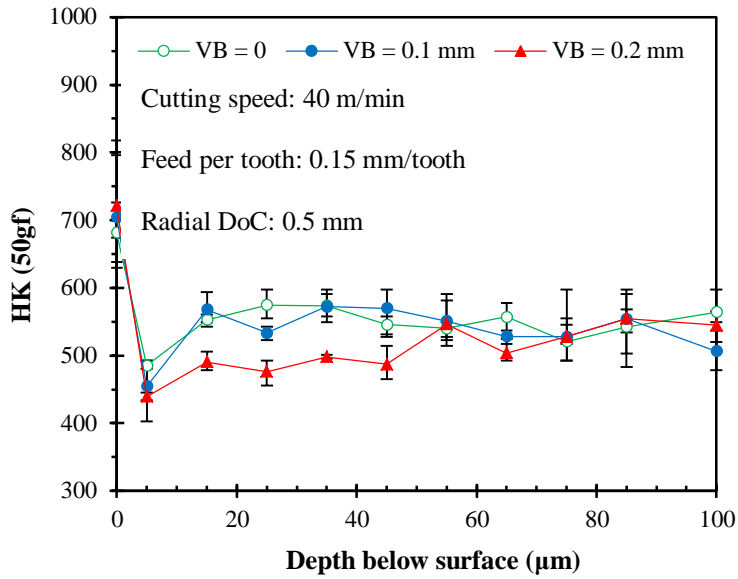


Fig. 6.5 Optical images of subsurface microstructure.

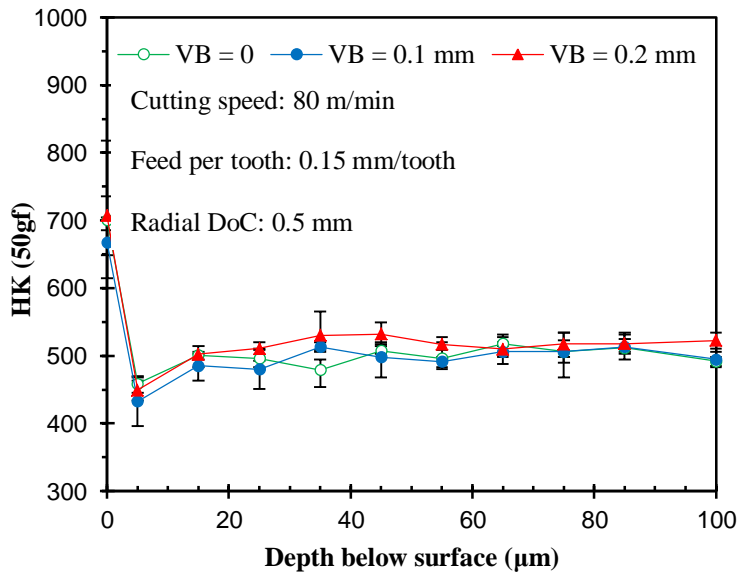
#### 6.3.4.3. Surface and subsurface microhardness

Microhardness on the surface and in the subsurface was measured at a load of 50 g for 10s using a Knoop indenter. Microhardness of the machined surfaces was measured in two orientations: parallel and perpendicular to the feed direction. Three measurements were performed in each direction and an average of six measured values was used as surface microhardness. In the subsurface, microhardness measurements were taken at about 10  $\mu\text{m}$  intervals between successive readings up to 100  $\mu\text{m}$ . Similarly, three measurements were made

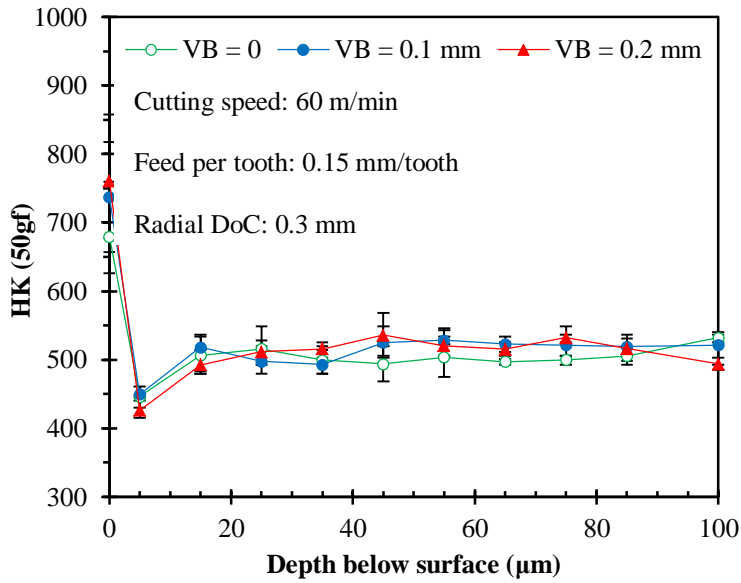
at the same depths in the subsurface. Figure 6.6 illustrates the microhardness profiles for twelve of the twenty-one milled samples.



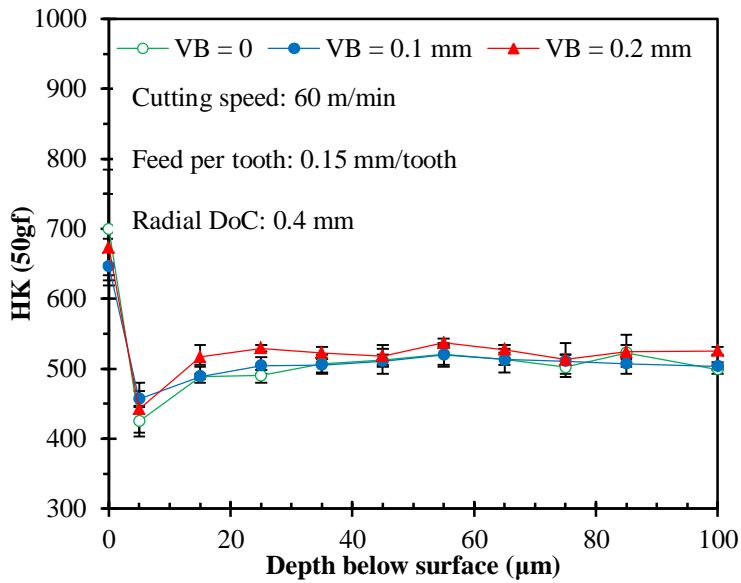
(a) Microhardness profiles for samples 1 ~ 3



(b) Microhardness profiles for samples 7 ~ 9



(c) Microhardness profiles for samples 16 ~ 18



(d) Microhardness profiles for samples 19 ~ 21

Fig. 6.6 Microhardness profiles for machined surface and subsurface.

Since the surface material experienced both mechanical and thermal loading, surface properties depend on the coupling effects of the two loadings. As thermal loading in milling has the characteristics of discontinuity and short time duration, while mechanical loading would be the predominant factor determining the surface properties. Based on the measured microhardness data for all the samples, the work-hardening resulted from mechanical loading on the machined surface would be dominant since much higher average microhardness occurred on the surface than the subsurface. The low microhardness at approximately 5  $\mu\text{m}$  into the subsurface is likely induced by the edge effect of micro-indenter rather than thermal effect. The reason for the measured low hardness was explained in [33].

#### 6.4. Four-point bending fatigue test

##### 6.4.1. Test specimen preparation

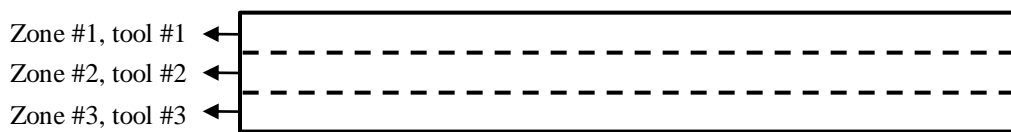
The Inconel 718 rectangular blocks used for fatigue testing were of dimensions: 200 mm  $\times$  21 mm  $\times$  12 mm. Before end milling tests, the blocks were also face milled on top and bottom surfaces to remove the heat treatment induced surface defects and ensure flatness to eliminate errors that may affect experimental results. The cutting tool used in the machining tests was a 20 mm diameter end milling cutter with one PVD (Ti, Al) N/TiN-coated carbide insert. The tool holder and the PVD-coated inserts were all made by SECO Tool Company.

Four rectangular Inconel 718 blocks were sequentially end milled by the same cutting tools. So the milled blocks are categorized as specimens machined by tools with different flank wears. Both top and bottom of the blocks were machined using the same cutting parameters, see Table 6.3. Flood coolant was applied throughout the tests. In order to assign the flank wear value ranges into four specimens without causing tool failure, each side of the specimens was equally

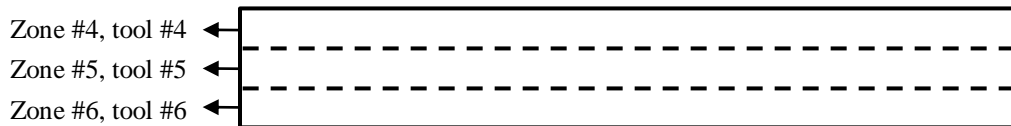
divided into three zones and three individual inserts were used to mill one surface which greatly shortened the cutting time for each tool (about 13 minutes in each zone), see Figure 6.7. Three fresh tools were first applied to mill on the top surface of one workpiece and then sequentially on the other top surfaces of the three remaining specimens. Following the same procedure, the bottom surfaces of the four specimens were prepared using another three fresh tools. In this way, the top and bottom surfaces of the end milled specimens were of the similar surface conditions. Representative images of tool wear evolution on flank face can be seen in Figure 6.8 (tool #2 milling in zone #2 of the four samples). Before fatigue test, the specimens' edges were polished using a 600-grit sandpaper to eliminate the effects of burrs and sharp-edges on fatigue life.

Table 6.3 End milling parameters to prepare fatigue samples.

Cutting speed $V_c$ (m/min)	Axial depth of cut $a_p$ (mm)	Feed rate $v$ (mm/min)	Radial depth of cut $a_e$ (mm)	Rotational speed $N$ (rpm)
90	0.5	215	0.5	1433

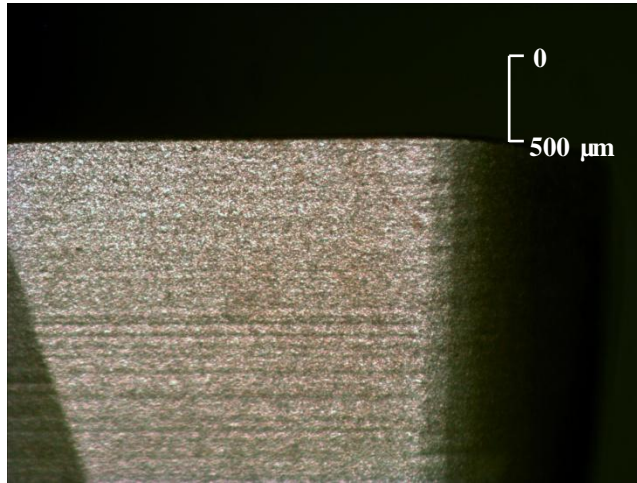


(a) Top view of milled samples

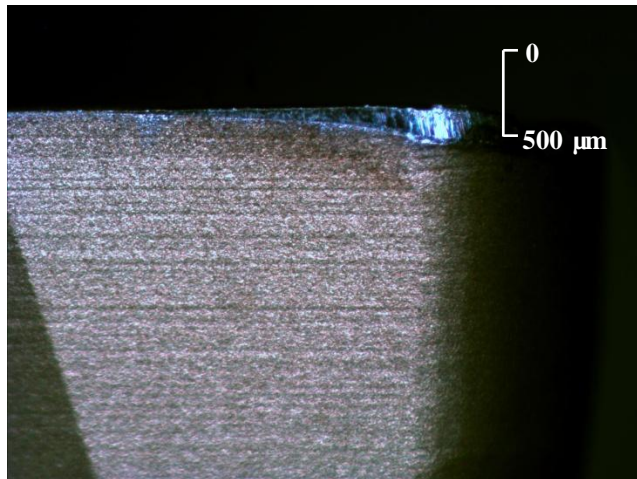


(a) Bottom view of the milled samples

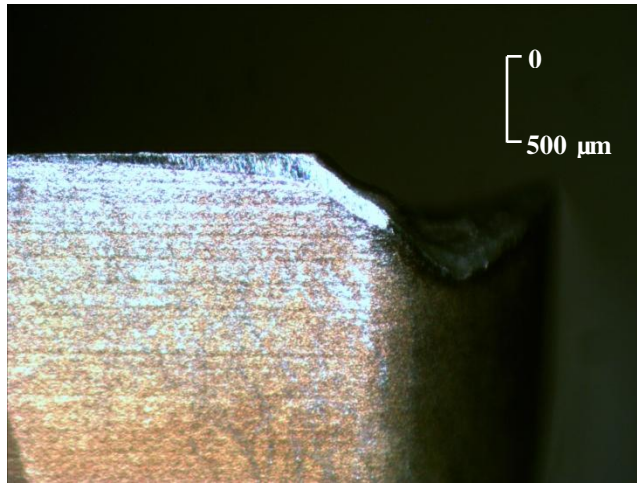
Fig. 6.7 Divided zones on top and bottom surfaces of the workpiece.



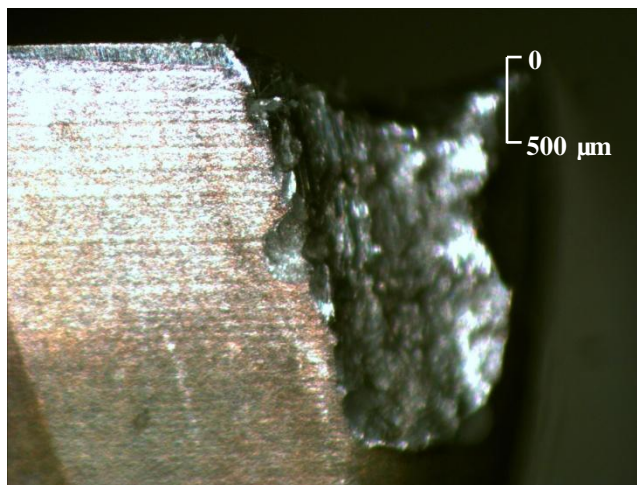
(a) Fresh tool ( $t = 0$ )



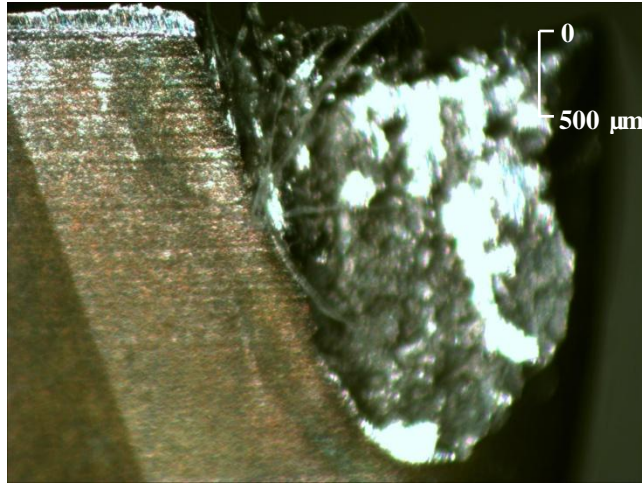
(b) Tool after cutting 13 minutes



(c) Tool after cutting 26 minutes



(d) Tool after cutting 39 minutes



(e) Tool after cutting 52 minutes

Fig. 6.8 Tool conditions before and after milling zone #2 of the four samples.

#### 6.4.2. Fatigue test system setup

Four-point bending fatigue tests were run at room temperature on a MTS 810 Test System (Figure 6.9). The MTS 810 test system consists of a servo-hydraulic fatigue testing machine, a Flextest SE digital controller, and the MultiPurpose TestWare Software (MPT). The test specimen sits on the loading fixture which is bolted to the oscillating piston. The oscillating piston moves up and down with the loading fixture at a certain frequency. The supporting fixture is fixed at supporting end to keep the loading direction constant.

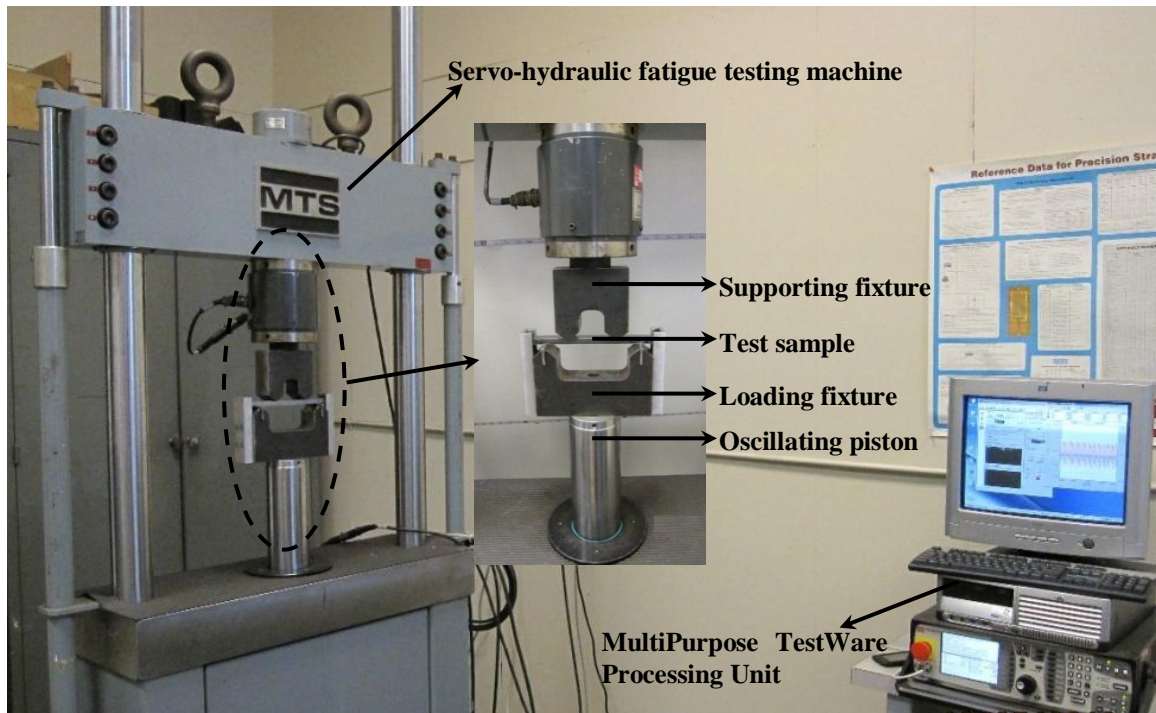


Fig. 6.9 MTS four-point bending fatigue testing system.

A cyclic load was applied at a frequency of 10 Hz and with a sinusoidal waveform. The nominal stress can be calculated by the beam theory:

$$\sigma = \frac{3Pa}{wh^2} \quad (6.1)$$

where specimen width  $w = 21$  mm, height  $h = 12$  mm,  $a = \frac{1}{2} b = 38.1$  mm (Figure 6.10).

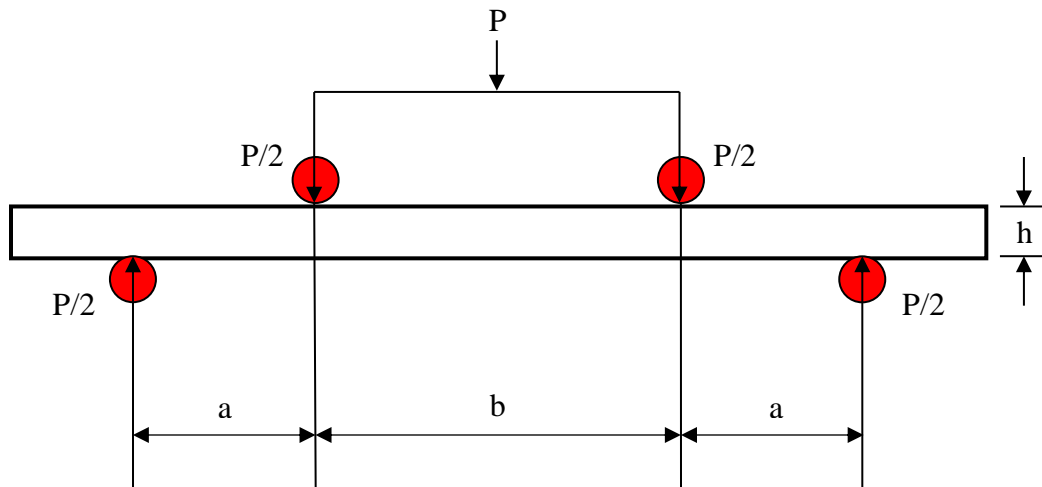


Fig. 6.10 Schematic of four-point bending fatigue testing system.

The maximum tensile stress  $\sigma_{\max}$  at the bottom of test samples was set to be 800 MPa, which is larger than 50% of the UTS (ultimate tensile strength: 1435 MPa) of Inconel 718. As shown in Figure 6.10, the load-span  $b$  was set to 76.2 mm, support-span  $= 2a + b = 152.4$  mm, and the stress amplitude ratio  $R = 0.1$ . The fatigue testing conditions are listed in Table 6.4.

Table 6.4 Four-point bending fatigue testing condition.

Max. stress $\sigma_{\max}$ (MPa)	800
Min. stress $\sigma_{\min}$ (MPa)	80
Stress ratio $R$ ( $\sigma_{\min}/\sigma_{\max}$ )	0.1
Mean stress $\sigma_m = (\sigma_{\min} + \sigma_{\max})/2$ (MPa)	440
Stress amplitude $\sigma_a = (\sigma_{\max} - \sigma_{\min})/2$ (MPa)	360

### 6.4.3. Fatigue performance

#### 6.4.3.1. Four-point bending fatigue testing

Fatigue life management of machined components under the progression of tool wear is concerned from the viewpoint of product performance. Fatigue test was terminated when the failure of the specimen occurred or the upper limit of loading cycles, which was preselected as 4 million cycles (in consideration of testing time, cost, facility capability, etc.) was reached. However, none of the four samples failed within  $4 \times 10^6$  cycles, see Figure 6.11.

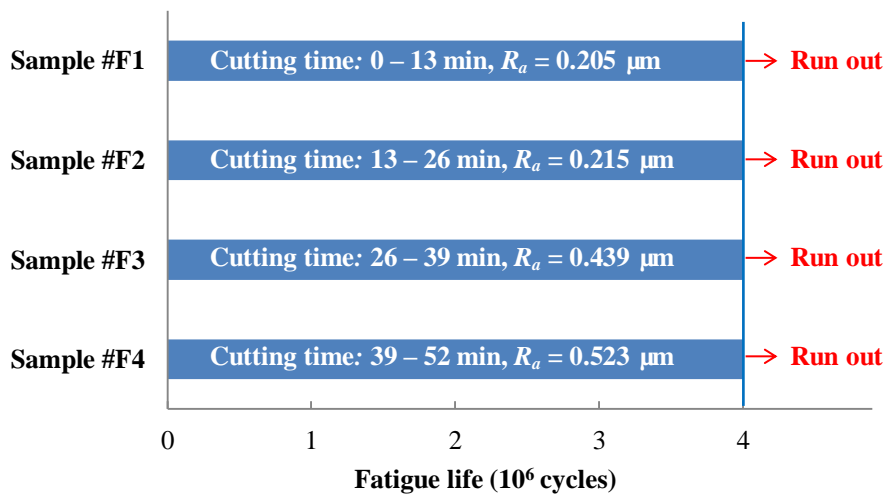


Fig. 6.11 Fatigue life of the four end milled Inconel 718 samples.

#### 6.4.3.2. Endurance limit estimation

Endurance limit, or  $S_e$ , is used to describe the amplitude of cyclic stress that can be applied to the material without causing fatigue failure. In typical  $S$ - $N$  diagrams for steels, a knee point usually occurs and its corresponding strength is termed endurance limit  $S_e$ . For fatigue experimental design and fatigue analysis, an estimation of endurance limit is needed. Generally, the endurance limit of the controlled laboratory specimen,  $S_e'$ , will be determined first and then it

can be modified by multiplicative factors by incorporating the effects of surface finish, sample size, loading mode, temperature, and miscellaneous items. Even though the material of the testing specimens is nickel-based superalloy, which is very different from steels and generally does not exhibit well-defined endurance limit within  $1 \times 10^6$  cycles, a similar estimation of the endurance limit is more or less helpful for the experimentalists to better design the test conditions instead of probing without any possible expectations. The endurance limit  $S_e$  of end milled Inconel 718 samples for four-point bending fatigue testing is estimated below.

Since the tensile strength of Inconel 718,  $S_{ut}$ , is 1435 MPa, the endurance limit of the controlled laboratory specimen,  $S_e'$ , is estimated as  $S_e' = 700$  MPa based on rule of thumb:

$$S_e' = \begin{cases} 0.5 S_{ut}, & \text{when } S_{ut} \leq 1400 \text{ MPa} \\ 700 \text{ MPa}, & \text{when } S_{ut} > 1400 \text{ MPa} \end{cases} \quad (6.2)$$

Then, modifying factors  $K_a, K_b, K_c, K_d, K_e, K_f$ , are applied to compensate the difference of lab controlled samples and the milled samples [34], see Table 6.5.

Table 6.5 Endurance limit modifying factors.

Surface factor $K_a = aS_{ut}^b$	0.657
Size factor $K_b = 1.24d_e^{-0.107}$	0.944
Loading factor $K_c$	1 (bending mode)
Temperature factor $K_d$	1 (room temperature)
Reliability factor $K_e = 1 - 0.08 \cdot z_\alpha$	$1 - 0.08 \cdot z_\alpha$ (varies with reliability)
Miscellaneous factor $K_f$	1

(1) Surface finish factor  $K_a$

$$K_a = aS_{ut}^b \quad (6.3)$$

For machined components,  $a = 4.51$ ,  $b = -0.265$

(2) Size factor  $K_b$  (when  $2.79 \leq d_e \leq 51$  mm)

$$K_b = 1.24 d_e^{-0.107}, d_e = 0.808 (h \times b)^{0.5} \quad (6.4)$$

$d_e$ : effective dimension;  $h$ : height, 12 mm;  $b$ : width, 21 mm

(3) Loading factor  $K_c$

$$K_c = 1 \text{ (bending)} \quad (6.5)$$

(4) Temperature factor  $K_d$

$$K_d = 1 \text{ (room temperature)} \quad (6.6)$$

(5) Reliability factor  $K_e$

$$K_e = 1 - 0.08 \times Z_\alpha \quad (6.7)$$

$$Z_\alpha = 3.091 \text{ (reliability 99\%)}$$

(6) Miscellaneous factor  $K_f$

$$K_f = 1 \quad (6.8)$$

From Marin equation [35],

$$S_e = K_a K_b K_c K_d K_e K_f S_e' \quad (6.9)$$

$$S_e = 0.657 \times 0.944 \times 1 \times 1 \times K_e \times 1 \times 700$$

$$S_e = 434.146 \times (1 - 0.08 \cdot z_\alpha)$$

So the endurance limit  $S_e$  is a function of reliability factor  $K_e$  and it varies with the transformation variate  $z_\alpha$  determined by the reliability. The statistical term reliability factor  $K_e$  can vary from 0.62 (reliability 99.9999%,  $z_\alpha = 4.753$ ) to 1.00 (reliability 50%,  $z_\alpha = 0$ ) which brings variation to the estimated endurance limit ( $S_e = 269.170 \sim 434.146$  MPa). While, when reliability is over 99% ( $z_\alpha = 2.326$ ) and then the estimated endurance limit will be  $S_e < 353.335$

MPa. In this case, the estimated endurance limit is below stress amplitude  $\sigma_a$  given in the test and fatigue failure is expected to happen within one million cycles. However, the experimental outcome is not supportive to the estimation.

## 6.5. Conclusions

This work focused on the basic relationships between tool wear, surface integrity, and fatigue in end milling of nickel-based superalloy Inconel 718. The key results may be summarized as follows:

- All the milled surfaces had roughness of less than 0.4  $\mu\text{m}$ . Sixteen of the twenty-one samples had surface roughness less than 0.25  $\mu\text{m}$ . For fifteen out of the twenty-one milled samples, surface roughness was higher in step-over direction than that in feed direction. Tool wear up to 0.2 mm does not necessarily produce a rougher surface.
- Thermal-induced white layers were not observed for the concerned tool wear levels, which may be explained by the improved cooling effect from the periodic tool/work contact in milling compared to constant tool/work contact in turning and grinding.
- The machined surface has been work-hardened due to the dominant mechanical loading which can be seen by relatively higher microhardness at milled surface. While, the microhardness of subsurface became stable at about 80  $\mu\text{m}$  below machined surface.
- Four-point bending fatigue tests show that no fracture happened within four million cycles for all the samples milled by tools with variable wear conditions. The possible reason is that nickel-based alloy's characteristic of ductility, which reduces with

increased temperature, strongly prohibits crack initiation and prevents crack propagation. Due to the constraints of sample size and point-to-point varying nature of tool wear and surface integrity, an exact relationship among tool wear, surface integrity, and fatigue life would be difficult to determine experimentally.

## 6.6. References

- [1] Sharman ARC, Dewes RC, Aspinwall DK. Tool life when high speed ball nose end milling Inconel 718. *Journal of Materials Processing Technology* 2001; 118: 29–35.
- [2] Aspinwall DK, Dewes RC, Ng EG, Sage C, Soo SL. The influence of cutter orientation and workpiece angle on machinability when high-speed milling Inconel 718 under finishing conditions. *International Journal of Machine Tools & Manufacture* 2007; 47: 1839-1846.
- [3] Krain HR, Sharman ARC, Ridgway K. Optimisation of tool life and productivity when end milling Inconel 718. *Journal of Materials Processing Technology* 2007; 189: 153-161.
- [4] Kortabarria A, Madariaga A, Fernandez E, Esnaola JA, Arrazola PJ. A comparative study of residual stress profiles on Inconel 718 induced by dry face turning. *Procedia Engineering* 2001; 19: 228-234.
- [5] Devillez A, Le Coz G, Dominiak S, Dudzinski D. Dry machining of Inconel 718, workpiece surface integrity. *Journal of Materials Processing Technology* 2011; 211: 1590-1598.
- [6] Kenda J, Pusavec F, Kopac J. Analysis of residual stresses in sustainable cryogenic machining of nickel based alloy – Inconel 718. *Journal of Manufacturing Science and Engineering* 2011; 133/041009: 1-7.
- [7] Alauddin M, El Baradie MA, Hashmi MSJ. Tool-life testing in the end milling of Inconel 718. *Journal of Materials Processing Technology* 1995; 55: 321-330.
- [8] Kim SW, Lee DW, Kang MC, Kim JS. Evaluation of machinability by cutting environments in high-speed milling of difficult-to-cut materials. *Journal of Materials Processing Technology* 2001; 111: 256-260.
- [9] Jawaid A, Koksai S, Sharif S. Cutting performance and wear characteristics of PVD coated and uncoated carbide tools in face milling Inconel 718 aerospace alloy. *Journal of*

- Materials Processing Technology 2001; 116: 2-9.
- [10] Li W, Singh HM, Guo YB. An online optical system for inspecting tool condition in milling of H13 tool steel and IN 718 alloy. *International Journal of Advanced Manufacturing Technology* 2012; DOI: 10.1007/s00170-012-4548-7.
  - [11] Guo YB, Li W, Jawahir IS. Surface integrity characterization and prediction in machining of hardened and difficult-to-machine alloys: a state-of-art research review and analysis. *Machining Science and Technology* 2009; 13/4: 437-470.
  - [12] Koster WP, Field M. Effects of machining variables on the surface and structural integrity of titanium. *Proceedings of the North American Manufacturing Research Conference, SME* 1973; 2: 67-87.
  - [13] Thomas WN. Effect of scratches and of various workshop finishes upon the fatigue strength of steel. *Engineering* 1923; 116: 449-485.
  - [14] Noll GC, Erickson GC. Allowable stresses for steel members of finite life. *Proceedings of the Society of Experts for Stress Analysis* 1948; 5/2: 132-143.
  - [15] Fluck PG. The influence of surface roughness on the fatigue life and scatter of test results of two steels. *Proceedings of American Society for Testing Materials* 1951; 51: 584-592.
  - [16] Koster W. Effect of residual stress on fatigue of structural alloys. *Proceedings of the Third International Conference, ASM International, Indianapolis, Indiana, USA* 1991. p. 1-9.
  - [17] Brinksmeier E, Cammett JT, Konig W, Leskovar P, Peters J, Tönshoff HK. Residual stresses-measurement and causes in machining processes. *Key-Note-Papers CIRP Ann.* 1982; 31/2: 491-510.
  - [18] Guo YB, Schwach DW. A fundamental study on the impact of surface integrity by hard turning on rolling contact fatigue. *Int. J. of Fatigue* 2006; 28: 1838-1844.
  - [19] Guo YB, Schwach DW. An experimental investigation of white layer on rolling contact fatigue using acoustic emission technique. *Int. J. of Fatigue* 2005; 27: 1051-1061.
  - [20] Guo YB, Yen DW. Hard turning versus grinding - the effect of process-induced residual stress on rolling contact. *Wear* 2004; 256: 393-399.
  - [21] Guo YB, Warren AW, Hashimoto F. The basic relationships between residual stress, white layer, and fatigue life of hard turned and ground surfaces in rolling contact. *CIRP J. Manuf. Sci. Tech.* 2010; 2/2: 129-134.
  - [22] Li W, Guo C, Guo YB. Superior surface integrity by sustainable dry hard milling and impact on fatigue. *Annals of the CIRP* 2013 (accepted).

- [23] Matsumoto Y, Magda D, Hoepfner DW, Kim TY. Effect of machining processes on the fatigue strength of hardened AISI 4340 steel. *ASME J. Eng. Ind.* 1991; 113: 154-159.
- [24] Denkena B, Tönshoff HK, Friemuth T, Muller C, Zenner H, Renner F, Koehler M. Fatigue strength of hard turned components. *Proceedings of the 1st International Conference on Manufacturing Engineering*, Sani, Halkidiki, Greece 2002. p. 185-194.
- [25] Taylor D, Clancy OM. The fatigue performance of machined surfaces. *Fatigue Fract. Eng. Mater. Struct.* 1991; 14/2-3: 329-336.
- [26] Jeelani S, Collins MR. Effect of electric discharge machining on the fatigue life of Inconel 718. *International Journal of Fatigue* 1988; 10: 121-125.
- [27] Bentley SA, Mantle AL, Aspinwall DK. The effect of machining on the fatigue strength of a gamma titanium aluminide intermetallic alloy. *Intermetallics* 1999; 7: 967-969.
- [28] Zhai T, Xu YG, Martin JW, Wilkinson AJ, Briggs GAD. A self-aligning four-point bend testing rig and sample geometry effect in four-point bend fatigue. *International Journal of Fatigue* 1999; 21: 889–894.
- [29] Li JX, Zhai T, Garratt MD, Bray GH. Four-point-bend fatigue of AA 2026 aluminum alloys. *Metallurgical and Materials Transactions* 2005; 36A: 2529–2539.
- [30] Yang XP, Liu CR. Investigating machining impact on fatigue variance: a machining quality perspective. *Transactions of the ASME* 2005; 127: 492-502.
- [31] Li W, Guo YB, Barkey ME. Surface integrity and fatigue strength of hard milled surfaces. *Proceedings of the 2011 ASME International Manufacturing Science and Engineering Conference*, Corvallis, Oregon, USA 2011. p. 199-206.
- [32] Li W, Guo YB. Residual stress and fatigue properties of AISI H13 steel by sustainable dry milling. *Proceedings of the ASME 2012 International Manufacturing Science and Engineering Conference*, Notre Dame, Indiana, USA 2012.
- [33] Warren AW, Guo YB. On the clarification of surface hardening mechanisms by hard turning and grinding. *Trans. NAMRI/SME* 2006; 34: 309-316.
- [34] Budynas R, Nisbett J. *Shigley's Mechanical Engineering Design*. McGraw-Hill, New York, 2008.
- [35] Marin J. *Mechanical Behavior of Engineering Materials*. Prentice-Hall, New Jersey, 1962.

## CHAPTER 7

### ANALYSIS OF VARIANCE BASED PREDICTIVE MODEL FOR SURFACE ROUGHNESS IN END MILLING OF IN 718

#### Abstract

Tool flank wear during milling adversely affects surface integrity and, therefore, product performance of machined components. Surface integrity and machining accuracy deteriorate when tool wear progresses. In this paper, the effects of process parameters including cutting speed, feed, radial depth of cut, and tool flank wear, on surface roughness of IN 718 alloy ( $45 \pm 1$  HRC) by milling using PVD coated tools have been studied. Surface roughness in both feed and step-over directions under a variety of milling conditions was characterized. Three levels of tool flank wear ( $VB = 0, 0.1\text{mm}, 0.2\text{mm}$ ) were used in the experiments. At each level of tool wear, the effects of cutting speed, feed, and radial depth-of-cut on surface roughness were investigated, respectively. Based on analysis of variance (ANOVA), a predictive model of milled surface roughness has been developed by incorporating tool wear and process parameters.

## 7.1. Introduction

The Inconel family of alloys was first developed in 1940s to support the development of jet engines for aerospace applications. They are well suited for service in extreme conditions due to their high oxidation and corrosion resistance. In particular, they are usually employed in the hot sections of gas turbines, jet motors, rocket engines and spacecraft since they are more creep-resistant than steels after precipitation hardening and thus retain strength over a wide temperature range. IN 718 is one of the most commonly used nickel based alloys in aerospace industry. It is known to be among the most difficult-to-cut materials due to its high strength even at high temperatures, low thermal conductivity, and especially rapid work hardening. Therefore, machining IN 718 is a challenging task since it is associated with rapid cutting tool wear and thus surface integrity and product performance of machined parts are hard to be controlled in mass production.

When a tool has been used in cutting Inconel alloys, a decision must be made that the current worn tool should be either replaced before next cutting or used continuously. When tool wear reaches a certain level, a conservative way for ensuring machined components with acceptable surface integrity in subsequent cutting is to replace the worn tool with a fresh one. However, this will obviously increase manufacturing cost and reduce production efficiency since more tools will be consumed and more time on replacement will be spent. Undoubtedly, a considerable amount of manufacturing cost has been contributed by cutting tools. Tool wear is considered to be a critical factor that determines the machining economy since it is closely related to tool life and thus the production cost.

Basically, two main types of tool wear will occur in cutting: flank wear (at tool/work interface) and crater wear (at tool/chip interface). Generally, crater wear only has relatively less

effect on machined surface integrity unless the cutting edge fails. Therefore, flank wear is considered to be the most important wear mode if surface integrity is concerned. Compared with sharp tools, worn tools will negatively affect surface integrity of machined components. However, no matter what service conditions the machined components experience, their performance is always a high priority from a customer's perspective. The performance of the machined components can be significantly influenced by their surface integrity. Surface integrity of the machined components by worn tools would deteriorate to an unacceptable level due to the progression of tool wear [1, 2]. Surface roughness is a critical factor of surface integrity, and therefore it is of great interests in machining industry to investigate the inherent relationship between tool flank wear and surface roughness. In order to achieve high production efficiency, long fatigue life, and low manufacturing cost, the basic relationship between tool wear and surface roughness needs to be thoroughly studied to ensure the desired product quality in mass production.

## 7.2. Tool wear in machining Inconel alloys

The main problems encountered when machining IN 718 are short tool life, workpiece surface damage, and subsurface metallurgical damage due to work hardening [3]. Surface integrity in machining nickel-based superalloys was summarized in a recent review work [4].

Aspinwall et al. [5] conducted a comprehensive series of experiments on the effects of cutter orientation and workpiece angle on machinability in high speed milling of IN 718. It was found that compressive surface residual stress was generated when a horizontal upwards cutter orientation was employed, while a tensile stress would be observed by employing a horizontal downwards operation.

Sharman et al. [3] outlined a three-factor, two-level full factorial cutting experiment to study tool life when high speed end milling of IN 718 with ball nose cutter. From the ANOVA results for tool life, it was concluded that tool coating was the main factor affecting tool life, followed by cutting speed and workpiece angle. It was also found that the primary tool wear mechanism was adhesive and a BUE (build-up edge) was seen on the tools.

Kim et al. [6] applied three different cutting environments: dry, flood coolant, and compressed chilly-air coolant to investigate the tool flank wear evolution when high-speed milling of In 718. Before reaching the maximum flank wear of 0.3 mm, almost similar cutting lengths under the three different conditions were observed at higher cutting speed. It was explained that cutting fluid and compressed chilly-air failed to infiltrate into the interfaces to quench the thermal friction generated heat due to the great pressure at the tool-chip and tool-workpiece interfaces in high speed machining.

Jawaid et al. [7] performed face milling of In 718 with two conditions – one coated with TiN and another uncoated tungsten carbide tools to study the effect of cutting speed and feed rate on tools performance under wet conditions. Wear rate was observed to increase with increased cutting speed for each fixed feed. Coated tools performed better than uncoated tools at most of the cutting conditions which can be attributed to the high wear resistance and low thermal conductivity of TiN coating layer.

Alauddin et al. [8] used uncoated tungsten carbide inserts in end milling of IN 718 under dry conditions to test tool life on the basis of flank wear. Immersion ratio ( $a_r/D$ : radial depth of cut/cutter diameter) was used to classify end milling processes. Full-immersion and half-immersion end milling operations were utilized for tool life testing. For most of the cutting tests, non-uniform flank wear and localized flank wear were dominant. It was found that cutting speed

influences the tool life significantly in full-immersion milling and down cut provides longer tool life than up cut in half-immersion milling.

### 7.3. Experimental procedure

#### 7.3.1. Work material and cutting tool

In this study, nickel-based alloy IN 718 was prepared for milling experiments. Table 7.1 shows the nominal chemical composition of the precipitation hardened IN 718 with a bulk hardness of  $45 \pm 1$  HRC. Before end milling tests, the blocks were ground on the top and bottom surfaces to remove surface defects from heat treatment and ensure flatness to eliminate errors that may affect experimental results.

Table 7.1 Chemical compositions of IN 718 (wt. %).

Element	wt %
Ni	51.49
Cr	18.31
Fe	Balance
Cb	5.03
Mo	2.93
Ti	1.04
Al	0.54
Co	0.20
Si	0.07
Mn	0.070
C	0.043
P	0.007
Cu	0.039
B	0.002
Ta	0.001
S	0.0007

End milling of IN 718 was carried out on a CNC vertical machining center. The cutting tool used in the machining tests was a 20 mm diameter end milling cutter with one PVD (Ti, Al) N/TiN-coated carbide insert. The tool holder and the insert were made by SECO Tool Company. The tool flank wear was monitored and measured by an on-line optical tool monitoring system integrated with CNC machining center [9]. Flood coolant was applied throughout all the tests.

### 7.3.2. Tool wear vs. surface integrity experiment

Detailed milling experimental design is shown in Table 7.2.

Table 7.2 End milling conditions.

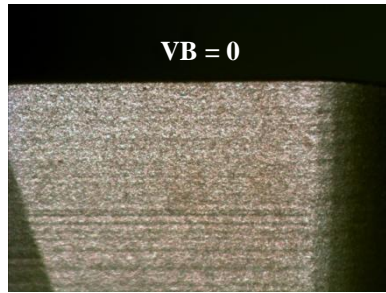
Sample #	VB (mm)	Cutting condition #	Cutting speed [m/min]	Feed per tooth [mm/tooth]	Radial DOC [mm]
1	0	1	40	0.15	0.5
2	0.1				
3	0.2				
4	0	2	60	0.15	0.5
5	0.1				
6	0.2				
7	0	3	80	0.15	0.5
8	0.1				
9	0.2				
10	0	4	60	0.1	0.5
11	0.1				
12	0.2				
13	0	5	60	0.2	0.5
14	0.1				
15	0.2				
16	0	6	60	0.15	0.3
17	0.1				
18	0.2				
19	0	7	60	0.15	0.4
20	0.1				
21	0.2				

Twenty one milling tests (7 different cutting conditions, with 3 levels of initial tool flank wear:  $VB = 0$ ,  $VB = 0.1$  mm, and  $VB = 0.2$  mm used for each cutting condition) were performed to study the effect of tool flank wear on surface roughness of machined samples at a variety of milling parameter combinations (Table 7.2). The axial depth of cut for each case was fixed as 0.5 mm.

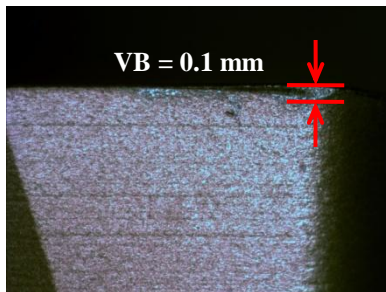
The dimension of the IN 718 samples was 25 mm × 21 mm × 13 mm. This relatively small area helped to reduce the progression of tool wear. Initial tool wears ( $VB = 0.1$  mm,  $VB = 0.2$  mm) were produced by machining on dummy samples before milling tests. Even though tool wear is developing all the time in machining, the cutting tool condition after each test was examined and wear variation could be neglected.

#### 7.4. Results and discussions

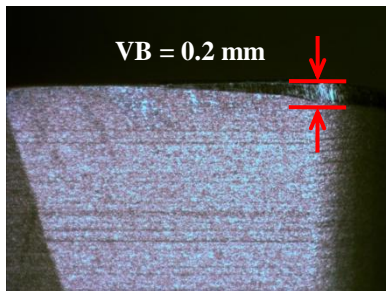
The representative optical images of cutting tools with the three different levels of flank wears used in the tool wear vs. surface integrity experiment are shown in Figure 7.1.



(1) Fresh tool (flank wear = 0)



(2) Tool with flank wear = 0.1 mm



(3) Tool with flank wear = 0.2 mm

Fig. 7.1 Flank wear of cutting tools.

#### 7.4.1. Characterization of surface roughness

Since surface roughness differs in the feed and step-over directions in end milling process [10], roughness in both directions for all the milled samples was measured by Sloan Dektak II profiler (stylus radius: 12.5  $\mu\text{m}$ ). Surface roughness data along feed direction and step-over direction for all the milled surfaces was shown in Figure 7.2.

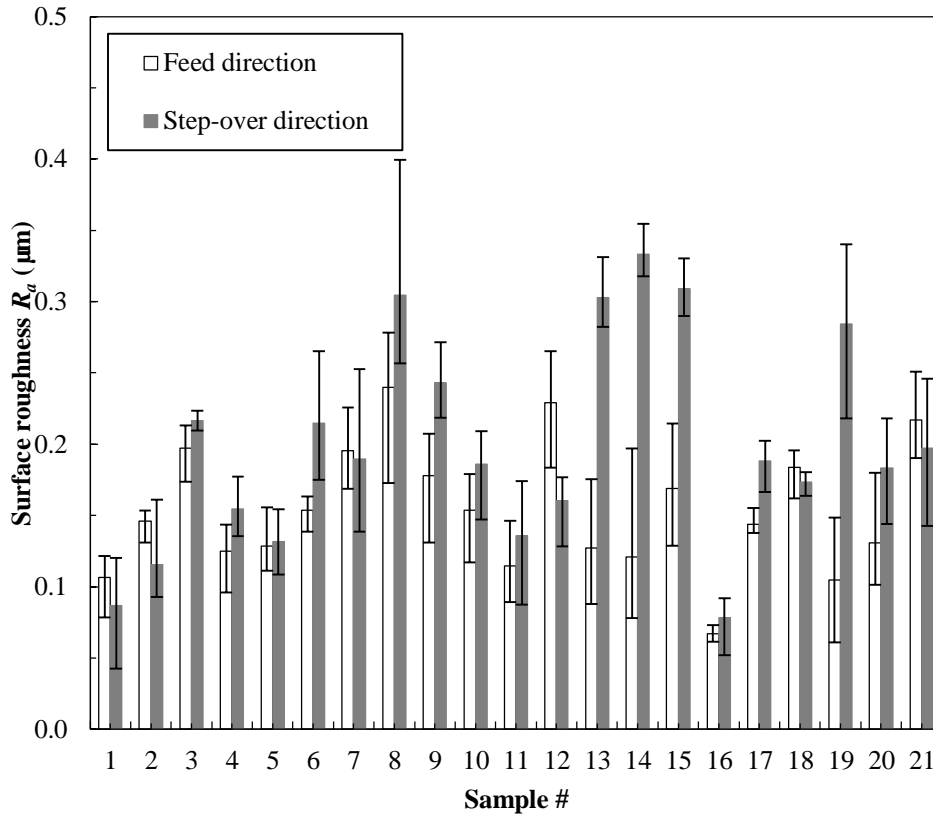


Fig. 7.2 Roughness ( $R_a$ ) in feed and step-over directions.

In order to get statistically reasonable surface roughness results, three measurements along each direction were made and measuring locations were different when tracing the machined surfaces. Figure 7.2 shows that 18 of all the 21 milled surfaces had much higher roughness  $R_a$  along step-over direction than along feed direction under the milling conditions listed in Table 7.2. Also, only 3 of all the 21 milled samples had an average surface roughness value of  $0.3 \mu\text{m} < R_a < 0.4 \mu\text{m}$  and the others were between  $0.1 \mu\text{m}$  and  $0.3 \mu\text{m}$ .

To investigate the effect of feed per tooth on surface roughness at different levels of tool flank wear, 9 of the 21 cases were extracted from surface roughness results, see Figure 7.3 (color

bars:  $R_a$  in step-over direction; white bars:  $R_a$  in feed direction). The highest feed per tooth:  $f_z = 0.20$  mm/tooth generated much higher roughness in step-over direction compared to lower feed per tooth at all tool wear levels. While, the use of intermediate, not the smallest, feed per tooth:  $f_z = 0.15$  mm/tooth gave the lowest roughness in step-over direction at all the cases.

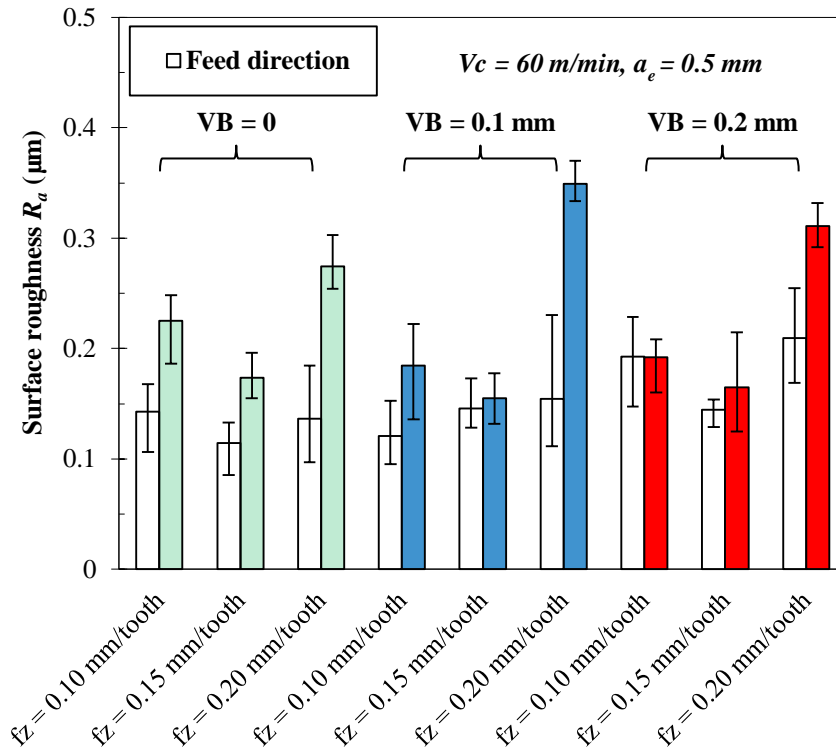


Fig. 7.3 Effect of feed on surface roughness at different tool wear levels.

Similarly, the cutting speed effect on surface roughness at different tool wear levels can also be analyzed by extracting the cases associated with different cutting speeds, see Figure 7.4. For  $VB = 0$  and  $VB = 0.1$  mm, surface roughness along step-over direction increased with increased cutting speed, while  $R_a$  is almost stable ( $\approx 0.20 - 0.25 \mu\text{m}$ ) at  $V_c = 80$  m/min under the three different tool flank wears. In feed direction, the increased tool flank wear produced rougher surfaces at each cutting speed level.

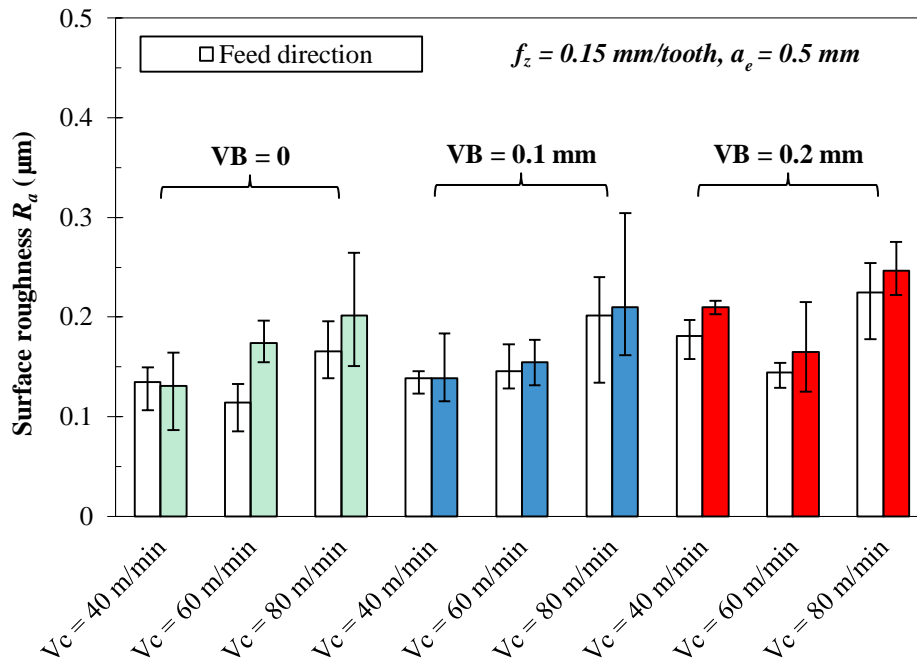


Fig. 7.4 Effect of cutting speed on surface roughness at different tool wear levels.

#### 7.4.2. Predictive model of surface roughness

Milled surface roughness is closely related to process parameters including cutting speed  $V_c$ , feed per tooth  $f_z$ , radial depth of cut  $a_e$ , and tool flank wear VB. In order for manufacturers to maximize their gains and minimize tooling cost in production, accurate predictive models for surface roughness incorporating the four process parameters need to be constructed. Comprehensive study on surface roughness in machining was performed by several investigators [11-14]. Classical empirical models of surface roughness for turning have been proposed by Taraman et al. [15] and Hasegawa et al. [16]. While, tool wear effect was not included in those models. A modeling of surface roughness and tool flank wear in turning of tool steel was developed by Özel et al. [17]. Prediction models for surface roughness in milling including

process parameters, especially tool wear, are necessary to be built up based on experimental results.

A basic theoretical model for surface roughness is given in Equation (7.1):

$$R_a = \frac{f^2}{32r_e} \quad (7.1)$$

Where  $f$  is feed rate and  $r_e$  is the tool nose radius. While, it does not take into account any geometry change of the cutting tool due to cutting forces and tool wear. Also, the effect of other process parameters was not incorporated in the model.

Another popular model was later proposed for surface roughness prediction in hard turning:

$$R_a = k_0 V^{k_1} f^{k_2} d^{k_3} r_e^{k_4} \quad (7.2)$$

Where  $V$  is cutting speed,  $f$  is feed,  $d$  is depth of cut, and  $r_e$  is the tool nose radius.  $k_0$ ,  $k_1$ ,  $k_2$ ,  $k_3$  and  $k_4$  are constants to be determined. Equation (7.2) combines both process parameters and tool geometry parameter. However, it may not work well in machining difficult-to-cut alloys since it lacks tool wear related parameter and tool wear is a common issue in these scenarios [18].

In this study, the relationship between surface roughness and the process parameters are represented by the following equation:

$$R_{a/avg} = c_0 V_c^{c_1} f_z^{c_2} a_e^{c_3} c_4^{VB} \quad (7.3)$$

-  $R_{a/avg}$ : average surface roughness ( $\mu\text{m}$ )

$$= (R_{a/feed} + R_{a/step-over})/2$$

-  $V_c$ : cutting speed (m/min)

-  $f_z$ : feed per tooth (mm/tooth)

- $a_e$ : radial depth of cut (mm)
- VB: initial tool flank wear (mm)
- $c_0, c_1, c_2, c_3$  and  $c_4$  are constants to be determined

Equation (7.3) can be expressed as:

$$\ln(R_{a/avg}) = \ln c_0 + c_1 \bullet \ln V_c + c_2 \bullet \ln f_z + c_3 \bullet \ln a_e + (\ln c_4) \bullet VB \quad (7.4)$$

Based on the characterized surface roughness results, 21 groups of data incorporating the effect of process parameters:  $V_c, f_z, a_e$ , and VB are imported to Minitab as data input. A multiple linear regression analysis was carried out by Minitab to model the relationship between the process parameters and the average surface roughness.

The detailed data input for regression analysis of all the process parameters and the average surface roughness can be seen in Table 7.3.

Table 7.3 Experimental matrix in end milling of IN 718.

Case #	$V_c$ [m/min]	$f_z$ [mm/tooth]	$a_e$ [mm]	$VB$ [mm]	$R_{a/avg}$ [ $\mu$ m]
1	40	0.15	0.5	0	0.1330
2	40	0.15	0.5	0.1	0.1384
3	40	0.15	0.5	0.2	0.1955
4	60	0.15	0.5	0	0.1441
5	60	0.15	0.5	0.1	0.1502
6	60	0.15	0.5	0.2	0.1545
7	80	0.15	0.5	0	0.1836
8	80	0.15	0.5	0.1	0.2054
9	80	0.15	0.5	0.2	0.2358
10	60	0.1	0.5	0	0.1838
11	60	0.1	0.5	0.1	0.1526
12	60	0.1	0.5	0.2	0.1926
13	60	0.2	0.5	0	0.2054
14	60	0.2	0.5	0.1	0.2516
15	60	0.2	0.5	0.2	0.2601
16	60	0.15	0.3	0	0.0884
17	60	0.15	0.3	0.1	0.1533
18	60	0.15	0.3	0.2	0.1773
19	60	0.15	0.4	0	0.2495
20	60	0.15	0.4	0.1	0.1646
21	60	0.15	0.4	0.2	0.2175

The regression analysis shows the equation as:

$$\ln(R_{a/avg}) = -2.535 + 0.4530 \cdot \ln V_c + 0.3907 \cdot \ln f_z + 0.5067 \cdot \ln a_e + 1.1047 \cdot VB \quad (7.5)$$

A detailed regression analysis table was generated by Minitab which can be seen in Table

7.4.

Table 7.4 Regression analysis from original data input.

Predictor	Coef.	SE Coef.	T	P
Constant	-2.535	1.156	-2.19	0.043
$\ln V_c$	0.4530	0.2541	1.78	0.094
$\ln f_z$	0.3907	0.2541	1.54	0.144
$\ln a_e$	0.5067	0.2606	1.94	0.070
VB	1.1047	0.5816	1.90	0.076

*Coef.*: the estimated coefficient of corresponding predictor

*SE Coef.*: the estimated standard deviation of the coefficient

*T*: equal to *Coef.* divided by *SE Coef.*

*P*: *p*-value, directly related to *T* ( $p < 0.05$  generally indicates significance of the predictor)

The result from Table 7.4 shows that only the *Constant* has a *p*-value less than 0.05 which means that other predictors are not significant. It helps to draw the conclusion that the current regression analysis cannot be accepted. The Minitab result also noted that cases 16 and 19 are unusual observations for the regression analysis. To optimize the prediction model, cases 16 and 19 were deleted from the data input and regression analysis was performed again with only 19 cases from Table 7.3.

The regression analysis table generated from the reduced data input showed that  $f_z$  (feed per tooth) and  $a_e$  (radial depth of cut) are still insignificant in the model. Case 6 and 10 were marked as unusual observations and were removed from data input before another regression analysis was performed. The reduced data set with 17 cases (see Table 7.5) produced the regression analysis table in Table 7.6:

Table 7.5 Reduced experimental matrix in milling of IN 718.

Case #	$V_c$ [m/min]	$f_z$ [mm/tooth]	$a_e$ [mm]	$VB$ [mm]	$R_{a/avg}$ [ $\mu$ m]
1	40	0.15	0.5	0	0.1330
2	40	0.15	0.5	0.1	0.1384
3	40	0.15	0.5	0.2	0.1955
4	60	0.15	0.5	0	0.1441
5	60	0.15	0.5	0.1	0.1502
6	60	0.15	0.5	0.2	0.1545
7	80	0.15	0.5	0	0.1836
8	80	0.15	0.5	0.1	0.2054
9	80	0.15	0.5	0.2	0.2358
10	60	0.1	0.5	0	0.1838
11	60	0.1	0.5	0.1	0.1526
12	60	0.1	0.5	0.2	0.1926
13	60	0.2	0.5	0	0.2054
14	60	0.2	0.5	0.1	0.2516
15	60	0.2	0.5	0.2	0.2601
16	60	0.15	0.3	0	0.0884
17	60	0.15	0.3	0.1	0.1533
18	60	0.15	0.3	0.2	0.1773
19	60	0.15	0.4	0	0.2495
20	60	0.15	0.4	0.1	0.1646
21	60	0.15	0.4	0.2	0.2175

Table 7.6 Regression analysis from the reduced data input.

Predictor	Coef.	SE Coef.	T	P
Constant	-2.2478	0.5486	-4.10	0.001
$\ln V_c$	0.4434	0.1175	3.77	0.003
$\ln V_c$	0.6093	0.1345	4.53	0.001
$\ln a_e$	0.3979	0.1481	2.69	0.020
$VB$	1.8112	0.3381	5.36	0.000

All the  $p$ -values in Table 7.6 are smaller than 0.05 which verified the significance of all the coefficients. Also, ANOVA (analysis of variance) was also carried out to investigate the influence of all the factors on the average roughness  $R_a$ . Table 7.7 represents the ANOVA

analysis at a significance level of  $\alpha = 0.05$ , i.e. for a confidence level of 95%. It may be observed that  $f_z$  (feed per tooth),  $VB$  (tool wear), and  $V_c$  (cutting speed) presented significant influences on surface roughness ( $p < 0.05$ ). However, the effect of  $a_e$  (radial depth of cut) on  $R_a$  would be ignored ( $p > 0.05$ ).

Table 7.7 Analysis of variance.

Source	DF	Seq SS	Adj SS	Adj MS	F	P
$\ln V_c$	2	0.0043	0.0047	0.0023	17.92	0.001
$\ln f_z$	2	0.0107	0.0102	0.0051	39.02	0.000
$\ln a_e$	2	0.0019	0.0007	0.0003	2.58	0.137
$VB$	2	0.0070	0.0070	0.0035	26.58	0.000
Error	8	0.0010	0.0010	0.0001		
Total	18	0.0250				

The regression analysis result from Table 7.6 shows the equation as:

$$\ln(R_{a/avg}) = -2.2478 + 0.4434 \cdot \ln V_c + 0.6093 \cdot \ln f_z + 0.3979 \cdot \ln a_e + 1.8112 \cdot VB \quad (7.6)$$

Thus the five constants  $c_0$ ,  $c_1$ ,  $c_2$ ,  $c_3$ , and  $c_4$  in Equation (7.3) can be calculated by comparing Equation (7.4) and Equation (7.6):

$$\left\{ \begin{array}{l} \ln c_0 = -2.2478 \\ c_1 = 0.4434 \\ c_2 = 0.6093 \\ c_3 = 0.3979 \\ \ln c_4 = 1.8112 \end{array} \right. \quad (7.7)$$

The constants are:

$$\left\{ \begin{array}{l} c_0 = 0.1056 \\ c_1 = 0.4434 \\ c_2 = 0.6093 \\ c_3 = 0.3979 \\ c_4 = 6.1178 \end{array} \right. \quad (7.8)$$

which makes Equation (7.3) can be represented as follows:

$$R_{a/avg} = 0.1056 V_c^{0.4434} f_z^{0.6093} a_e^{0.3979} 6.1178^{VB} \quad (7.9)$$

Based on the predictive model (Equation (7.9)) constructed by regression analysis in Minitab, surface roughness measured by surface profiler and predicted can be compared, see Figure 7.5. The outliers (case # 6, 10, 16, and 19) of the model were marked with dotted ellipses.

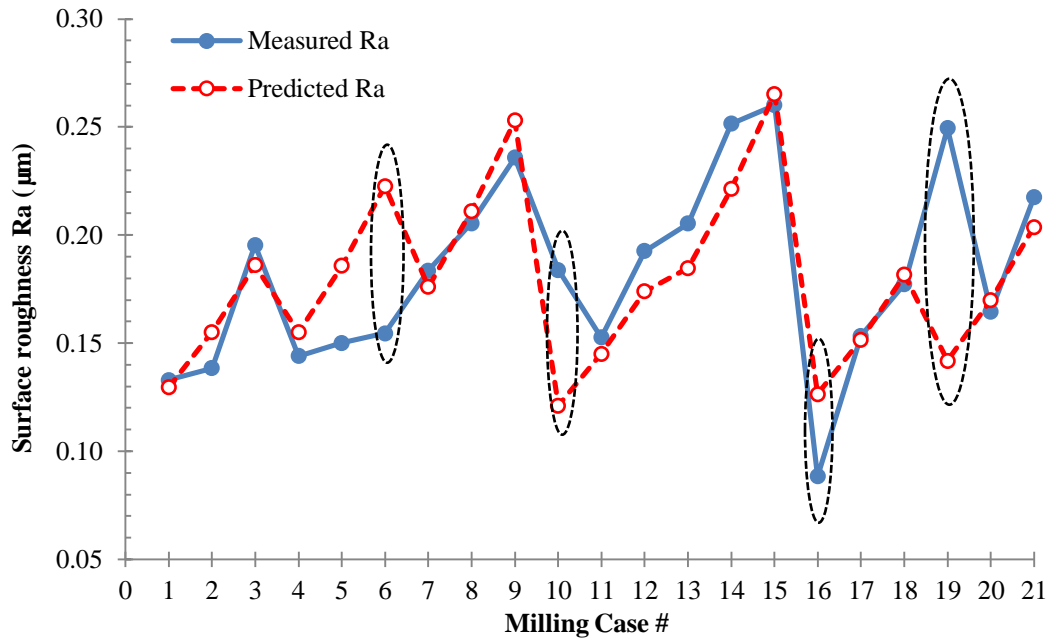


Fig. 7.5 Comparison between the measured and predicted surface roughness.

By incorporating the main process parameters to this model, including tool wear, it makes the predicting of milled surface roughness possible even for milling of difficult-to-cut alloys where rapid tool wear happens. In addition, if tool wear is not considered significant in the process, the tool wear effect on surface roughness can be ignored by making  $VB = 0$ . Axial depth of cut and tool nose radius are not included in this prediction model since they are not variables in the experimental design. But they could be introduced into the model when experimental plan defines these two parameters as variables.

## 7.5. Conclusions

End milling of superalloy IN 718 has been conducted to investigate the effects of tool flank wear and process parameters on surface roughness. The key findings of this research can be summarized as follows:

- Surface roughness in step-over direction is much higher than in feed direction under most of the milling conditions. The increased tool flank wear does not necessarily produce a rougher surface in both directions. The highest feed per tooth generates much higher roughness in step-over direction compared to lower feed per tooth at all tool wear levels. In feed direction, the increased tool flank wear produces rougher surfaces at each cutting speed.
- A predictive model of surface roughness by incorporating tool wear and process parameters (cutting speed, feed per tooth, radial depth of cut) has been constructed to determine the cause-effect relationship.
- A significance analysis by ANOVA shows that feed per tooth, tool wear, and cutting speed presented significant influences on surface roughness. However, the effect of radial depth of cut would be negligible.

## 7.6. References

- [1] Li W, Guo YB, Barkey ME, Guo C, Liu ZQ. Surface integrity and fatigue strength of hard milled surfaces. Proceedings of the ASME 2011 International Manufacturing Science and Engineering Conference, Corvallis, OR 2011. p. 199-206.
- [2] Li W, Guo YB. Residual stress and fatigue properties of AISI H13 steel by sustainable dry milling. Proceedings of the ASME 2012 International Manufacturing Science and Engineering Conference, Notre Dame, IN 2012.

- [3] Sharman A, Dewes RC, Aspinwall DK. Tool life when high speed ball nose end milling Inconel 718. *Journal of Materials Processing Technology* 2001; 118: 29–35.
- [4] Guo YB, Li W, Jawahir IS. Surface integrity characterization and prediction in machining of hardened and difficult-to-machine alloys: a state-of-art research review and analysis. *Machining Science and Technology* 2009; 13(4): 437-470.
- [5] Aspinwall DK, Dewes RC, Ng EG, Sage C, Soo SL. The influence of cutter orientation and workpiece angle on machinability when high-speed milling Inconel 718 under finishing conditions. *International Journal of Machine Tools & Manufacture* 2007; 47: 1839-1846.
- [6] Kim SW, Lee DW, Kang MC, Kim JS. Evaluation of machinability by cutting environments in high-speed milling of difficult-to-cut materials. *Journal of Materials Processing Technology* 2001; 111: 256-260.
- [7] Jawaid A, Koksai S, Sharif S. Cutting performance and wear characteristics of PVD coated and uncoated carbide tools in face milling Inconel 718 aerospace alloy. *Journal of Materials Processing Technology* 2001; 116: 2-9.
- [8] Alauddin M, El Baradie MA, Hashmi MSJ. Tool-life testing in the end milling of Inconel 718. *Journal of Materials Processing Technology* 1995; 55: 321-330.
- [9] Li W, Singh HM, Salahshoor M, Guo YB. The development of a novel on-line optical inspection system for tool conditions in machining processes. *Proceedings of the ASME 2010 International Manufacturing Science and Engineering Conference, Erie, PA 2010.*
- [10] Zhang S, Li W, Guo YB. Process design space for optimal surface integrity in finish hard milling of tool steel. *Production Engineering* 2012; 6(4-5): 355-365.
- [11] Nakayama K, Shaw MC. Relationship between cutting tool, temperature, built-up-edge and surface finish. *Annals of the CIRP* 1966; 14: 211-223.
- [12] Sata T. Surface finish in metal cutting. *Annals of the CIRP* 1964; 12: 190-197.
- [13] Koenig W, Berktold A, Koch F. Turning versus grinding – a comparison of surface integrity aspects and attainable accuracies. *Annals of the CIRP* 1993; 42(1): 39-43.
- [14] Matsumoto Y, Hashimoto F, Lahoti G. Surface integrity generated by precision hard turning. *Annals of the CIRP* 1999; 48(1): 59-62.
- [15] Taraman K, Lambert B. A surface roughness model for a turning operation. *International Journal of Production Research* 1974; 12(6): 691-703.
- [16] Hasegawa M, Seireg A, Lindberg RA. Surface roughness model for turning. *Tribology International* 1976; 9(6): 285-289.

- [17] Özel T, Karpat Y, Figueira L, Davim JP. Modelling of surface finish and tool flank wear in turning of AISI D2 steel with ceramic wiper inserts. *Journal of Materials Processing Technology* 2007; 189: 192-198.
- [18] Li W, Singh HM, Guo YB. An online optical system for inspecting tool condition in milling of H13 tool steel and IN 718 alloy. *International Journal of Advanced Manufacturing Technology* 2012; DOI: 10.1007/s00170-012-4548-7.